Ultracold collisions for atom–diatom systems with a reaction barrier

Ionel Simbotin, Ph.D.

University of Connecticut, 2012

Theoretical results for ultracold atom-molecule collisions involving exoergic reactions are presented. Systems with a reaction barrier are considered; specifically, we report the results of extensive computations for D + H_2 and Cl + H_2. We analyzed the extreme situation of translationally cold collisions between an atom and an internally hot molecule; namely, for D + H_2 we explored the role played by the internal vibrational excitation of the diatomic target for initial states $H_2(v)$ with $v = 0, 1, 2, \ldots, 8$. The v-dependence of the zero-temperature limit of the reaction rate coefficient shows two distinct regimes: a barrier dominated regime for $v < 4$, and a barrierless regime for $v > 4$. Also, for highly excited initial states, the distribution over the final states of the products shows an approximate conservation of the internal vibrational energy. For Cl + H_2 we studied in detail the isotopic effect by varying continuously the mass of H, which allowed us to find resonance effects in the threshold behavior of cross sections. These resonances are caused by long-lived van der Waals complexes (Cl$\cdots H_2$) which have vanishingly small binding energy, or by virtual states of the Cl$\cdots H_2$ complex.

Ultracold collisions for atom–diatom systems with a reaction barrier

Ionel Simbotin

Diploma, University of Bucharest, Romania, 1991

A Dissertation

Submitted in Partial Fulfillment

of the Requirements for the Degree of

Doctor of Philosophy

at the

University of Connecticut

2012

UMI Number: 3510538

UMI

Dissertation Publishing

UMI 3510538

ProQuest®

APPROVAL PAGE

Doctor of Philosophy Dissertation

Ultracold collisions for atom–diatom systems with a reaction barrier
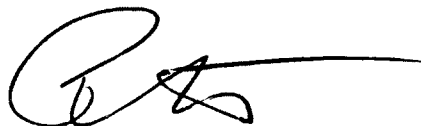
Presented by

Ionel Simbotin
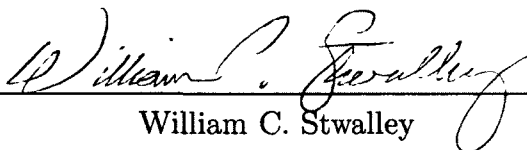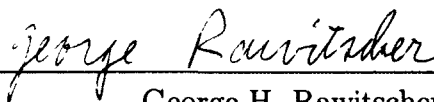
Major advisor _____

Robin Côté

Associate advisor _____

William C. Stwalley

Associate advisor _____

George H. Rawitscher

University of Connecticut

2012

for my wife Cristina

Acknowledgements

I would like to thank my major advisor, Prof. Robin Côté, and also Prof. Bill Stwalley and Prof. George Rawitscher, my associate advisors. I am greatly indebted to Robin, and to Bill and George for their support in general, and for many stimulating discussions we had.

I am also indebted to Prof. Alex Dalgarno and Prof. Mihai Gavrila for their support over the years.

I also give my warm thanks to Dr. Subhas Ghosal, my colleague and friend. Subhas and I shared an office for the last few years, and I enjoyed working together with him.

I give special thanks to Dr. Zoran Pavlović for his generosity. I am very lucky to have Zoran as a good friend.

I give my warmest thanks to my wife Cristina; her love and support and strength have kept me sane through the long years of graduate school.

Table of Contents

List of Tables

List of Figures

Chapter 1

Introduction

Collisions at the atomic scale are ubiquitous in nature—they are responsible for an entire host of processes: thermalization, chemical reactions, ionization, etc. These phenomena are characterized by physical quantities such as thermalization rates and reaction rates, which are expressed in terms of collision cross sections. Thus, the study of collisions is at the heart of understanding many complex phenomena. At a more fundamental level, collision experiments have been employed for the past century in our quest for learning the deepest secrets of the physical world, *e.g.*, in particle accelerators, where collisions at enormous energies are studied. More recently, during the last two or three decades, collisions at the opposite end of the energy scale are being explored in the areas of atomic, molecular and optical physics [6, 7].

The field of ultracold atomic physics has grown tremendously in the last two decades, and it is now overlapping with other areas of physics (e.g., condensed matter) and even other disciplines (chemistry, computer science). The early experiments dealt exclusively with dilute atomic gases, but soon the study of molecules at ultralow temperatures became inevitable. As in the case of atomic gases, reaching the regime of quantum degeneracy was initially the main goal, but now many other interesting processes involving cold molecules are being studied. One of the new areas of research is chemistry in the sub-Kelvin regime, as chemical reactions are inevitable in most experiments with cold molecules. For certain molecular species AB, the reaction channel $AB + AB \rightarrow A_2 + B_2$ can be open. Also, when cold molecules are produced

from cold atoms, *e.g.*, using photoassociation, then atom–molecule collisions can have reaction channels that are open, such as B + AB → A + B$_2$.

Given the success in the early work on alkali atomic gases, it is no surprise that these species (Li, Na, K, Rb, Cs) are also among the favorite ones in the experiments on cold molecules. Regarding the chemical reactions that can take place at very low temperatures, atom–diatom systems involving alkalies are highly reactive, because they are barrierless. Theoretically, this situation is advantageous, as it allows the use of comparatively simple models to estimate or parametrize the reaction rate coefficients in the ultracold regime [8, 9]. The opposite case of systems with a reaction barrier has received comparatively little attention, even though it has certain features that are very interesting. For example, when the scattering problem is highly elastic (*i.e.*, low reactivity due to the barrier, and also low inelasticity for the non-reactive channels) then it becomes possible for an s-wave resonance to be located near the threshold of the entrance channel, which will enhance strongly the reaction rate coefficient as $T \to 0$.

For this dissertation we have studied two examples of atom–diatom systems with high reaction barriers. Apart from the problem of near threshold resonances mentioned above, we also analyzed the role played by the initial vibrational excitation of the diatomic target in the ultracold collision. Although this situation (*i.e.*, internally hot molecules that are translationally cold) seems unusually extreme, it is quite common in laboratory experiments. In most of these experiments the goal is to obtain molecules that are both translationally and internally cold, *i.e.*, in the lowest rovibrational level, and it takes a great deal of effort and ingenuity to achieve this. Typically, in photoassociation experiments, translationally cold molecules are obtained in the ground electronic state, but in highly excited rovibrational levels. Thus, one needs detailed knowledge of ultracold collisions involving vibrationally excited molecules,

as they will inevitably take place. Although such collisions are detrimental from the point of view of obtaining a good sample of molecules that are internally (as well as translationally) cold, these collisions—either reactive or inelastic—can be quite interesting on their own. Indeed, a new area of chemical physics research—sub-Kelvin chemistry in the gas phase—is now a significant part of the broad field of cold molecules.

Collision problems involving molecules in highly excited internal states are generally demanding computationally, even when the scattering is non-reactive, simply because of the large number of coupled channels (both open and closed) that need to be included. For scattering with rearrangement, *i.e.*, a reaction, additional obstacles appear; indeed, the very choice of suitable coordinates becomes difficult. Asymptotically, each arrangement is most conveniently described in terms of Jacobi coordinates; however, different sets of Jacobi coordinates are suitable for different arrangements, and it is not at all straightforward how to combine them. To overcome this difficulty, and also to treat all atoms on an equal footing at short range, hyperspherical coordinates are usually employed in a coupled channel approach. In general, for a collision between an atom A and a diatomic molecule BC, one can have three possible arrangements: A–BC, B–AC, and C–AB. Note that, if a diatomic combination (*e.g.*, AB) does not have any vibrational bound states, then the corresponding arrangement (C–AB) cannot carry any probability flux asymptotically. Also note that the A–B–C arrangement (with all three atoms separated) will not be included, as we will only consider collisions well below the threshold for three body break-up.

Although a different set of Delves hyperspherical coordinates is defined for each arrangement, they all share the same hyperradius ρ (which stems from the properties of the mass scaling of the Jacobi coordinates). This makes it possible to use all three sets together; namely, one employs a simultaneous expansion of the full wavefunction

3

in an extended eigenbasis which contains the eigenbases for all arrangements. For each arrangement, the corresponding eigenbasis spans the part of the Hilbert space which depends on five angle coordinates. The extended eigenbasis is then orthogonalized, and the full wavefunction is expanded in this basis at each ρ. Thus, the original Schrödinger equation is transformed into a coupled system of ordinary differential equations along the hyperradius ρ. The set of coupled differential equations will be solved numerically, using a modified version of the ABC computer code developed by Manolopoulos and coworkers [10]. We have already adapted this computer program for the specific situation of ultracold collisions. The S-matrix is extracted by imposing scattering-type boundary conditions in the asymptotic region, after the wavefunction has been transformed back to Jacobi coordinates. The cross sections for individual state-to-state transitions are then evaluated in terms of the matrix elements of S.

Scattering problems at ultralow energy pose difficulties having to do with increased sensitivity to the details of the potential energy surface, especially at long range. It is well known from atom–atom collisions that the long-range tail of the interaction potential plays a very important role in the ultracold regime. This is also the case for atom–molecule collisions, where one encounters the surprising fact that the outcome of a chemical reaction depends greatly on the interaction at large separations, which is much more feeble than at short range (where the reaction takes place). We expect that this effect will be extremely important when a van der Waals complex (A$\cdots$BC) with vanishingly small binding energy is present in the entrance channel. Indeed, this should give a resonance enhancement for all the components (elastic, inelastic, reactive) of the scattering problem at ultralow energy.

4

1.1 D–H$_2$ collisions

In physical chemistry, H$_3$ is one the most studied systems; hence, a very accurate potential energy surface (PES) was computed [11] for it. From a practical standpoint, the availability of an accurate PES gives us a good reason to study the collision problem for this benchmark system at ultralow energy. In laboratory experiments it is only recently that cold molecular hydrogen was successfully trapped, albeit in high Rydberg states [12]. However, given the important role of hydrogen chemistry in the Universe in general [13], and especially in cold interstellar clouds, it is likely that cold molecular hydrogen will receive increased attention from the cold molecule community.

We studied the D + H$_2$(v, $j = 0$) $\rightarrow$ H + DH reaction for a wide range of initial vibrational states $v = 0, 1, 2, 3, 4, \ldots, 8$. Note that this reaction is exoergic at vanishing initial kinetic energy, even for the lowest initial state H$_2$($v = 0$, $j = 0$). For this system, experimental data for the reaction rate coefficient only exist for $T >$ 167 K, far above the sub-Kelvin regime; also, accurate theoretical results do not exist for $T \lesssim 100$ K, where the simple Arrhenius behavior will break down. Although we focus on the ultracold regime, we emphasize that for systems (like this one) with a reaction barrier, the intermediate (sub-thermal) regime between $T \approx 1$ K and (roughly) room temperature is also very interesting. Indeed, at high temperature, the reaction rate coefficient follows a simple Arrhenius type dependence; namely, $\mathcal{K}_{\text{Arrh}} = A \exp(-B/T)$, with A and B positive constants. However, this vanishes (very abruptly) when $T \rightarrow 0$, in contradiction with Wigner's threshold law [14], which says that $\mathcal{K}(T)$ should reach a constant (non-zero) value when $T = 0$. Surprisingly, we found that a deviation from the Arrhenius behavior appears at temperatures very high above the ultracold regime. In order to shed light on this question, we performed full computations for a very wide range of energies, from $T = 0$ to $T \approx 2000$ K (*i.e.*,

up to energies that are comparable to the height of the reaction barrier, which is roughly 5000 K for this system).

1.2 Cl–H$_2$ collisions

H$_2$Cl is another benchmark system in chemistry, and it also has a reaction barrier, albeit not as high as that of H$_2$D. Given the similarities of these two systems, we studied both of them in order to confirm the generality of some findings that emerged from our results. Note that for lowest rovibrational state ($v = 0, j = 0$) of H$_2$, the Cl + H$_2$ → HCl + H reaction is endoergic; thus, all reaction channels will be closed at low kinetic energy. Consequently, we will use as initial state H$_2$($v = 1, j = 0$), in which case there are plenty of open channels in the product (HCl) arrangement, even at vanishing kinetic energy.

Compared to D–H$_2$, Cl–H$_2$ is a more reactive system; also, it has rovibrational adiabats that are deeper, and can support more than one quasibound van der Waals complex. Thus, there is an increased likelihood of finding resonance effects in ultracold collisions. This will be the case if the Cl· · ·H$_2$ complex has a long lifetime against predissociation (*i.e.*, it has a very narrow width), and if its binding energy is vanishingly small. We investigated this systematically, by "tuning" the binding energy of the least bound van der Waals complex in the entrance channel. Practically, it was very convenient to explore this by changing the mass of the H atoms continuously, in order to carefully monitor how the collision is affected by binding energy of the complex (when it is shifted very close to the threshold). Although this seems rather artificial, it turned out to be a very instructive exercise. Also, note that this can simply be regarded as a very detailed study of isotopic effects. For example, comparing and understanding the differences between the results for different isotopologues (*e.g.*, Cl + H$_2$ and Cl + D$_2$) may require precisely this type of careful analysis. Moreover,

6

varying the mass is somewhat equivalent to modifying the PES itself, which often needs to be adjusted when comparing experiment with theory.

Chapter 2
An overview of scattering theory

The theoretical basis of our work is the formalism of scattering theory, which is a well established part of physics, and we shall only recapitulate certain parts of it here. The main purpose of this chapter is to translate the formal content of scattering theory into a practical framework that is suitable for numerical solutions. We shall try to give a clear overview of the physical and mathematical content of scattering theory, and we will adopt concrete representations (e.g., position, angular momentum) that fully reveal the details of the quantities entering our equations; if Dirac's bra-ket notation were to be used heavily, the presentation would be too obscure. Thus, we will mostly avoid the shorthand of abstract formalism, despite its virtues.

We begin this chapter with a discussion of the simplifying assumptions that are usually employed in scattering problems. After this general introduction, we will delve into the scattering theory proper; first, we will give a short account of the time-dependent formalism, where we will mostly discuss its physical (rather than mathematical) content. Then, we will move on to the time-independent approach, which we will present in greater detail, as it is much more suitable for computational work. Also, we will discuss briefly the connection between the two approaches.

2.1 Assumptions for the binary collision problem

The generic situation of a scattering experiment is that of a collimated beam of particles impinging on a target,[1] and we would like to find out under what conditions will a scattering experiment be accurately described by the scattering theory of binary collisions alone. We will see that one needs a series of simplifying assumptions, and we consider it instructive to review them.

2.1.1 Dilute conditions

We begin our discussion with the requirement that the number density of the beam particles is low enough such that their mutual interaction is vanishingly small. For clarity, we can envisage the projectiles being sent one at a time; in this idealized situation it is clear that the accumulated signal in a scattering experiment will be directly proportional with the total number of beam particles (more specifically, the number of projectiles that fall on the target).[2]

In cross beam experiments, the target is itself a beam of particles, just like the projectile beam, and one could arrange that both beams are very dilute. Thus, we are sketching here a thought experiment which consists of a long sequence of truly individual binary collisions. But even under such idealized conditions, we still need to consider how these beams were collimated, i.e., whether the wavepackets come in a certain distribution, etc. In other words, all the relevant details of the experimental apparatus need to be taken into account, as the results for the cross section may actually depend on the particular shape of the wavepackets; indeed, the expression

---

[1]The terminology is not quite appropriate, as the target is not necessarily fixed; in many experiments, both the target and projectile particles are moving (e.g., two crossing beams).

[2]It is possible that the extent of the target in the plane transverse to the beam direction is smaller than the beam waist; in such a case, we should ignore the beam particles falling outside the target area. Conversely, for a large target, only those scatterers within the part of the target that is "illuminated" by the beam will contribute.

9

of the cross section does not simply contain the product of the two fluxes of the projectile and target beams, but also an overlap integral of the wavepackets.[3] This unwanted complication will only go away if we use additional simplifying assumptions regarding the transverse distributions of the wavepackets in the beams, see Sec. (4.1). However, this detailed analysis is not always necessary; e.g., the flux factor may not need to be known if one is not interested in the absolute values of the cross section. Often, the interesting parts are the various features in the energy dependence or the angular dependence of the cross section. Some of the intrinsic characteristics of these features (positions, widths, shape, etc) do not require precise calibration of the absolute value of the scattering signal. Also, the branching ratios of cross sections for different processes (elastic, inelastic, etc.) are independent of the overall flux factor (which simply cancels out).

When both the beam and the target are dilute, it is also justified to neglect collisions in which more than two particles participate (e.g., three body recombination). For collisions in the gas phase, it is always possible to satisfy the diluteness assumption by lowering the density (pressure) accordingly, unless, of course, high density is needed in the first place for achieving the main results of the experiment (e.g., reaching quantum degeneracy in ultracold gases). In general, at high densities, many-body processes may become important, and they need to be taken into account, along with the binary collisions.

2.1.2 Low opacity. No multiple scattering.

Assuming the projectile beam consists of one-at-a-time particle shots, we now focus our attention on the target. In order to have a very clean scattering experiment, each projectile passing through the target must have suffered a single collision, or none

---

[3]See Goldberger and Watson, page 89.

at all. This additional simplification can be achieved by requiring that the target be highly transparent to the projectile particles; in other words, we assume the mean free path of the projectiles in the target medium to be much longer than the macroscopic spatial extent of the target (its thickness). If the target is gaseous, one can meet this assumption by simply reducing the pressure (low number density). For solid targets, one can use a thin foil or a small crystal as a target. The probability for multiple collisions in sequence will thus be kept vanishingly small.

The first two assumptions that we discussed so far (dilute conditions, and thin target) ensure that complicated processes (multiple scattering, three body recombination, etc.) are very unlikely; therefore, it is safe to neglect them entirely. However, there may be other complications; for instance, we still need to find out if the scattering signal is directly proportional to the number of scatterers (target constituent particles).

2.1.3 Incoherent scattering. The assumption of independent scatterers.

In the general area of atomic collisions, it is usually assumed that the scattering centers inside the target contribute independently, i.e., the scattering signal is an incoherent sum over the scatterers. But, for elastic scattering, the contributions from individual scatterers will add up coherently if the scatterers are within the spatial extent of the projectile wavepacket. These coherent contributions may generate interference effects; thus, the independent scatterer assumption is equivalent to saying that the conditions are such that the interference terms will cancel out almost entirely.

However, the interference effects do not simply vanish, but rather they are averaged out; this is what we expect if the de Broglie wavelength of the projectile is much shorter than the separation between the scattering centers inside the target. Indeed, the absence of the interference can be understood qualitatively by using the

11

analogy between the situation when we have just two scattering centers and the well known double slit experiment; in the latter, the interference fringes may become too narrow to be resolved by the detector (which has finite spatial resolution) when the separation between the slits is much larger than the de Broglie wavelength. Without being able to resolve the interference fringes, the double slit setup will give a signal that is simply twice the signal for a single slit. Effectively, the two slits will contribute incoherently, simply because coherence effects (interference fringes) cannot be resolved. One would thus only be able to resolve the (broader) angular dependence coming from single slit diffraction.

Returning now to atomic collisions, we can say that if the de Broglie wavelength is short enough, i.e, at high collision energies, the accumulated signal is simply proportional to the number of scatterers, and the only angular dependence that remains is due to single center scattering. Conversely, when the de Broglie wavelength becomes comparable to the distance between the scattering centers, we should remember that we are dealing with coherent scattering, and we need to approach the problem carefully. A good example is the so-called Bragg scattering; however, one should not think that coherent scattering only takes place in the case of a crystalline target.

2.2   Elements of time-dependent formalism

The mathematics of the quantum theory of scattering is very similar with that of the scattering of classical waves. At the same time, it has strong similarities with the classical theory of scattering for particles; indeed, both the classical and quantum mechanical descriptions rely on the assumption that, before the collision, the particles

propagate freely until the separation between them is small enough for the interaction to play its role; after the collision, the fragments again propagate freely.[4]

The physical picture associated with a scattering problem is that of a collimated beam of particles impinging on a (fixed) target, which suggests naturally that a time-dependent approach should be used. For clarity, we have in mind the simple case of potential scattering for a spinless particle of mass μ, with free and full Hamiltonians $H_0 = -\frac{\hbar^2}{2\mu}\nabla^2$ and $H = H_0 + V(\vec{r})$ respectively. We shall work with this simplest of examples in the first part of this chapter; then, after a brief review of the basic elements of scattering theory for this single channel problem, we will move on to the multichannel case. We denote by Φ the free states, which are solutions of the time-dependent Schrödinger equation for the free Hamiltonian:

$$i\hbar \frac{d\Phi(t)}{dt} = H_0 \Phi(t). \tag{2.1}$$

The scattering states, which we denote by Ψ, are solutions of the time-dependent Schrödinger equation for the *full* Hamiltonian, $H = H_0 + V$,

$$i\hbar \frac{d\Psi(t)}{dt} = (H_0 + V)\Psi(t), \tag{2.2}$$

and their definition will be spelled out in full below. Note that in this section, our generic notations Φ and Ψ stand for *proper*, i.e., normalizable[5] vectors in the abstract Hilbert space associated with the physical problem at hand; for concreteness, it is

---

[4]Peculiar situations may occur, e.g., for charged particles the long range nature of the Coulomb interaction poses certain difficulties. Also, if three or more particles emerge from the collision, two of them can remain near each other on their way out, and the interaction between them will not vanish. In our work, however, we will not consider these situations.

[5]The plane-wave-type solutions are not normalizable, except in the generalized sense; hence, they do not belong to the Hilbert space of square integrable functions. However, they are very useful in the time-independent formalism, as we will see in the next section.

helpful to have in mind the position or momentum representation, in which they can simply be viewed as normalizable wavepackets.

2.2.1 The wavepacket description of a scattering event

We begin by specifying the initial condition for Eq. (2.2) according to a typical scattering experiment; namely, at some initial time $t = t_1$ the wavefunction in the position representation is

$$\Psi(\vec{r}, t_1) = \phi(\vec{r}), \tag{2.3}$$

where $\phi(\vec{r})$ is a square integrable function (normalized to unity). Thus, the initial wavepacket is not a plane wave, i.e., it is not an eigenfunction of the momentum operator. However, its momentum is very well defined; in other words, its Fourier transform $\varphi(\vec{p})$ is sharply peaked around $\vec{p} \approx \vec{p}_1$; hence, $\phi(\vec{r})$ is very broadly spread in $\vec{r}$, and it occupies a volume that is much larger than the interaction region. Nevertheless, one assumes that the wavepacket is still well localized macroscopically in coordinate space; namely, the length and width of the wavepacket $\phi(\vec{r})$ are much smaller than the distance between its initial location (the collimation slit) and the scattering center.

As the wavepacket approaches the scattering center, it will be affected by the interaction potential, and a small fraction of the wavepacket will scatter in all directions. Finally, long after the collision, there will be a roughly spherical shell of probability propagating outwards toward the detectors. This outgoing wave has different amplitudes depending on the direction of propagation, which will determine the strength of the signal in the detectors surrounding the scattering center.

The mathematical machinery of formal scattering theory is quite formidable, and it can obscure a qualitative understanding of the physical aspects of the problem.

14

Here, we give a qualitative discussion of the subtleties involved in the formulation of a scattering problem. We first emphasize the key assumption: $V(\vec{r})$ vanishes fast enough when $r \to \infty$; also, V is assumed to be well behaved generally. More specifically, one restricts the class of potentials according to the mathematical niceties that are required (e.g., convergence of the Born series in a perturbative approach). Some of the mathematical demands carry a high price, as they are too restrictive with regard to the class of acceptable potentials. Thus, in order to relax the conditions imposed on $V(\vec{r})$, one can take a more pedestrian approach; indeed, working in coordinate representation, one can merely require that the scattering amplitude exists. The class of reasonable potentials can thus be enlarged to include even those with a Coulomb tail.

2.2.2 The scattering operator

We now begin to tackle the mathematical formalism, which will lead us to a formal definition of the cross section. The initial wavepacket in Eq. (2.3) will evolve according to the time-dependent Schrödinger equation with the full Hamiltonian $H = H_0 + V$. However, the potential V only plays a significant role in the immediate proximity of the scattering center $\vec{r} \approx \vec{r}_0 = 0$. Thus, except for a short duration (when the actual collision takes place) the wavepacket propagates almost freely (both before and after the collision). We are then tempted to push the initial time towards the remote past $(t_1 \to -\infty)$ and the final time towards the distant future $(t_2 \to \infty)$. While this mathematical maneuver is very familiar, a great deal of care is needed in taking these limits for a scattering problem.

Experimentally, one could practically approximate the conditions $t_1 \to -\infty$ and $t_2 \to \infty$ by pushing both the collimation slit and the detector farther and farther from the scattering center. Naively, one would expect the scattering experiment to give

15

results that are independent of the size of the apparatus; however, the wavepacket is spreading, even as it propagates freely before the collision. While this may seem a negligible effect, the free propagation spreading becomes important in the limit $t_1 \to -\infty$; indeed, the wavepacket will stretch and become indefinitely thin before it even reaches the target. Thus, in the limit $t_1 \to -\infty$, the incident flux at the target will diminish to zero.[6]

Mathematically, one can see the difficulty in our equations; indeed, writing the formal solution $\Psi(t)$ in terms of the evolution operator U,

$$\Psi(t_2) = U(t_2, t_1)\,\Psi(t_1),$$

one is tempted to take the limit

$$\lim_{\substack{t_2 \to +\infty \\ t_1 \to -\infty}} U(t_2, t_1) = (?)$$

However, this limit does not exist. As we discussed above, the evolution operator $U(\infty, -\infty)$ would take a given wavepacket and would stretch (spread) it infinitely thin. Although such a wavepacket will not vanish (its norm is actually conserved), its projection on any given wavepacket (any normalized vector in the Hilbert space) will vanish. In other words, the weak-limit of U is zero, and this approach leads nowhere; also, note that the strong-limit simply does not exist [15].

This mathematical obstacle is overcome by undoing the indefinite spreading caused by the full evolution operator by using a time reversed evolution governed by the free Hamiltonian. Such a combination of evolution operators does exist, and it allows us

---

[6]The same difficulty is encountered if we neglect the quantum mechanical spreading, and consider instead a slight beam divergence that is entirely classical (geometrical). In general, both classical and quantum divergence effects may be important.

to take the limit. Thus, rather than shifting the collimation slit to a different starting place (farther away), one pretends that the wavepacket is time evolved backwards with the free Hamiltonian to $t_1 \to -\infty$. Given a fixed instance of time $t = t_0$ we take a wavepacket Φ_0 that has very well defined momentum (and is also well localized macroscopically, say around $\vec{r} \approx \vec{r}_0 = 0$) and we free-evolve it back in time ($t < t_0$). In order to maintain consistency with the experimental situation, we choose Φ_0 such that there exists $t = t_1$ for which the freely evolved wavepacket

$$\Phi(t_1) = U_0(t_1, t_0)\, \Phi_0$$

is nearly identical with the wavepacket produced by the collimation slit in the actual experiment.[7] However, we no longer keep $t = t_1$ fixed, but we allow it to become very large and negative.

Next, we take $\Phi(t_1)$ and we use it as initial state for the full problem, i.e., we evolve it forward in time ($t > t_1$) according to the dynamics governed by the full Hamiltonian. For $t = t_2$ we have

$$\Psi(t_2) = U(t_2, t_1)\, \Phi(t_1),$$

which is the final state after the scattering took place. The momentum distribution $|\Psi(\vec{p}, t_2)|^2$ of the final state gives us precisely the detection probabilities in the directions $\hat{p}$. While this may seem the end of the story, we actually need one final step to complete our construction of the scattering operator. Namely, we use the final state

---

[7]Note that scattering problems are formulated in terms of free momentum states, which are also eigenstates of the free Hamiltonian; thus, the free evolution from t_0 to t_1 will not alter the momentum distribution $|\Phi(\vec{p}, t)|^2$. Consequently, $\Phi_0 = \Phi(t_0)$ can be regarded as our initial state, even though it is $\Phi_1 = \Phi(t_1)$ that is actually produced by the collimation slit.

$\Psi(t_2)$ as an initial condition for the free evolution operator, which will take it back in time again (for $t < t_2$). At $t = t_0$ we will have

$$\Phi_f(t_0) = U_0(t_0, t_2) \, \Psi(t_2).$$

This last step is completely artificial experimentally, but it does not affect the probability amplitudes for scattering, i.e., $\Psi(t_2)$ and $\Phi_f(t_0)$ give the same amplitudes when projected on momentum eigenstates (which are also eigenstates of the free Hamiltonian). Mathematically, it is necessary to undo the infinite spreading in the distant future (just as it was done for the remote past) in order to complete a meaningful definition of the scattering operator.

Combining all these steps, we have

$$\Phi_f(t_0) = U_0(t_0, t_2) \, U(t_2, t_1) \, U_0(t_1, t_0) \, \Phi_0$$

Now, one can safely take the limits $t_1 \to -\infty$ and $t_2 \to \infty$, to obtain the definition[8] of the scattering operator:

$$\mathbb{S} \equiv \lim_{\substack{t_2 \to +\infty \\ t_1 \to -\infty}} U_0(t_0, t_2) \, U(t_2, t_1) \, U_0(t_1, t_0). \tag{2.4}$$

---

[8]The scattering operator is sometimes written incorrectly as

$$\mathbb{S} = \lim_{\substack{t_2 \to +\infty \\ t_1 \to -\infty}} U(t_2, t_1).$$

As we already discussed, but this limit does not exist. Also adding to the confusion is the fact that in Eq. (2.4) we recognize the evolution operator in the interaction picture; indeed, $\mathbb{S}$ can be written as

$$\mathbb{S} = \lim_{\substack{t_2 \to +\infty \\ t_1 \to -\infty}} U_{\mathrm{int}}(t_2, t_1).$$

However, the Schrödinger picture is more amenable to a physical interpretation.

18

This limit exists, and it is independent of t_0. Choosing $t_0 = 0$ and writing the evolution operators explicitly in terms of the free and full Hamiltonians, the definition of $\mathbb{S}$ reads

$$\mathbb{S} = \lim_{\substack{t_2 \to +\infty \\ t_1 \to -\infty}} e^{it_2 H_0}\, e^{-i(t_2 - t_1)H}\, e^{-it_1 H_0},$$

with Φ_0 as our initial state, and Φ_f as the final state. The importance of the scattering operator $\mathbb{S}$ stems from the fact that it is precisely the operator which takes an initial state and gives us the final state of the full scattering problem:

$$\Phi_f = \mathbb{S}\,\Phi_0$$

2.2.3 Detection probabilities in a scattering experiment

We continue our discussion of a single scattering event, i.e., a single projectile described by a certain wavepacket $\Psi(t)$ evolving in time. Thus, we are first defining the scattering probability; later in this chapter, we will give the definition of the cross section, which involves an incident beam containing a large number of projectiles.

The probability for detecting the particle scattered in a certain direction is given by the final state wavepacket in the momentum representation. Namely, we integrate $|\Phi_f(\vec{p})|^2$ inside a narrow cone C:

$$\Delta(\text{prob}) = \int_C \mathrm{d}^3\vec{p}\,|\Phi_f(\vec{p})|^2 \approx \Delta\Omega_{\hat{p}} \int_0^\infty \mathrm{d}p\, p^2 |\Phi_f(\vec{p})|^2.$$

As we have shown in the previous section, the final state is given by the action of the scattering operator on the initial state: $\Phi_f = \mathbb{S}\,\Phi_0$. Its explicit form in the momentum representation,

$$\Phi_f(\vec{p}) = \langle \vec{p}\,|\,\Phi_f \rangle = \langle \vec{p}\,|\,\mathbb{S}\,|\Phi_0 \rangle = \int \mathrm{d}^3\vec{p}\,'\, \langle \vec{p}\,|\,\mathbb{S}\,|\vec{p}\,'\rangle\, \Phi_0(\vec{p}\,')$$

19

shows clearly that, for a given initial wavepacket, the scattering probability is determined by the matrix elements of $\mathbb{S}$ between free momentum eigenstates.

Other representations (e.g., angular momentum) are more useful for computational purposes, but the momentum representation has a certain advantage when it comes to the formal derivation of the cross section formula. This has to do with the simple fact that the initial wavepacket $\Phi_0(\vec{p})$ is very sharply peaked around the initial momentum $\vec{p} \approx \vec{p}_1$, which helps in dealing with the integrals above.

2.2.4 The S-matrix

It is now clear that solving a scattering problem amounts to finding the matrix elements of $\mathbb{S}$, and, because a scattering process represents a transition between free states, the obvious choice for a basis is an eigenbasis of the free Hamiltonian.

In order to define the S-matrix we first make the observation that the scattering operator commutes[9] with the free Hamiltonian. Consequently, in any given eigenbasis $\{\Phi_{E\alpha}\}$ of the free Hamiltonian,

$$H_0\Phi_{E\alpha} = E\Phi_{E\alpha}$$

the matrix elements of $\mathbb{S}$ contain an energy-conserving[10] delta function,

$$\langle\Phi_{E'\beta}|\,\mathbb{S}\,|\Phi_{E\alpha}\rangle = \delta(E' - E)\,S_{\beta\alpha}(E).$$

---

[9]Given the fact that $\mathbb{S}$ depends on the interaction potential V in a complicated way, it is quite remarkable that $[\mathbb{S}, H_0] = 0$. This is a direct consequence of the particular combination of free and full evolution operators that $\mathbb{S}$ contains, and the fact that $V(\vec{r})$ vanishes at large distances. The key factor is the vanishing role of the interaction both in the remote past and in the distant future.

[10]We already know that energy is conserved, simply because V (and hence H) does not depend on time. As we mentioned in the previous footnote, the commutation property $SH_0 = H_0S$ expresses much more than energy conservation.

Note that the matrix elements $S_{\beta\alpha}(E)$ are defined only after this delta function has been factored out. We thus have a matrix $S(E)$ for each positive energy $E > 0$, and all these matrices inherit their properties (e.g., unitarity) from the scattering operator itself.

The subscripts α and β are quantum numbers that account for the infinite degeneracy of the positive energy eigenvalues. They depend on the concrete representation that is chosen. For example, in the angular momentum representation, the free states are $\Phi_{E\ell m}$ and $S_{\beta\alpha}$ becomes $S_{\ell'm',\ell m}$.

2.2.5 The T-matrix

In the absence of the interaction ($H = H_0$) there is no scattering taking place, and we have $\mathbb{S} = \mathbb{I}$. This suggests that it would be convenient in general to subtract this non-scattering contribution from the S-matrix. We remark that the separation of the scattered contribution (given by $\mathbb{S} - \mathbb{I}$) and the unscattered one (given by the unity operator $\mathbb{I}$) is not an approximation.[11] Assuming an orthonormal eigenbasis $\{\Phi_{E\alpha}\}$ of the free Hamiltonian, we have for the scattered part

$$\langle \Phi_{E'\beta}|\, \mathbb{S} - \mathbb{I}\, |\Phi_{E\alpha}\rangle = \delta(E' - E)\left[S_{\beta\alpha}(E) - \delta_{\beta\alpha}\right]$$

which defines, up to a factor,[12] the T-matrix:

---

[11] The separation into scattered and unscattered parts is indeed exact, but it becomes inoperational near the forward direction, as discussed in Sec. (2.4.1). In the forward direction, the scattered wave will interfere with the unscattered wavepacket, and the distinction between them is lost.

[12] The $\frac{2\pi}{i}$ factor is introduced for convenience; namely, we want that the expression of the T-matrix in terms of the potential energy be free of such factors, i.e.,

$$T_{\beta\alpha}(E) = \langle \Phi_{E\beta}|\, V\, |\Psi_{E\alpha}^{(+)}\rangle.$$

The stationary scattering states $\Psi_{E\alpha}^{(+)}$ are eigenstates of the full Hamiltonian, and they will be discussed later.

21

$$\frac{2\pi}{i} T_{\beta\alpha}(E) \equiv S_{\beta\alpha}(E) - \delta_{\beta\alpha} \qquad (2.5)$$

It is important to notice that, due to the energy conserving[13] delta function, this equation only defines the matrix elements $T_{\beta\alpha}(E)$ separately for each energy E; indeed, Eq. (2.5) does not automatically define a $\mathbb{T}$ operator.

The T-matrix, which is the necessary ingredient for calculating the cross section, is computed either by solving an integral equation that the T-matrix itself satisfies, or it is found by solving the time-independent Schrödinger equation for the full Hamiltonian H. Appropriately chosen, the eigenfunctions of H are the so-called scattering states, which, through their asymptotic behavior, bear a direct relationship to the T-matrix. Indeed, as we shall see later in this chapter, the scattering amplitude (which is the T-matrix under a different name) is calculated by imposing appropriate boundary conditions for the scattering solutions.

2.2.6 From time-dependent to time-independent formalism

The derivation of the cross section formula—the central result of the scattering theory—relies on a series of assumptions, whose necessity and physical meaning are best understood within the time-dependent formalism, i.e., through the use of wavepackets. Such an approach is more laborious than the simplified description of the scattering process using stationary states, but it gives us the benefit of knowing the limitations of the validity of our results; should we have to deal with a situation when certain assumptions are not fulfilled, we will be better prepared to recognize it and address it.

---

[13]For this reason, $T_{\beta\alpha}(E)$ is called the on-shell T-matrix. Off-shell extensions can also be defined, either fully off-shell or half-off-shell, and they can be regarded as the matrix elements of a $\mathbb{T}$ operator, which is defined in terms of Green functions and the interaction V; see Refs. [15] and [16].

As we tried to convey in this chapter so far, the time-dependent formalism provides the correct approach to studying scattering processes; this is not just for reasons having to do with mathematical rigor—it is, in fact, the approach that is physically sound. However, a time-independent approach is also needed, if only for practical reasons; indeed, the T-matrix is usually found by solving the equations of the time-independent formalism.

The recipe for switching between the two formalisms reads as follows: time-dependent quantities are converted into their energy-domain counterparts. For example, propagators (evolution operators) are turned into Green functions $G(E)$, normalized wavepackets $\Psi(t)$ into stationary scattering states, etc., and an entire time-independent formalism is produced. This is achieved through Fourier transformations between the time and energy domains; for details, see Ref. [15].

2.3 Stationary scattering solutions

In the remainder of this chapter we give a short account of the elementary time-independent approach to scattering theory. We start with the simple case of potential scattering, but we consider an interaction energy $V(\vec{r})$ which does *not* have spherical symmetry; this will make this example more instructive, as the partial wave analysis for this single-channel problem will lead to a system of fully coupled radial equations. Compared to the much simpler case of a spherically symmetrical potential, for which there are only uncoupled equations, the general case will provide a more abrupt introduction to scattering theory, and it will better prepare us to tackle the complications of the three body problem.

In non-relativistic quantum mechanics, the Hamiltonian (in atomic units) for a spinless particle of mass μ under the influence of a potential energy $V(\vec{r})$ is $H = -\frac{1}{2\mu}\nabla^2 + V$, and the time-independent Schrödinger equation reads:

$$H \, \Psi_E(\vec{r}) = E \, \Psi_E(\vec{r}). \qquad (2.6)$$

For scattering problems, we are interested in the continuous part of the spectrum ($E \geq 0$). All positive energies are infinitely degenerate eigenvalues, and their corresponding eigenfunctions Ψ_E should carry additional labels for identification. We like to emphasize that, for scattering problems, these labels are quantum numbers associated with observables that commute with the *free* Hamiltonian; such observable (e.g., $\vec{P}$) do not necessarily commute with the full Hamiltonian H (this will become apparent when we discuss the asymptotic boundary conditions next[14]).

2.3.1 Asymptotic boundary conditions

The eigenfunction Ψ_E can be made unique by imposing specific boundary conditions in the asymptotic region. Indeed, assuming $V(r) \to 0$ when $r \to \infty$, any eigensolution Ψ_E of the full Hamiltonian can be written (at large r) as a linear combination of free-particle eigensolutions for the same eigenenergy E. Among the infinite number of choices, there is a particular one which is compatible with the physical picture of a scattering process; namely, we specify the asymptotic behavior of Ψ_E to be that of a plane wave of fixed momentum $\vec{p}$ superposed with an outgoing spherical wave:

$$\Psi_{\vec{p}}^{(+)}(\vec{r}) \overset{r \to \infty}{\sim} e^{i\vec{p}\cdot\vec{r}} + \frac{e^{ipr}}{r} f_{\vec{p}}(\hat{r}). \qquad (2.7)$$

---

[14] The connection between free particle states and scattering states can be made more explicit when the scattering problem is formulated in the language of Green's functions and the Lippmann–Schwinger equation.

This procedure makes the solution unique, and we use the notation $\Psi_{\vec{p}}^{(+)}$ to indicate this fact; the superscript $^{(+)}$ denotes the outgoing spherical wave.[15] The scattering amplitude $f(\hat{r})$, which is to be determined, gives the amplitude of the spherical wave for all possible directions $\hat{r}$; when squared, it gives the differential cross section $d\sigma/d\Omega = |f|^2$. We shall discuss this well known formula in the next section. The momentum $\vec{p}$ is only constrained by $E = \frac{p^2}{2\mu}$, and its direction $\hat{p} = \vec{p}/p$ accounts fully for the infinite degeneracy of the eigenenergy.

We like to mention that, while the asymptotic behavior for the scattering solution in Eq. (2.7) can simply be regarded as a good ansatz based on physical grounds, in a rigorous approach it is derived from the equations of time-dependent scattering theory; indeed, the time-dependent formalism leads to a time-independent approach framed in terms of Green functions and Lippmann–Schwinger equations for the scattering solutions. These are integral equations which have the asymptotic boundary conditions built into them. However, we follow a more pedestrian approach based directly on the time-independent Schrödinger equation.

2.4 Cross sections

2.4.1 Operational definition of the cross section as an effective scattering area

In a realistic experimental situation, a large number N_{inc} of particles are sent as a collimated beam towards the target. Assuming these projectiles are distributed uniformly in the plane perpendicular to the beam, the incident flux n_{inc} is defined as an area density,

---

[15]Our scattering amplitude in Eq. (2.7) should read $f^{(+)}$ but we drop the superscript for simplicity. Notice that a different solution denoted $\Psi_{\vec{p}}^{(-)}$ and a different scattering amplitude $f^{(-)}$ can be obtained if we specify an incoming spherical wave e^{-ipr}/r in place of the outgoing one in Eq. (2.7).

$$n_{\text{inc}} = \frac{N_{\text{inc}}}{A_{\text{beam}}},$$

where A_{beam} is the transverse area of the beam.

We now define an effective area for scattering within a certain solid angle $\Delta\Omega$,

$$\Delta A_{\text{eff}} = \frac{\Delta N_{\text{sc}}}{n_{\text{inc}}}$$

where ΔN_{sc} is the number of particles scattered into $\Delta\Omega$. This effective area is nothing but the cross section of the entire target, which is often macroscopic, and is expressed in terms of directly measurable quantities: the beam flux n_{inc} and the number of scattered particles ΔN_{sc} (counted by the detectors).

Assuming that we can estimate accurately how many scattering centers inside the target participate in the scattering process, and assuming that these N_{tar} scatterers contribute *independently*, we simply define the cross section as an effective area per scattering center:

$$\Delta\sigma = \frac{\Delta A_{\text{eff}}}{N_{\text{tar}}}$$

Substituting ΔA_{eff} from its definition, we have:

$$\Delta\sigma = \frac{\Delta N_{\text{sc}}}{n_{\text{inc}}\, N_{\text{tar}}}$$

In other words, the number of scattered particles is directly proportional with these three quantities: beam flux, number of scattering centers, and cross section; in fact, it simply given by their product:

$$\Delta N_{\text{sc}} = n_{\text{inc}}\, N_{\text{tar}}\, \Delta\sigma$$

We like to point out that, strictly speaking, the cross section is not a purely microscopic quantity; indeed, although it is a "per-particle" quantity, its very definition relies on certain simplifying assumptions regarding the macroscopic features of the concrete experimental situation.

We can define a differential cross section in the usual way: if the detectors have good angular resolution, we can make the solid angle $\Delta\Omega$ infinitesimally small, and we have

$$\frac{\Delta\sigma}{\Delta\Omega} \longrightarrow \frac{\mathrm{d}\sigma}{\mathrm{d}\Omega}.$$

When integrated over the solid angle, the differential cross section yields the total cross section:

$$\sigma_{\text{tot}} = \sum_{\Delta\Omega} \Delta\sigma = \int \mathrm{d}\Omega \, \frac{\mathrm{d}\sigma}{\mathrm{d}\Omega}$$

If we count all the particles scattered in every direction (except near the forward direction), i.e., $N_{\text{sc}} = \sum \Delta N_{\text{sc}}$, and assuming that we can neglect the contribution of forward scattering, the total cross section is

$$\sigma_{\text{tot}} = \frac{N_{\text{sc}}}{n_{\text{inc}} N_{\text{tar}}} = \frac{A_{\text{eff}}}{N_{\text{tar}}}$$

where $A_{\text{eff}} = N_{\text{sc}}/n_{\text{inc}}$ is the total effective area of the entire target.

The caveat we made regarding forward scattering stems from the fact that for vanishing scattering angle, the detectors will be flooded by the unscattered part of the beam; hence, the differential cross section cannot be defined in an operational way, except by extrapolation towards zero angle.

2.4.2 Formal definition of the cross section

The expression of the cross section in terms of the scattering amplitude is usually obtained directly from the asymptotic behavior of $\Psi_{\vec{p}}^{(+)}$ in Eq. (2.7), but such a derivation is only a convenient shortcut; its proper justification is through a time-dependent approach that uses normalized wavepackets. The time-independent approach is sometimes presented (especially at the introductory level) without enough emphasis on its connection with the time-dependent formalism. At the very least, it is necessary to see how the stationary scattering states are used to construct wavepackets whose time evolution is in accord with the actual scattering process. These wavepackets are then used to calculate the detection probabilities for a scattering experiment, and the celebrated formula for the cross section is obtained. We will sketch the derivation here.

The wavefunction $\Psi_{\vec{p}}^{(+)}(\vec{r})$ is a stationary state of H, and it provides a steady state picture of the scattering process; but, strictly speaking, $\Psi_{\vec{p}}^{(+)}$ cannot represent a physical state, because it is not square integrable. To overcome this difficulty, we need to construct a wavepacket as a superposition of many solutions $\Psi_{\vec{p}}^{(+)}$ integrated over a small domain centered around a fixed point $\vec{p}_1$ in momentum space. In other words, we have

$$\Psi^{(+)}(\vec{r}, t) = \int d^3\vec{p}\, \varphi(\vec{p})\, e^{-iEt}\Psi_{\vec{p}}^{(+)}(\vec{r})$$

where the "coefficients" $\varphi(\vec{p})$ are a square integrable function which is sharply peaked around $\vec{p} \approx \vec{p}_1$.

The competition between φ having nonzero values in a very small region in momentum space and the oscillating phase factors e^{-iEt} and $\Psi_{\vec{p}}^{(+)}$ as functions of $\vec{p}$ will determine the behavior of the wavepacket in the remote past and the distant future (before and after the collision). We first consider $t \to -\infty$. The time-dependent

28

phase factor $e^{-iEt} = e^{-itp^2/2\mu}$ is oscillating very fast as a function of $\vec{p}$, and it will cancel out the integrand almost everywhere; in particular, the contribution of the outgoing spherical wave vanishes for $t \to -\infty$. The only exception is the contribution of the plane wave term at certain locations; namely, those obtained by imposing the stationary phase condition for the combined phase factor $e^{-iEt}e^{i\vec{p}\cdot\vec{r}} = e^{i(\vec{p}\cdot\vec{r}-tp^2/2\mu)}$. Thus, in the remote past, our wavepacket has a group velocity $\vec{v}_1 = \vec{p}_1/\mu$, and it is localized far away from the interaction region, around $\vec{r}_1(t) = \vec{v}_1 t$, i.e., it is traveling along the direction given by our initial momentum $\vec{p}_1$. Before the collision, the wavepacket propagates almost freely and has a very well defined energy (given roughly by $E_1 \approx p_1^2/2\mu$).

For $t \to \infty$, the stationary phase condition for the outgoing spherical wave phase factor $e^{-iEt}e^{ipr}$ yields a nonzero contribution; namely, we obtain an expanding spherical shell of probability amplitude of radius $r \approx v_1 t$. Notice that for $t \to \infty$ there will also be a localized wavepacket (the unscattered part)[16] still traveling along $\vec{p}_1$.

The full details of this wavepacket approach can be found in many textbooks, e.g., see Messiah [17] for a derivation based on the position representation, and Taylor or

---

[16]In fact, the scattered portion of the wavepacket is only a very small fraction of the initial wavepacket; this is not at all a perturbative effect in the usual sense (indeed, the interaction potential V is not assumed to be small); instead, it is simply due to the great spatial extent of the initial wavepacket, which is much broader than the typical length-scale of the interaction $V(r)$. Thus, most of the initial wavepacket is simply unaffected by the potential $V(r)$, and we can take the following view of the scattering process: long after the collision, the wavepacket is a superposition of the (spherical) scattered wave and the completely unscattered initial wavepacket. This simple physical picture is not approximate, as it stems from the equation that relates the S operator and the T-matrix, see Sec. (2.2.5). After the collision, the unscattered wavepacket, which is simply the freely propagated initial wavepacket, will be located within a very narrow solid angle around the forward direction (because of its tight initial collimation); indeed, it will remain within a narrow cone defined by the small angle $\Delta\theta = \frac{\Delta p_\perp}{p_1} \ll 1$ (assuming a very small momentum spread $\Delta p_\perp$ in the transverse directions). Thus, the two wavepackets (scattered and unscattered) will overlap only within this cone, and they will interfere; it is this destructive interference near the forward direction which ensures that the total probability adds up to unity. By making use of the unitary character of the time evolution in this very direct and intuitive way, we can actually prove the optical theorem; this is a tedious mathematical exercise, but it has great appeal on the physical side.

Newton [16, 15] for a calculation in the momentum representation. The key result is that the cross section for scattering from an initial direction $\vec{p}_1$ into an infinitesimal cone $d\Omega$ centered around $\vec{r}$ is

$$\frac{d\sigma}{d\Omega} = \left| f_{\vec{p}_1}(\hat{r}) \right|^2 \tag{2.8}$$

This result looks remarkably simple, but one should not forget that its derivation makes use of a number of assumptions. The projectile beam is assumed to be well collimated and nearly monoenergic, such that the momentum dependence of $f_{\vec{p}}$ is very broad compared to the initial momentum distribution function; if $\varphi(\vec{p})$ were not sufficiently peaked around $\vec{p} \approx \vec{p}_1$, then a wider range of momenta would need to be integrated over, and $f_{\vec{p}}$ could not be pulled outside the integral anymore. Also, we need to average over many wavepackets distributed uniformly in the plane transverse to the initial direction of propagation. Only then, does the final result for the cross section reduce to the simple expression given in Eq. (2.8) above. Moreover, other simplifying conditions are assumed, as discussed earlier in this chapter in Sec. (2.1).

2.4.3 Probability depletion in a scattering event

It is very fortunate that the simple expression of the cross section can be derived without considering the details of the time evolution of the wavepacket during the collision itself. But it is instructive to picture this evolution, as it gives us a fuller picture of the scattering process. Despite its intricate details, the scattering event has a certain simplicity—during the time it takes the wavepacket to pass through the scattering center, the latter will act as a source for the outgoing spherical wave. Thus, apart from the short transient times just before and just after the collision, the incident wavepacket suffers a steady depletion of probability during the interaction time.

Assuming that the wavepacket has a length and width that are very much larger than the interaction range (assumed finite, for simplicity), i.e., the wavepacket is spread very thin over a large volume, the total depletion caused by scattering will be small compared to unity. However, this is not a perturbative effect in the usual sense, as already mentioned in the last footnote.

2.5 The scattering amplitude

It is now clear that the main goal in a scattering problem is the computation of the scattering amplitude, and we now devote our attention to it. We first recall an integral representation for the scattering amplitude:

$$f_{\vec{p}_1}(\hat{p}_2) = -\frac{2\pi\hbar^2}{\mu} \int d\vec{r}' \, e^{-i\vec{p}_2 \cdot \vec{r}'} V(\vec{r}') \, \Psi_{\vec{p}_1}^{(+)}(\vec{r}')$$

where we have set $\vec{p}_1 \equiv \vec{p}$ and $\vec{p}_2 \equiv p\hat{r}$. Evidently, $p_1 = p_2 \, (= p)$ which is a consequence of energy conservation. In the equation above, the integral has the appearance of a matrix element and it can be rewritten in bra-ket notation

$$f(\vec{p}_2 \leftarrow \vec{p}_1) = -\frac{2\pi\hbar^2}{\mu} \langle \Phi_{\vec{p}_2} | V | \Psi_{\vec{p}_1}^{(+)} \rangle$$

Here we have also changed the notation for the scattering amplitude to better show that the scattering process can be regarded as a transition between two momentum states: the initial state with momentum $\vec{p}_1$ and the final state with momentum $\vec{p}_2$. Notice that f does not depend on six independent variables, but only five (at most); indeed, due to conservation of energy, we have $p_1 = p_2 = \sqrt{2\mu E}$ and a better notation would be $f_E(\hat{p}_2 \leftarrow \hat{p}_1)$, in which the energy is shown as a parameter. Yet a

different style of notation could be used to emphasize the energy dependence, namely $f_{\hat{p}_2 \leftarrow \hat{p}_1}(E)$. All these notations are, of course, equivalent:

$$f_{\vec{p}_1}(\hat{p}_2) \equiv f(\vec{p}_2 \leftarrow \vec{p}_1) \equiv f_E(\hat{p}_2 \leftarrow \hat{p}_1) \equiv f_{\hat{p}_2 \leftarrow \hat{p}_1}(E).$$

$$T_{\vec{p}_2 \vec{p}_1} = \langle \Phi_{\vec{p}_2} | T | \Phi_{\vec{p}_1} \rangle = \langle \Phi_{\vec{p}_2} | V | \Psi_{\vec{p}_1}^{(+)} \rangle. \tag{2.9}$$

$$f(\vec{p}_2 \leftarrow \vec{p}_1) = -\frac{2\pi\hbar^2}{\mu} T_{21}. \tag{2.10}$$

This tells us that the T-matrix is just the scattering amplitude under a different name, and we may wonder as to why it has to be introduced at all. Two reasons: one is tradition, and the other is its usefulness as a concept in the formalism (see Taylor).

The coefficient in Eq. (2.10) changes when we change the normalization of the free states, and this can generate a great deal of confusion. We end this section with a discussion that is meant to clarify this point. In Eq. (2.7), where the scattering amplitude was first introduced, the plane-wave term had unity coefficient; this corresponds to a specific choice for the normalization of the free particle eigenfunctions, namely

$$\langle \Phi_{\vec{p}} | \Phi_{\vec{p}'} \rangle = \langle e^{i\vec{p}\cdot\vec{r}} | e^{i\vec{p}'\cdot\vec{r}} \rangle = (2\pi)^3 \delta(\vec{p} - \vec{p}')$$

This normalization is also inherited by the scattering solutions; in general, we have

$$\langle \Psi | \Psi' \rangle = \langle \Phi | \Phi' \rangle,$$

whatever the choice of the generalized normalization of the free states is (this is ensured by the fact that the Møller operators are isometric, se Ref. [15]). In the next chapter we will present the angular momentum analysis of the scattering states $\Psi_{\vec{p}}^{(+)}$.

Chapter 3

Partial wave analysis, and computational details

3.1 General remarks for non-separable problems

The Schrödinger equation (2.6) is not usually attacked numerically directly as a 3-dimensional problem; instead, the general approach for a multi-variable problem is to reduce it to a single variable. This is achieved by expanding the full wavefunction Ψ in a basis of functions of all variables except one; the "coefficients" of such an expansion will be functions of the remaining variable. If the potential V (in general, if the Hamiltonian H) is not separable, one obtains a (possibly infinite) set of coupled differential equations; this new problem may seem daunting, but it is more manageable than the original multi-variable problem. From the mathematical and computational points of view, the advantage of this approach is that we have to deal with ordinary differential equations (albeit coupled); from the physical point of view, such an approach is advantageous because when the problem is formulated in one radial-type variable, it is naturally suited for the fact that the interaction potential vanishes in the limit of infinite separation between target and projectile.

We now illustrate this approach for the simple case of potential scattering; we will consider the general situation when $V(\vec{r})$ does not have spherical symmetry. This exercise may seem unnecessarily complicated, but we will see that it provides a more thorough understanding of both the practical and formal aspects of scattering theory;

its complications are actually welcome, as they anticipate some of the more serious difficulties that larger problems have.

3.2 An instructive exercises: partial wave analysis for potential scattering without spherical symmetry

The scattering theory is usually introduced for the simple case of potential scattering with spherical symmetry. For such a simple problem, angular momentum is conserved; thus, we take advantage of rotational invariance by using the angular momentum representation, where the S-matrix has the simplest form. However, the angular momentum representation is useful even if the Hamiltonian doesn't have rotational invariance (which is the case if V doesn't have spherical symmetry).

The key to the angular momentum analysis is the plane wave expansion formula:

$$e^{i\vec{p}\cdot\vec{r}} = \frac{4\pi}{pr} \sum_{\ell m} i^\ell Y_{\ell m}(\hat{r})\, u_l(pr)\, Y_{\ell m}^*(\hat{p}), \tag{3.1}$$

where $u_l(z) = z j_l(z)$ are the Riccati–Bessel functions, and $Y_{\ell m}$ are the spherical harmonics.

For the full problem, we seek a similar expansion of the scattering solution,

$$\Psi_{\vec{p}}^{(+)}(\vec{r}) = \sum_{\ell m} \psi_{\ell,m}(\vec{p},r)\, Y_{\ell m}(\hat{r})$$

In the general case of (without spherical symmetry) we need to further expand $\psi_{\ell,m}(\vec{p},r)$ with respect to $Y_{\ell m}^*(\hat{p})$

$$\psi_{\ell,m}(\vec{p},r) = \sum_{\ell',m'} \psi_{\ell,m;\ell',m'}(p,r) Y_{\ell'm'}^*(\hat{p}),$$

35

Finally, one arrives at a radial problem, which is a system of coupled radial equations for the components $\psi_{\ell,m;\ell',m'}$

$$\left(\frac{d^2}{dr^2} + p^2\right)\psi_{\ell,m;\ell',m'} = \sum_{\ell'',m''} V_{\ell'm',\ell''m''}\psi_{\ell'',m'';\ell',m'}$$

Thus, even for the single channel case, a scattering problem can be rather large and it can pose serious computational challenges.

The solutions of the system of coupled equations are specified by imposing scattering type boundary conditions in the asymptotic region:

$$\psi_{\ell,m;\ell',m'}(p,r) \sim e^{-ipr}\delta_{\ell\ell'}\delta_{mm'} - S_{\ell m,\ell'm'}e^{ipr}$$

The S-matrix is extracted, and the cross section can be expressed in terms of its matrix elements.

3.3 Collisions with rearrangement

We discuss atom–diatom reactive scattering in this chapter, which is a particular example of a three-body problem; although this is one of the simplest cases of collisions involving rearrangement, the full quantum mechanical solution is notoriously difficult, even for energies below three-body breakup. Apart from having to deal with many degrees of freedom, the very choice of a convenient set of coordinates is problematic. This difficulty stems from the fact that the coordinates which are most suitable at large separations—the Jacobi coordinates—are different for each arrangement. This obstacle can be circumvented in various ways, e.g., using methods based on the variational approach, which employ traditional basis sets or discrete variable representations [18] to make the scattering problem similar to a bound state problem;

36

also very popular are close-coupling methods using hyperspherical coordinates, which require solving a large system of coupled differential equations along the hyperradius. The later approach, as implemented in the ABC computer code [10], is the one we used here.

Manolopoulos and coworkers [10] developed their ABC code based on Delves [19] hyperspherical coordinates. Note that a separate set of Delves hyperspherical coordinates is defined for each arrangement; however, they share the same hyperradius coordinate, which makes it possible to simultaneously use all sets of Delves coordinates for a given problem. Indeed, the full wavefunction can be expanded in eigenbases corresponding to internal motion coordinates for each arrangement (after the combined multiple-arrangement basis is orthogonalized). The resulting hyperradial coupled-channel equations are then solved using the log derivative method [20]. The propagation starts at $\rho = \rho_{\text{min}}$ (where the potential is highly repulsive), and ends at a sufficiently large $\rho = \rho_{\text{max}}$, where the S-matrix is extracted by imposing asymptotic boundary conditions.

The expression for the state-to-state cross sections, integrated over all scattering directions, averaged over the initial rotational states of the reactant dimer, and summed over the final rotational states of the product, reads

$$\sigma_{n' \leftarrow n}(E) = \frac{\pi}{k_n^2} \sum_{J=0}^{\infty} \left(\frac{2J+1}{2j+1} \right) \sum_{\ell=|J-j|}^{|J+j|} \sum_{\ell'=|J-j'|}^{|J+j'|} \left| T^J_{n'\ell', n\ell}(E) \right|^2 , \tag{3.2}$$

where the generic notation n stands for the arrangement label and quantum numbers of the diatom states, $n = (a\,vj)$, and $k_n = \sqrt{2\mu_a E_{\text{kin}}}$ is the initial momentum ($\hbar = 1$, atomic units are used); μ_a the reduced mass of the binary system atom–diatom in the initial arrangement (a), the initial kinetic energy is $E_{\text{kin}} = E - \varepsilon_n$, and ε_n is the rovibrational energy of the diatom. E is the total energy, J is the total angular

momentum, and ℓ is the initial angular momentum for the relative motion. $T^J_{n'\ell',n\ell} = \delta_{n'n}\delta_{\ell'\ell} - S^J_{n'\ell',n\ell}$ is the T-matrix.

Except for the particular case of very low initial kinetic energy, obtaining fully converged results is very expensive computationally; indeed, the truncation of the infinite sum in Eq. (3.2) needs to include a sufficiently large number of terms. Although all J-blocks are separate from each other (due to conservation of total angular momentum), they quickly become formidable computational tasks; for large J, the coupled problem becomes prohibitive due to its sheer size, unless the number of channels is also truncated severely. In the ultracold regime, there is a great simplification, as the number of significant J-terms reduces drastically; when the initial kinetic energy is sufficiently low, only s-wave ($\ell = 0$) collisions remain, while higher partial waves ($\ell \geq 1$) become negligible due to centrifugal barriers. Note that the s-wave contribution is contained only in the $J = j$ block (j is the rotational quantum number of the initial state of the diatomic reactant). If the initial state has large j, the s-wave block can still be rather large, especially if many vibrational states are involved.

3.4 Convergence tests

Our numerical results were obtained with the computer code ABC developed by Manolopoulos [10]; in their early work, ABC was tested at high energies for a number of benchmark systems such as D+H$_2$, Cl+H$_2$, F+H$_2$, and their isotopic counterparts [21, 22, 23, 24, 25]. Subsequently, modified versions of this code have been used by other groups to study certain benchmark chemical reactions in the ultracold regime[26, 27, 28, 29, 30]. In order to use the ABC code at ultralow kinetic energy in a reliable way, we have also made certain modifications in its structure; most important in our implementation is the ability to follow the progress of convergence in great detail. We typically monitor the convergence simultaneously for a large number of collision

energies and for many initial states $H_2(v, j = 0)$ in a single large run. We have also implemented a save-and-restart feature, which is extremely convenient, as it allows us to go back and extend the radial propagation of a given run after it has ended (normally, or prematurely by accident).

In order to understand the various issues regarding convergence, we performed numerous tests (which were rather expensive, despite the current advances in computational power). Also, we spent a significant amount of time and effort to analyze the results of these tests, and we present our findings for $D + H_2$ reaction. The rovibrational levels of H_2 and HD are shown in Fig. 3.1 for reference.

Generally speaking, the main questions regarding convergence are:

(i) is the target basis large enough?

(ii) is the hyperradius integration step $\Delta\rho$ small enough?

(iii) is the maximum hyperradius ρ_{max} large enough?

The last question stems from simple considerations of energy scales; namely, we need to satisfy $|V_{nn'}(\rho)| \ll E_{kin}$ in the asymptotic region ($\rho \to \infty$). For scattering at high energy, these asymptotic conditions are easily fulfilled when ρ_{max} corresponds to separations of roughly 15–20 Bohr radii. However, in ultracold collisions, the initial kinetic energy in the entrance channel can be of the order of $1\,mK$ ($10^{-7}\,eV$) or even much smaller, and it requires us to propagate the numerical solutions far into the asymptotic region; for the DH_2 system, we typically end the propagation at $\rho_{max} = 40$ a.u. (atomic units), because the long range van der Waals forces are fairly weak. Note that for other systems, e.g., atom–atom scattering with heavy alkali species, the long range interactions are much stronger and have a significant effect even at distances of a few hundred Bohr radii. Also, the reduced mass of the binary collision has a compounding effect; indeed, when $E_{kin} \to 0$, the local momentum in the

39
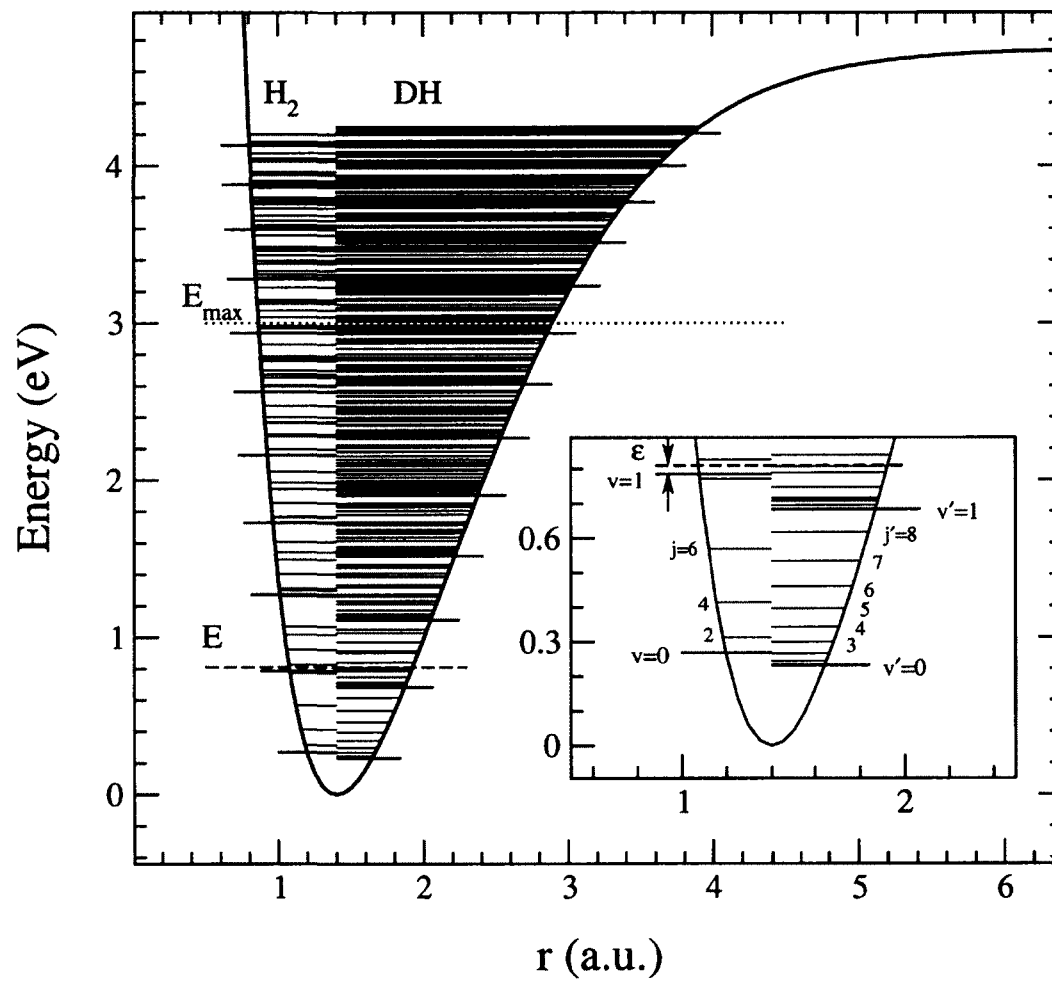
Figure 3.1 — Rovibrational levels of H_2 and HD
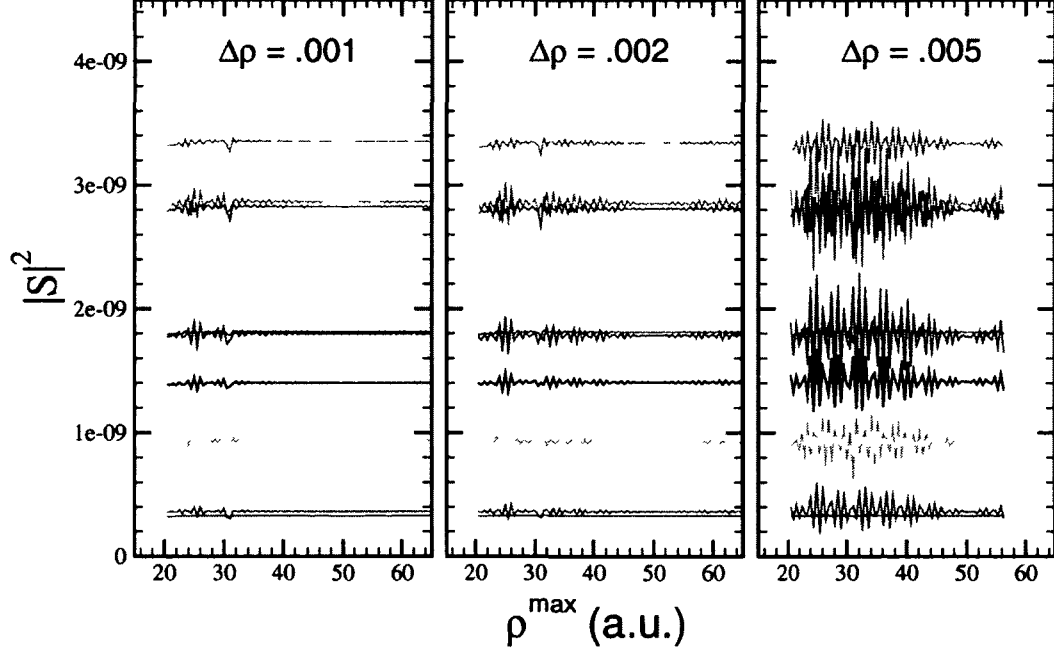
Figure 3.2 — Convergence with respect to ρ_{max} and $\Delta\rho$. The curves represent $|S_{a'v'j',avj}|^2$ for initial state $v = 1$, $j = 0$ in arrangement a $= 1$ (H_2) and final states $v' = 0$, $j' \leq 8$ in arrangement a$' = 2$ (DH). Note that we omitted the subscripts $\ell = 0$ and $\ell' = j'$. The kinetic energy is $E_{kin} = 1$ K, and the truncation energy $E_{max} = 2.5$ eV, and the total angular momentum $J = 0$.

entrance channel is approximately given by $k_{loc}(\rho) \approx \sqrt{2\mu V(\rho)}$, and the enhancement coming from a large reduced mass needs to be compensated by the decrease of the diagonal potential $V(\rho)$ at larger distances.

We also need to pay special attention to the size of the integration step $\Delta\rho$. Indeed, in the ultracold regime, the amplitudes of the inelastic components of the scattering solution follow a simple scaling law, $\psi_n \sim k$, assuming the normalization is such that the entrance (elastic) channel component oscillates with unit amplitude as $\rho \to \infty$. Thus, relative to the asymptotic amplitude of the entrance channel component, all other components become vanishingly small when $k \to 0$. To ensure that we obtain reliable results, we need high numerical precision because of the smallness of the inelastic components of the wavefunction. This is very important for low initial

vibrational dimer (H_2) states; $v = 0$ is an especially difficult case, as it also suffers from a strong barrier suppression effect, and the reactive components of the wavefunction are extremely small even at high energies ($\lesssim 10^3$ K). Computationally, a small step size is rather expensive, e.g., reducing $\Delta\rho$ by only a factor of two will double the run time. From a practical standpoint, it is thus desirable to find a good compromise between adequate numerical accuracy and speed of computation. We have done thorough testing to find such an optimal middle ground, and we illustrate our findings in Fig. 3.2, which shows the gradual improvement of the results when the step size $\Delta\rho$ is reduced. Note that the propagation step has to be quite small to reach full convergence. The results obtained with a slightly larger step size seem to oscillate around the converged values; however, care is needed, as the oscillations can have large amplitudes.

We now consider the difficult question regarding the size of the target basis. Note that, in general, apart from the degrees of freedom of the target itself (i.e., rovibrational motion of H_2 and DH), the so-called target basis also includes one degree of freedom for the rotational part of the relative motion. We present results only for the s-wave contribution, as we are interested in the ultracold regime; for a given initial rotational quantum number j of the dimer, $\ell = 0$ is contained only in the block with $J = j$, which is thus the only one we consider at ultralow collision energies. In our exploration of high vibrational states, we have limited ourselves to initial states with $j = 0$; hence, we always have $J = 0$, which is a great advantage, as it keeps the problem small (albeit still challenging). It follows that in this particular case, the target basis does contain only target states, since for any value j', the quantum number of the orbital angular momentum is fixed ($\ell' = j'$); consequently, the degree of freedom corresponding to relative orbital angular momentum does not augment the basis size; note, however, that the fixed values $\ell' = j'$ can be rather large, and are fully relevant

in the scattering problem (e.g., in constructing the matrix elements of the couplings, or in extracting the S-matrix).

The approach employed in ABC uses Delves hyperspherical coordinates [31], in which different arrangements are treated separately with regards to the internal motion coordinates. For each arrangement, a basis is constructed depending mainly on two truncation parameters: $E_{\max}$, and $j_{\max}$ (see Fig. 3.1). For a given initial dimer state $\{v, j\}$ with channel energy ε_{vj}, the total energy is $E = \varepsilon_{vj} + E_{\text{kin}}$. In the ultracold regime E_{kin} is vanishingly small, and all channels above the initial one are closed; indeed, there isn't sufficient energy for their excitation, and the collision is completely exoergic. However, many of the closed channels play an important role, and we need to find out how many of them to include; hence, we repeat the computation for increased values of $E_{\max}$, in order to obtain converged results. The truncation of channels is straightforward; namely, all channels with dimer eigenenergies below $E_{\max}$ are included, and all channels above $E_{\max}$ are ignored. In a similar fashion, the cutoff parameter $j_{\max}$ can be used to control the truncation of the number of rotational eigenstates of both dimers; however, in order to ensure that our computation is very nearly exact, we have eliminated the need for $j_{\max}$ by always including all j states that are energetically relevant (i.e., all open and closed channels below $E_{\max}$ are included, no matter how large their quantum number j is). Note that the dimer energy eigenbasis is constructed from a primitive particle-in-a-box basis, which depends on the size of the box in the radial-like coordinate for each dimer; also, there are additional parameters controlling the quadratures used in computing matrix elements, and we performed separate tests in which we varied these parameters.

As expected, care is needed to ensure convergence with respect to the number of closed channels. This is especially difficult for high vibrational states; not only does the size of the problem increase as we approach the threshold from below, but

43
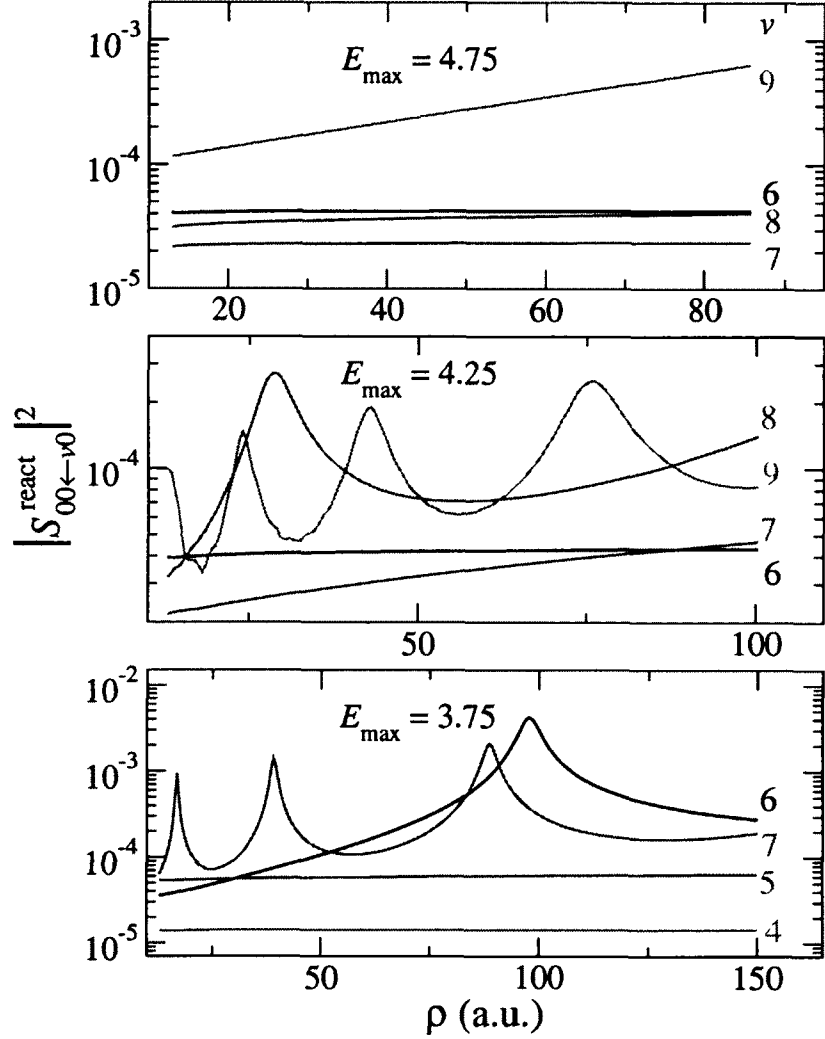
Figure 3.3 — Convergence of the S-matrix with respect to ρ_{max} for different values of E_{max}. In order to be fully specific, we show results for a particular final state, namely $DH(v' = 0, j' = 0)$ at a fixed kinetic energy $E_{kin} = 1\ \mu K$; the state-to-state results for all other final states are similar. The different curves are for different initial states $H_2(v, j = 0)$ and each value of v is shown next to the corresponding curve.

we eventually need to include the dimer continuum (in a discretized fashion). We did attempt such a computation, but we obtained results that were incorrect (judged by comparing them with runs for lower $E_{\max}$). We speculate that this failure stems from an overcompleteness issue; in other words, there is too much linear dependence in the combined dimer bases of the separate arrangements. This obstacle could be circumvented, at least in principle, but we haven't pursued this issue. The problem simply becomes prohibitively expensive when a significant part of the continuum needs to be included, and we decided to stop just shy of the threshold. With this elaborate caveat, we are now ready to present the concrete technical details of our results for $E_{\max}$ convergence.

In Fig. 3.3, we show results from our convergence study for high vibrational initial states of H_2. It is readily apparent that the gradual improvement is rather slow when $E_{\max}$ is increased; e.g., if we follow $v = 7$ in Fig. 3.3, from the bottom panel to the top one, we see that its $\rho_{\max}$ behavior only shows stabilization for the highest cutoff energy used ($E_{\max} = 4.75$ eV, which was roughly at the dissociation threshold of the dimer). Note that we only obtained converged results for initial vibrational states $v \lesssim 8$. Regarding the difficulty of obtaining converged results for high v, we emphasize the strong connection between the $E_{\max}$ convergence and the $\rho_{\max}$ convergence, which is apparent in Fig. 3.3. Strictly speaking, the stabilization of the results at large $\rho_{\max}$ does not guarantee convergence, but when the results remain unchanged for increased values of $E_{\max}$, we consider that we have achieved convergence. As we see in Figs. 3.2 and 3.3, the radial integration only needs to be propagated out to modest values of $\rho_{\max}$, because the results stabilize rather quickly if $E_{\max}$ is sufficiently high. Conversely, if the results are not converged at these moderate distances, they cannot be improved by extending the propagation to larger distances, and it is very likely that $E_{\max}$ is simply too low. There is one exception to this empirical rule: if there is a
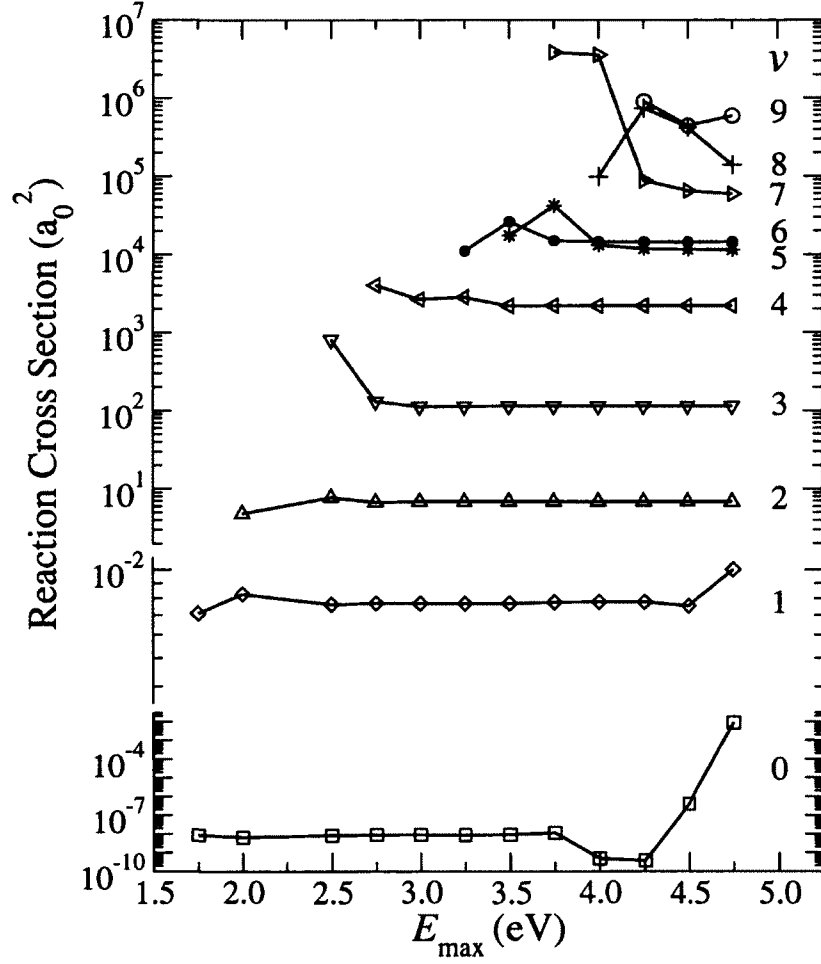
Figure 3.4 — Variation of numerical results when increasing $E_{\max}$ up to 4.75 eV (near the continuum threshold of H_2). The vibrational quantum number of the initial dimer state is specified next to each curve. Note that the vertical axis is broken twice (below and above $v = 1$). Based on the convergence results shown in this graph, we determined which value of $E_{\max}$ is optimal for different initial v. Thus, we extracted our final results according to the following choices: $E_{\max} = 3.5$ eV for $v \leq 2$, $E_{\max} = 4.25$ eV for $3 \leq v \leq 6$, and $E_{\max} = 4.75$ eV for $v \geq 7$.

46

resonance near the threshold, then it will amplify the long range sensitivity, and ρ_{max} will need to be much larger. Also, special attention needs to be paid to the diagonal matrix element for the entrance channel, as its complex phase $\phi = \arg(S_{ee})$ is very sensitive to ρ_{max} even in the absence of threshold resonances; this is well known from the simpler case of purely elastic (single channel) scattering.

In our pursuit of understanding the various aspects of convergence, we have amassed a substantial amount of numerical results, which we summarize in Fig. 3.4. This graph contains another unpleasant surprise, this time regarding initial states with low v. In the bottom right corner, we see that the results for $v = 0$ and $v = 1$ show a wild variation for large values of the truncation energy E_{max}. This instability stems from the fact that the cross sections for the lowest vibrational states have extremely small values, and are thus very sensitive with respect to changing certain parameters of the numerical problem; specifically, those matrix elements of S that are very small become less accurate when the number of channels is increased above a certain value. With the benefit of hindsight, we can say that this anomaly should have been expected, especially for $v = 0$; however, despite this instability, there is still a plateau of converged results for E_{max} between 2.5 eV and 3.5 eV. Next, for intermediate values of the initial vibrational number ($v = 2, 3, \cdots, 7$), we obtain converged results when the number of channels included is sufficiently large, i.e., the results become stable when E_{max} is increased; as seen in Fig. 3.4, they are much more robust than $v = 0$ and $v = 1$. For $v = 8$, the results barely begin to converge at $E_{max} = 4.75$ eV, judging by the ρ_{max} behavior in the top panel of Fig. 3.3. We also obtained results for $v = 9$ (shown in Figs. 3.3 and 3.4) and $v = 10$, 11 (not shown), but they are not fully converged.
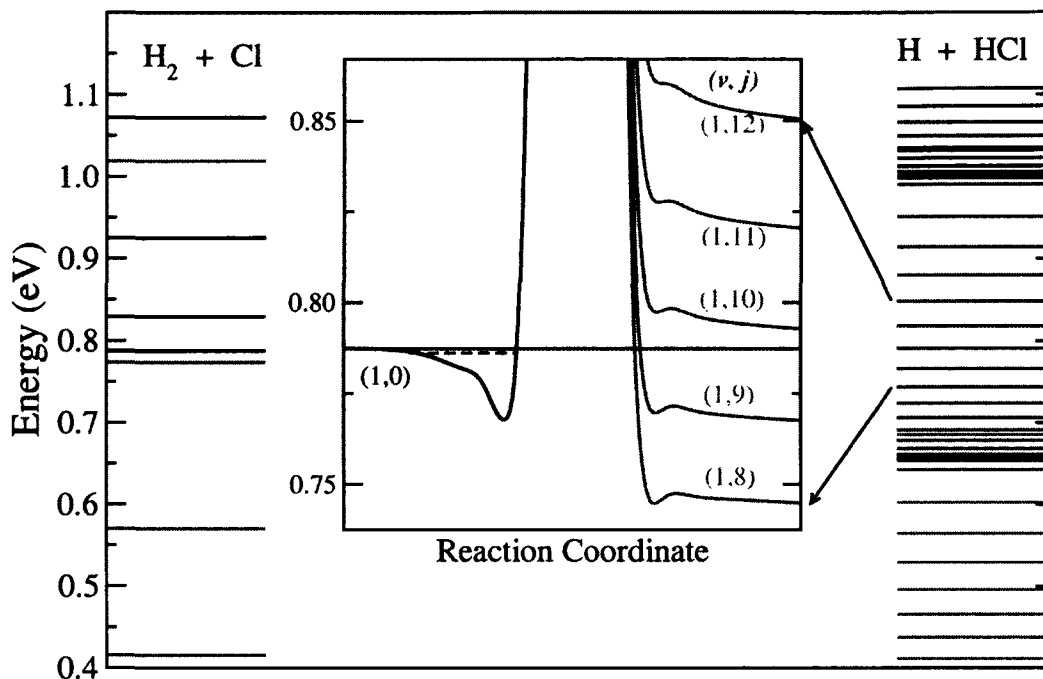
Figure 3.5 — Rovibrational levels of Cl—H$_2$ and HCl—H

3.5 Special case: Resonance

We have so far discussed the general issues of convergence for ultracold collisions. But, near a resonance very close to the asymptote, obtaining converged results become much more difficult. Generally, in presence of a bound or anti-bound (virtual) state close to the threshold of the entrance channel, the magnitude of the scattering length becomes huge, creating a dramatic enhancement in the reactive scattering. We have explored the effect of the resonance on low energy scattering by varying continuously the reduced mass of the reactive system (particularly, the mass of the hydrogen atoms); this approach, which is similar to the more direct approach of modifying the potential surface itself [32], has been used before to study the effect of a threshold resonance in the F + H$_2$ reaction [33]. We emphasize that the exercise of varying the mass continuously can be very instructive even when an extremely accurate surface is available.

We discuss the convergence issues in the s-wave threshold resonances using the example of the $Cl + H_2(v = 1, j = 0) \rightarrow HCl(v', j') + H$ reaction. The rovibrational ground state ($v = 0$, $j = 0$) of HCl is energetically higher than that of H_2; thus, in order to make the $Cl + H_2 \rightarrow HCl + H$ reaction possible in the ultracold regime, we use ($v = 1$, $j = 0$) as initial state of H_2. This reaction is particularly interesting since it can support quasibound Cl—H_2 van der Waals complexes in the shallow potential well of the entrance arrangement (see Fig. 3.5) [34]. Due to the barrier, the reactivity in this system is very low. This makes it possible for the resonance pole associated with an energy level of the van der Waals complex to be located very close to $E = 0$ in the complex plane, which dramatically affects the threshold behavior, see Chap. 6. Note that, when the mass of the hydrogen atoms are modified, the channel thresholds in both arrangements will shift; however, near the entrance channel, there cannot be any Feshbach resonances from the closed channels in either arrangement (see inset in Fig. 3.5). Indeed, in the entrance arrangement, the nearest ($v = 1, j = 2$) closed channel in the entrance arrangement is too high energetically, while in the product arrangement, the effective van der Waals potential curves for the relevant channels (shown in the inset in Fig. 3.5) cannot hold any quasibound states for the H—HCl complex. Recall that we have $J = 0$ for the total angular momentum; thus, the orbital angular momentum ℓ' for any channel (v', j') is $\ell' = j'$. Consequently, for high rotational diatomic levels, the centrifugal term is large and it will make the van der Waals potential well disappear.

At very low kinetic energy, it is the elastic phase of the S-matrix, $\phi = \arg(S_{e,e})$, that is most sensitive to ρ_{max} convergence. This is especially important in the resonant case, which we illustrate in Fig. 3.6, where we see that $\phi(\rho_{max})$ requires extremely large values for ρ_{max} in order to reach convergence. We stress that, for a large scattering

problem that is highly elastic (low reactivity), the behavior of the elastic phase ϕ is very similar to that of the single channel phaseshift.
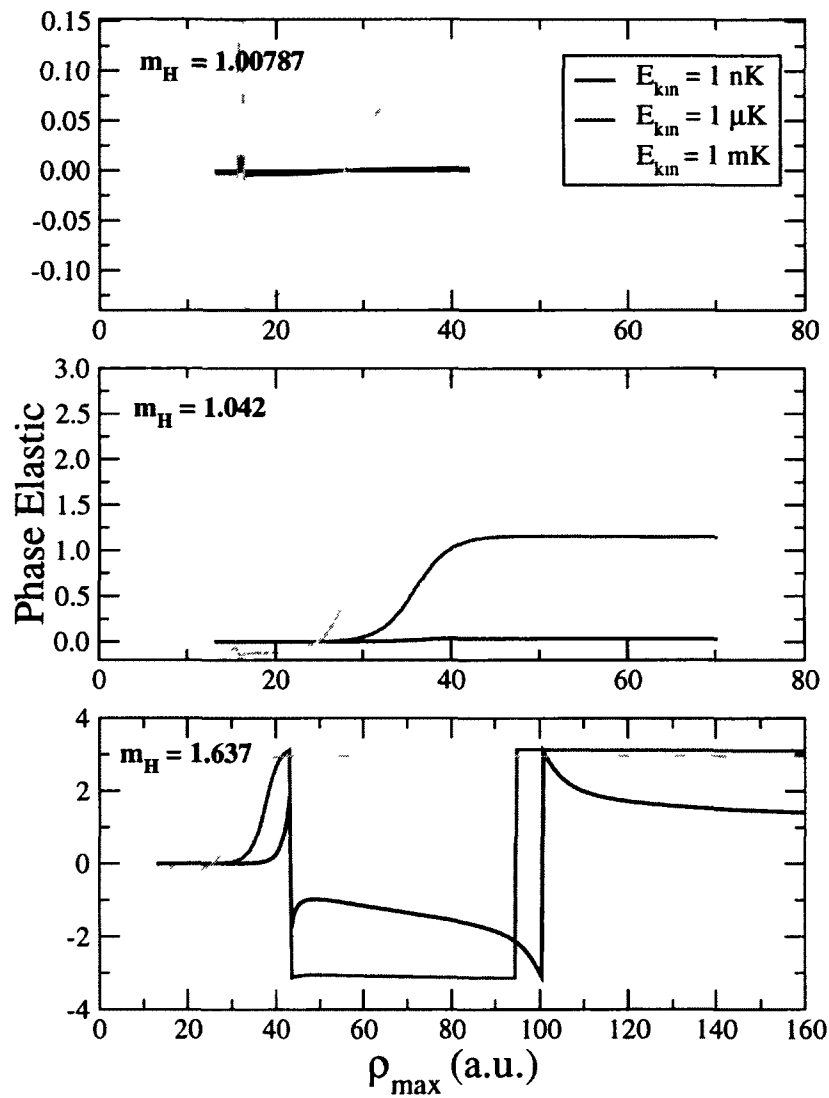
Figure 3.6 — Elastic phases of $Cl + H_2(v = 1, j = 0) \rightarrow HCl(v', j') + H$ reaction for three difference masses of H.

Chapter 4

D–H$_2$ collisions in the ultracold regime

Among the systems with a reaction barrier, $D + H_2 \rightarrow DH + H$ is one of the benchmark cases, and it has been extensively studied at high energies. Our work is focused on the ultralow (sub-Kelvin) energy regime, which makes the collision problem extremely sensitive to the details of the potential energy surface (PES), and places taxing demands on the numerical accuracy of the PES. From the point of view of electronic structure, this system is rather small, which made feasible the computation of a potential energy surface (PES) that is comparatively accurate.[11]

Our main goal is to understand the role of the initial vibrational excitation of the reactant in the ultracold reaction $D+H_2(v) \longrightarrow H+HD$. Although we are particularly interested in the case of a highly excited target, we did an exhaustive study of all possible values of v; however, as we have mentioned in the previous chapter, the computation becomes prohibitive for the very high vibrational states ($v \geq 8$), so we present here results with sufficient confidence up to initial states with $v \leq 7$. Since we had to perform many tests, which were computationally expensive for high values of v, we kept all other aspects of the problem small; specifically, we only studied the $j = 0$ initial states of H$_2$. Moreover, the s-wave contribution is dominant at ultralow kinetic energy; hence, we only computed the contribution for total angular momentum $J = j = 0$. Nevertheless, the computational work was still challenging, as we included all possible open channels in both arrangements, and also a sufficiently large number of closed channels.

4.1 Vibrationally excited target in ultracold reactions

In Fig. 4.1 we show the probabilities for exoergic inelastic and reactive scattering, which we define as $\sum_{v'} \sum_{j'} |S_{v'j',v0}|^2$, where the sums extend over all open channels in a specific arrangement which are below the entreance channel. Thus, for the entrance arrangement, we only consider the final states $H_2(j', v')$ for quenching, $\varepsilon_{v'j'} < \varepsilon_{v0}$, and similarly for reaction, i.e., $HD(j'', v'')$ with $\varepsilon_{v''j''} < \varepsilon_{v0}$ in the product arrangement. Note that, to simplify notation, we omitted the arrangement labels and the quantum numbers $J = 0$, $\ell = 0$ and $\ell' = j'$. According to our choice, the initial rotational state of H_2 has $j = 0$, while v specifies its initial vibrational state. For low values of v, we distinguish two very different regimes: the Wigner regime at very low kinetic energy, followed by a gradual transition (at $E_{kin} \approx 0.1$–10 K) into the barrier dominated regime at higher energies (100–10^3 K). According to Wigner's law [14], the probabilities for inelastic and reactive scattering behave as $E_{kin}^{1/2}$ at ultralow energy, and they vanish when $E_{kin} \to 0$; this simple power law behavior produces straight lines on our log-log graphs in Fig. 4.1, with a slope of $\frac{1}{2}$. This threshold behavior stems from the simple energy scaling of the wavefunction at vanishing kinetic energy.

For the special case $v = 0$, there is no vibrational motion to be quenched; the reaction, however, can occur even at vanishing kinetic energy. The product (HD) arrangement has three channels ($v' = 0$, $j' = 0, 1, 2$) below the entrance channel $H_2(0,0)$; these channels are thus always open, but the reaction probability is greatly reduced at low kinetic energy, due to the reaction barrier. We see in Fig. 4.1 that the reaction probability for $v = 0$ shows a sharp drop off, when the kinetic energy decreases from a few thousand Kelvins to energies of the order of 10 K. We recall that our results only include the s-wave contribution, which dominates all other partial waves only for kinetic energies below 0.1 K; above this energy, higher partial waves
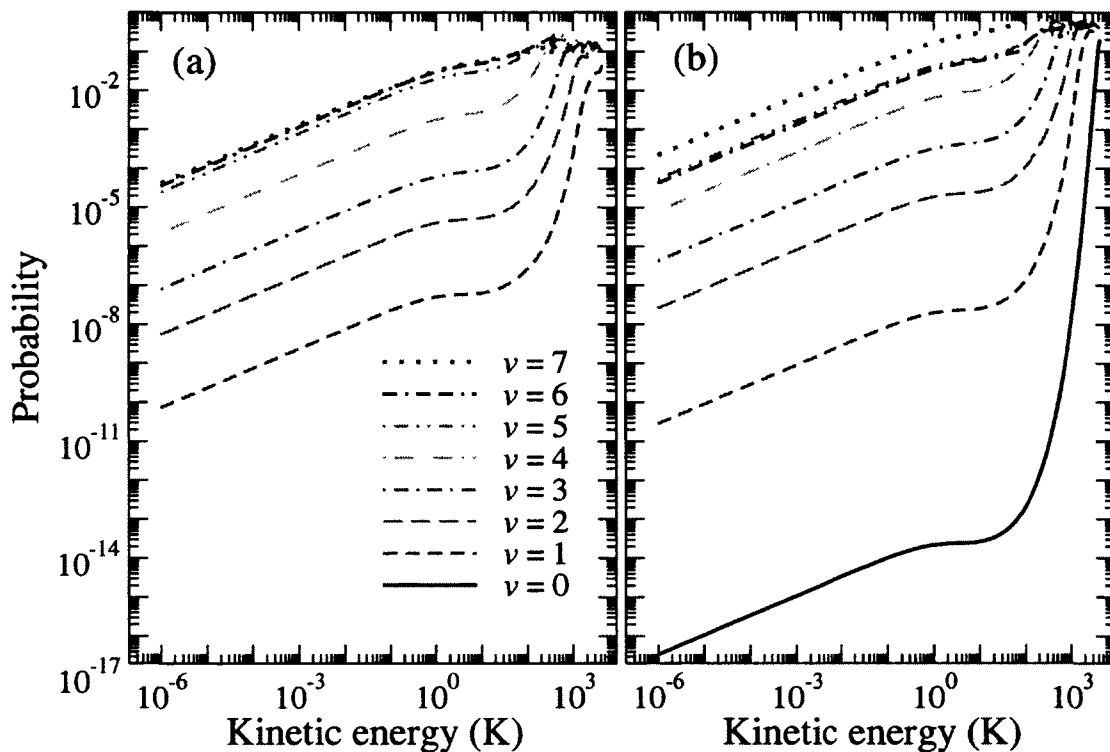
Figure 4.1 — Kinetic energy dependence of the probabilities for quenching (a) and reaction (b). Each curve in panel (a) is paired with a similar one in panel (b) and they both correspond to a certain initial vibrational state of H_2 as shown in the legend. For $v = 0$, all open channels belong to the product (DH) arrangement; thus, the curve for quenching is absent in panel (a).

will begin to contribute substantially, and they would need to be included in the full results.

Although we focus on the ultracold regime, the broad scope of our s-wave results, from ultralow to high energy, helps to illustrate the stark difference between the barrier-dominated regime and the Wigner regime at ultralow energies. We emphasize that, given the very different behavior in these two regimes, the high energy (barrier-dominated) results cannot simply be extrapolated towards vanishing kinetic energy. Moreover, as Fig. 4.1 shows, there is a significant barrier controlled regime even for high initial vibrational states ($v = 1$, 2, 3, 4). This is rather unexpected, if we simply compared the vibrational energies (up to about 2 eV) with the barrier height of approximately 0.5 eV. However, the persistence of the barrier regime for high vibrational states can be understood in terms of vibrational adiabatic curves, which have a repulsive wall at short range. This repulsive wall diminishes slowly for high v, and only disappears for $v \geq 5$. In other words, we can say that, effectively, there is indeed a barrier for $v \leq 4$; however, the effective height of the barrier, as manifested for a certain v, cannot be assessed by simply inspecting the potential surface. The extent of the barrier-dominated regime for high v can only be found by performing the full quantum computation. We see in Fig. 4.1 that the reaction probabilities reach values near unity at very high energy (above the barrier regime). As the kinetic energy is lowered towards the sub-Kelvin domain, the effective barrier for a certain initial v will dictate the decrease of the reaction probability. Thus, the s-wave results at high kinetic energy shed light on those in the ultracold regime; this is the reason we explored a range of kinetic energy that extends high above the sub-Kelvin domain.

For $v \geq 5$, the behavior in Fig. 4.1 is similar to that of systems without a reaction barrier [35], i.e, the reaction probability reaches values near unity at kinetic energies just above the sub-Kelvin regime. The only surprising aspect is that the transition

from barrier-dominated to barrierless dynamics occurs at reactant vibrational energies of about 2.5 eV, while the height of the barrier is only about 0.5 eV. As we explained above, this is due to the persistence of the repulsive wall of the vibrational adiabats.

Next, in Fig. 4.2, we show the kinetic energy dependence of the cross sections for quenching and reaction, for the same initial vibrational states of H_2 shown in Fig. 4.1. Given the simple expression of the cross sections in terms of probabilities, $\sigma \sim |S|^2/E_{kin}$, we again see a simple power law behavior at ultralow energies. Written in terms of cross sections, Wigner's threshold law reads

$$\sigma \sim \frac{1}{\sqrt{E_{kin}}}$$

Although Figs. 4.1 and 4.2 illustrate the threshold behavior equally well, the latter is much more striking, as it shows the inelastic cross sections increasing indefinitely when $E_{kin} \to 0$. However, as we saw in Fig. 4.1, all elements of the S-matrix corresponding to inelastic processes do vanish at the threshold, and this fact can have important consequences in the practical aspects of computation; indeed, the smallness of these quantities can pose numerical difficulties for systems with a high reaction barrier. This technical issue is particularly pressing for initial state $v = 0$.

For $v \leq 4$, the behavior of the inelastic cross sections in Fig. 4.2 shows again the two different regimes we saw in Fig. 4.1; now, the Wigner regime and the barrier dominated regime can be distinguished more clearly, as a pronounced minimum marks the transition region between the two regimes. The cross sections reach their minima at energies comparable to the depths ($E_{vdW} \approx 30$ K) of the van der Waals potential wells; however, one should not attach too much significance to this feature. In fact, it is the barrier regime that causes the minimum in the cross section to appear. Indeed, as we see in Fig. 4.2, for $v \geq 5$, the barrier regime disappears, and so does the minimum; for the highest vibrational states, the inelastic and reactive cross sections no
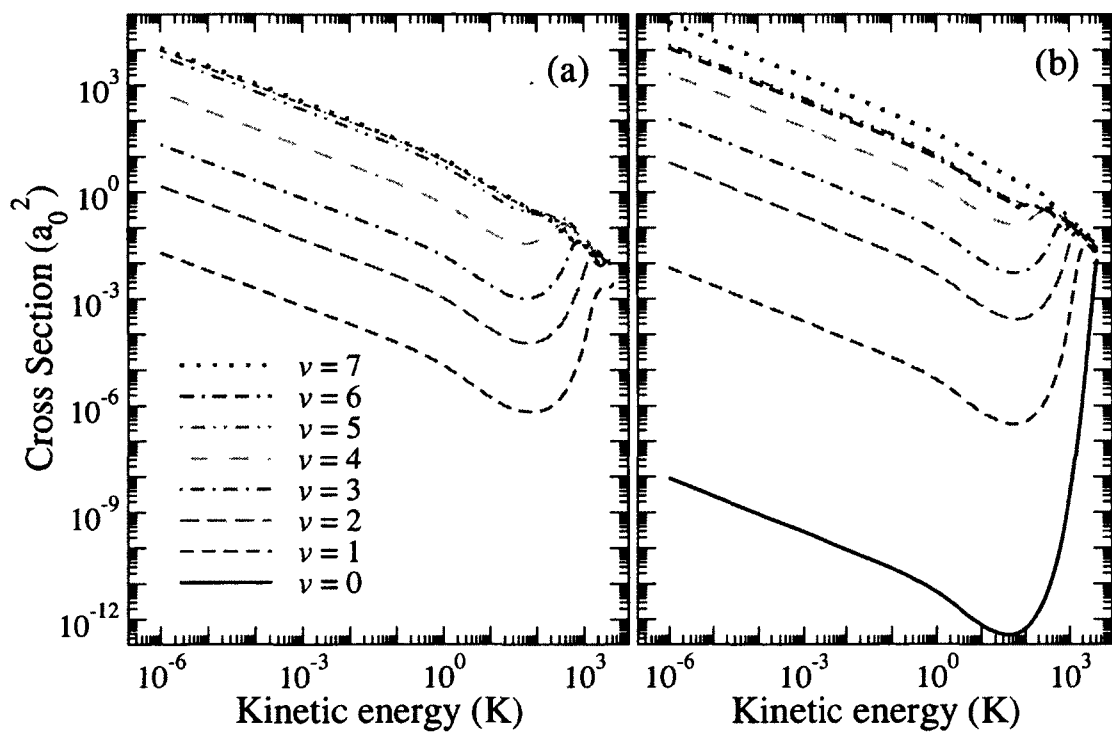
Figure 4.2 — Same as Fig. 4.1, for inelastic and reactive cross sections (unit is Bohr radius squared)

longer show any interesting features in the transition region (at intermediate energies, $E_{\text{kin}} \approx E_{\text{vdW}}$).

For completeness, we also show the behavior of the elastic cross section in Fig. 4.3, where we see that, in stark contrast to the inelastic and reactive cross sections in Fig. 4.2, the elastic cross section is rather insensitive to the initial vibrational excitation of the target. Despite the differences between the behavior of the elastic cross section and the inelastic and reactive cross sections, they have in common the intrinsic simplicity of the Wigner regime. Indeed, as we see in Fig. 4.3, the elastic cross section reaches a constant finite value at ultralow energies,

$$\sigma_{\text{el}} \approx 4\pi |a|^2 = 4\pi (\alpha^2 + \beta^2)$$

where $a = \alpha - i\beta$ is the s-wave scattering length (which is complex valued, see below).

For a given initial channel (v, j) in the entrance arrangement (labeled "a"), the scattering length is extracted from the low-k expansion of the diagonal element of the S-matrix (corresponding to the s-wave component of the initial channel); to the lowest order in k, we have:

$$S_{\text{a}vj,\text{a}vj} \approx 1 - 2\,i\,a_{\text{a}vj}\,k = 1 - 2\,\beta_{\text{a}vj}\,k - 2\,i\,\alpha_{\text{a}vj}\,k \tag{4.1}$$

For simplicity, we have omitted the quantum number $\ell = 0$ for the orbital angular momentum of the relative motion, and the total angular momentum $J = j$. The momentum k should also carry the quantum numbers of the initial channel and the label "a" for the entrance arrangement, but they were omitted to simplify notation; for clarity, we specify that k is the initial momentum in the entrance channel: $k^2/2\mu_{\text{a}} = E_{\text{kin}}^{\text{a}vj}$ with μ_{a} the reduced mass for the collision fragments D and H_2 in the entrance arrangement. Note that, when the scattering problem contains non-elastic (inelastic
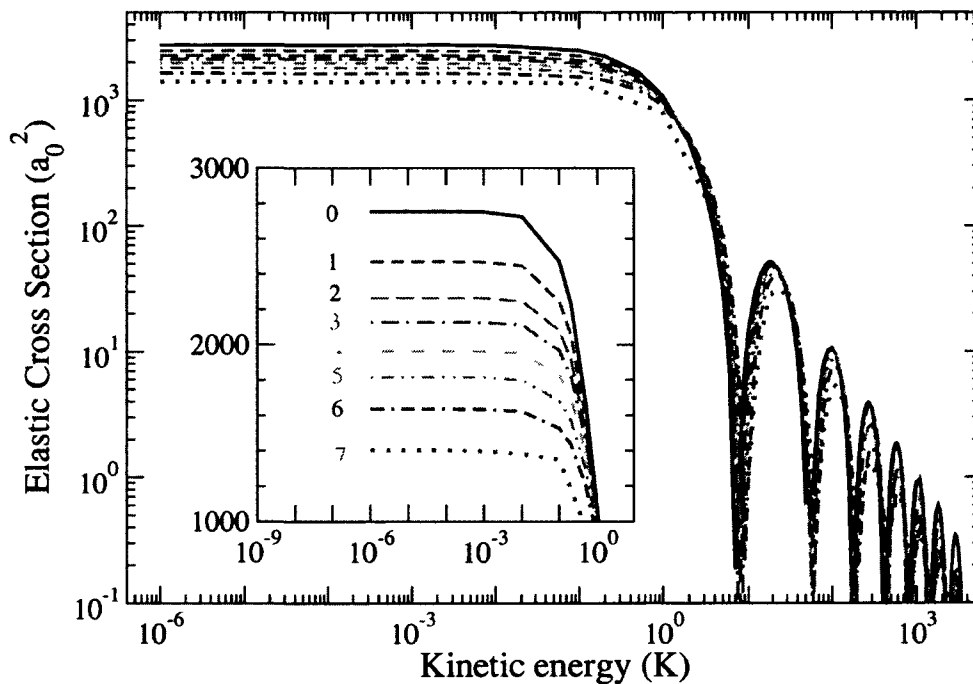
Figure 4.3 — Kinetic energy dependence of the elastic cross sections for D + $H_2(v, j = 0)$. All initial vibrational states ($v \leq 7$) of H_2 give results that are nearly identical, which is in contrast to the inelastic cross sections shown in Fig. 4.2. The oscillations at high energy are a reminder that this is an s-wave only result; the addition of higher partial wave contributions will have the effect of averaging out most of the oscillatory behavior.

or reactive) open channels, the scattering length acquires an imaginary part $(\beta = -\text{Im}(a) > 0)$.

In the Wigner regime, the total inelastic cross section can be expressed in terms of the scattering length. Integrating over angles and summing over all final channels in all arrangements, we obtain the total non-elastic cross section,

$$\sigma_{\text{tot}}^{\text{ne}}(k) = \frac{\pi}{k^2} \sum_J \left(\frac{2J+1}{2j+1} \right) \sum_\ell \widetilde{\sum_{a'v'j'}} \sum_{\ell'} |S_{a'v'j',\,avj}(k)|^2 \,,$$

where the symbol $\widetilde{\sum}$ signifies the entrance channel is excluded. In general, making use of unitarity will not help a great deal in simplifying this expression, as two sums still remain:

$$\sigma_{\text{tot}}^{\text{ne}}(k) = \frac{\pi}{k^2} \sum_J \left(\frac{2J+1}{2j+1} \right) \sum_\ell \left[1 - |S_{avj\ell,\,avj\ell}^J(k)|^2 \right]$$

It is only at ultralow kinetic energy that the significant contribution in the equation above is contained in a single term; namely, the one with $J = j$ and $\ell = 0$. At low-k, all other terms in the two remaining sums become negligible, as they are of higher order in k, and we have

$$\sigma_{\text{tot}}^{\text{ne}}(k) \approx \frac{\pi}{k^2} \left[1 - \left| S_{avj0,\,avj0}^{J=j}(k) \right|^2 \right] .$$

Making use of Eq. (4.1) for the s-wave diagonal matrix element, and retaining consistently terms of the lowest order in k, we obtain

$$\sigma_{avj}^{\text{ne}} \approx 4\pi \frac{\beta_{avj}}{k}$$

We point out that the simplicity of this expression is illusory; indeed, the scattering length $a = \alpha - i\beta$ can only be obtained as a result of a full coupled channel computation for the scattering problem.

So far, we have discussed the total non-elastic cross section, summed over all final states. Now, in order to gain more insight into our collision problem, we present the state-to-state cross sections in the ultracold limit, i.e., the detailed distribution over the final rovibrational states in both arrangements. The results shown in Figs. 4.4 and 4.5 are for initial channel $H_2(v = 7, j = 0)$, at $E_{kin} = 10^{-6}$ K, i.e., deep in the Wigner regime, where the branching ratios for the final states become constants. Regarding the overall branching ratio between the two product arrangements (reaction and quenching), see Fig. 4.2; also see Sec. 4.2, where we answer this question for all initial vibrational states.

As we see clearly in Figs. 4.4 and 4.5, the final states with the highest populations are those which have internal rovibrational eigenenergies nearly equal to that of the initial state of H_2. This approximate conservation of vibrational quantum number stems from the strength of the couplings between the initial and final channels. Indeed, at short range, the off-diagonal vibrational adiabats corresponding to (v, v') coupling are largest when v' is highest, and they get smaller as v' decreases. Note that the final states with high j' are typically suppressed, especially if they have very high internal energy. The suppression caused by the combination of high j' and high $\varepsilon_{v'j'}$ is easily understood as being due to a centrifugal barrier effect. Such a final channel, with its energy threshold just under the total collision energy, will have a very low kinetic energy (similar to the initial channel); given that in our cases we always have $J = 0$, each final channel has $\ell' = j'$ and thus can have a significant centrifugal barrier (if j' is large).
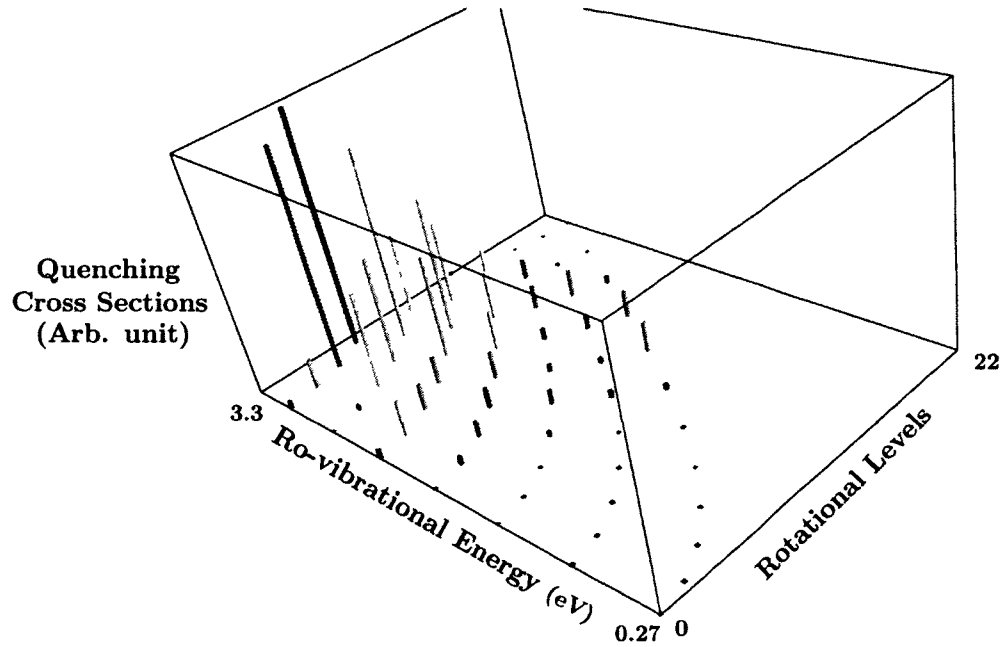
Figure 4.4 — Distribution over the final states of H_2 (inelastic) arrangement for initial state $v = 7$. The quantum number j' and eigenenergy $\varepsilon_{v'j'}$ of the rovibrational eigenstates of H_2 are shown on two of the axes; the cross section is shown on the vertical axis (the unit is arbitray, as we focus on the different values relative to each other). The maximum value on the energy axis is the collision energy itself, which is practically equal to the initial channel threshold eigenenergy.
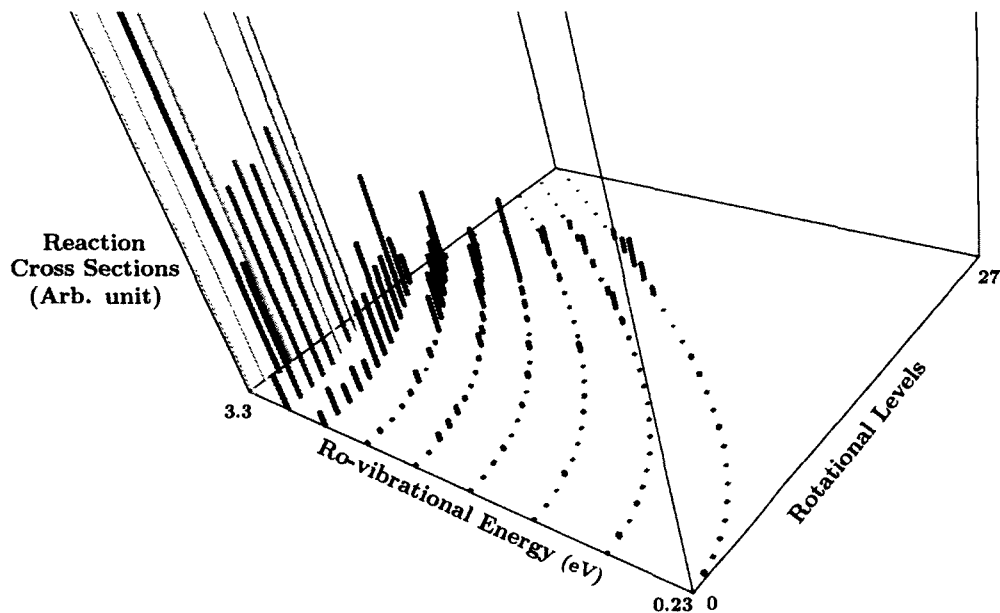
Figure 4.5 — Same as Fig. 4.4, for the final states of DH (reactive) arrangement. We truncated the top of this graph, in order to better discern the distribution for the final states with small cross sections.

4.2 Rate coefficients

Given the simple behavior of the inelastic cross sections in the Wigner regime, one obtains very simple results for the rate coefficients at ultralow temperatures. According to its definition, a rate coefficient is expressed as the average of the corresponding cross section multiplied with the relative velocity of the collision fragments: $\mathcal{K} = \langle v_{\rm rel}\sigma \rangle$. Assuming equilibrium, the velocity distribution is Maxwellian, and the thermal average can be written as

$$\mathcal{K}(T) = \left(\frac{8}{\pi \mu_a k_B^3 T^3} \right)^{1/2} \int_0^\infty dE\, \sigma(E)\, E\, e^{-E/k_B T}$$

If the temperature is low enough ($T \lesssim 0.1$ K, for the system we consider), then the distribution of velocities (kinetic energies) is confined within the Wigner regime, and the product $v_{\rm rel}\sigma$ becomes independent of $v_{\rm rel}$. Thus, the velocity distribution function becomes irrelevant, and the total non-elastic rate coefficient reads
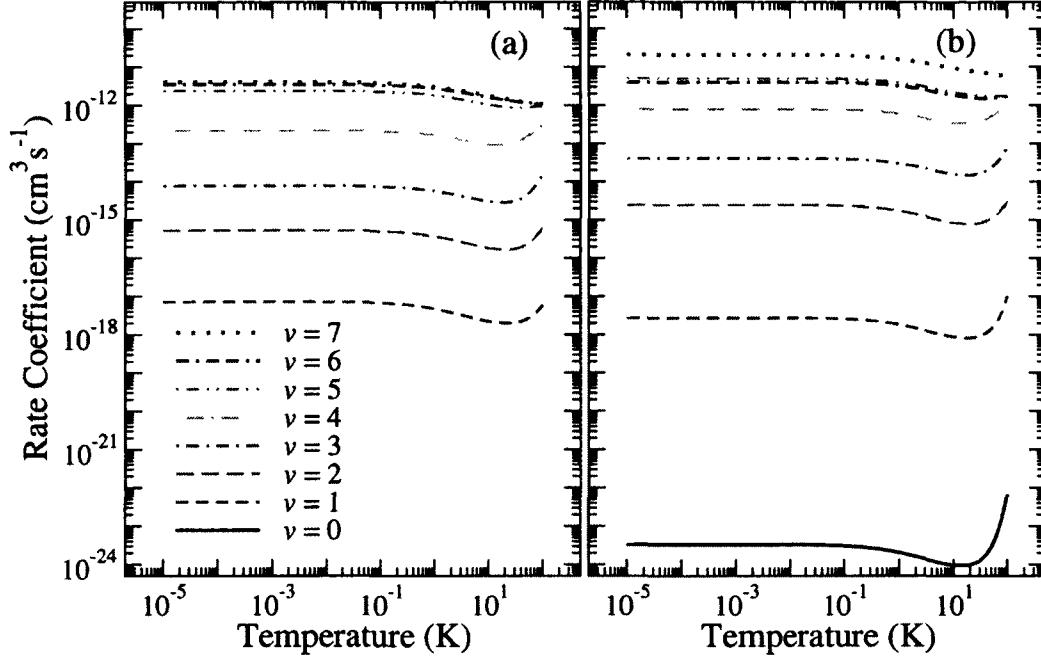
Figure 4.6 — Temperature dependence of rate coefficients, obtained by averaging the cross sections in Fig. 4.2 with a Maxwellian distribution function.

$$\mathcal{K}(T) \approx \frac{4\pi\hbar}{\mu_a}\beta_{avj} \qquad (\text{when } T \to 0).$$

As seen in Fig. 4.6, we indeed obtained $\mathcal{K}(T) \approx$ constant in the Wigner regime.

In Fig. 4.6 we show the temperature dependence of the rate coefficients for different initial vibrational states; the log scale makes it readily apparent that the rates reach finite (non-zero) values at ultralow temperatures. This result is fully general for *exoergic* processes, as it follows directly from Wigner's law for the threshold behavior of inelastic cross sections.

Having established that the rate coefficients become temperature independent in the Wigner regime, we now extract their values in the zero temperature limit for each of the initial H_2 states, and present them in Fig. 4.7. For $v = 0$, the reaction rate coefficient is extremely small, due to the reaction barrier; as discussed in Sec. 4.1, the effective barrier diminishes gradually for $1 \le v \le 4$, and it disappears for $v \ge 5$.

The quenching rate becomes nearly flat for $5 \leq v \leq 7$, while the reaction rate shows a drop for $v = 6$, and increases again (albeit more slowly) for $v = 7$. Although a gentle increase seems to continue for $v = 8$, we do not have fully converged results to confirm this trend at higher v. In fact, we have strong reasons to believe that the rates approach an upper limit for $v = 7$ and higher. Indeed, for $v = 7$, as seen in Fig. 4.1, the total probability for non-elastic processes approaches the unitarity limit, at the high energy end of the ultracold regime [9]. This is to be expected, as the reaction is governed by barrierless dynamics for very high v [35]. We thus infer that, for $v \geq 5$, the total rate coefficient is roughly independent of the initial vibrational state v. For the highest possible initial states (near the dissociation threshold) it may even be likely that the rates begin to decrease, due to the diatomic molecule being very loosely bound and its wavefunction becoming very thinly spread, with highest probability amplitude at large $H-H$ separations; however, this is unlikely for our system, as the $H_2(v)$ molecule is quite compact (it has rather small interatomic separation) even for the highest values of v.

Regarding the decrease of the reaction rate for $v = 6$, we found it to be caused by an accidental absence of dominant final channels in the product arrangement. In order to understand this, let us compare $v = 6$ and $v = 5$, for which the highest v' in the HD arrangement is $v' = v = 5$; due to the heavier mass, the $HD(v' = 5)$ level is significantly lower in energy than the initial state $H_2(v = 5)$, and there are several rotational states ($0 \leq j' \leq 7$, for $v' = 5$) that correspond to open channels; these are the dominant ones. For $v = 6$, there is an *accidental* occurrence; namely, $v' = 7$ of HD becomes open (just barely, i.e., only $j' = 0$ is open). We show a group of energy levels in Fig. 4.8, where we see that due to the heavier mass, the higher vibrational levels of HD have a tendency to catch up with the lower levels of H_2. Although the highest final state ($v' = 7$) in HD should be dominant, there is now only a single
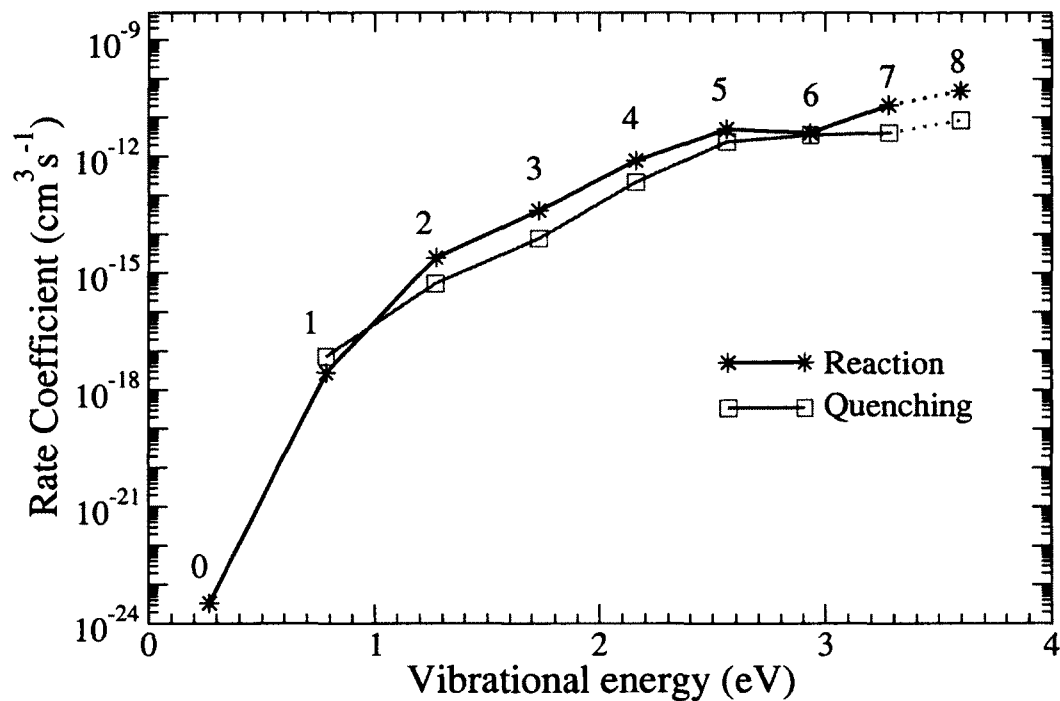
Figure 4.7 — Dependence of rate coefficients upon the initial vibrational state v of the H_2 target (each value of v is shown inside the figure, while the initial internal vibrational energy ε_v is the abscissa). The dotted lines for $v = 8$ are used to indicate that our results are not fully converged for $v \geq 8$.
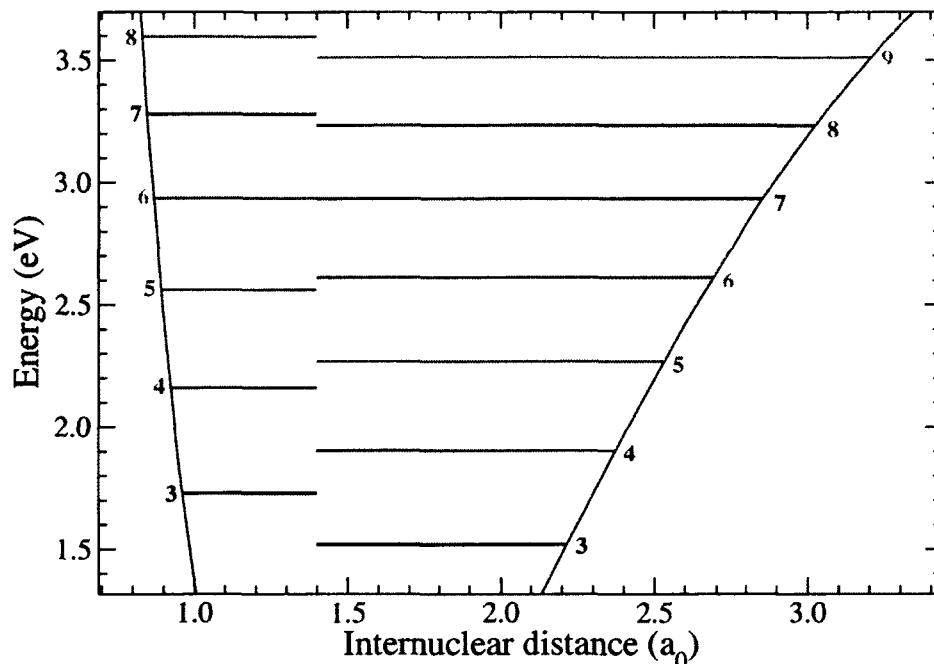
Figure 4.8 — Vibrational energy levels of H_2 (left side) and HD (right side) shown inside a section of the diatomic potential energy curve. Note that the $v = 6$ level of H_2 has almost the same energy as $v = 7$ of HD; this accidental near-degeneracy has a strong effect on the reaction rate (see Fig. 4.7). For HD, we also show some of the rotational levels in a lighter shade of gray.

channel ($j' = 0$) contributing for $v' = 7$, and thus the j' sublevels in $v' = 6$ contribute significantly. However, the $v' = 6$ channels have weaker couplings with the initial channel (see the discussion about vibrational adiabats at the end of Sec. 4.1), which explains the anomalous decrease of the reaction rate for $v = 6$ in Fig. 4.7.

We summarize our results in Table 4.1, where we give the threshold limit values for the elastic cross sections, rate coefficients, and the complex scattering lengths for all initial vibrational states $v \leq 7$. Except for $v = 0$, the rate coefficients are sizable, and they increase rather quickly with v. Until now, similar computations for ultracold collisions with highly excited targets have only been done for non-reactive systems, e.g., quenching of excited H_2 by noble gas atoms [36, 37]; for these non-reactive systems, the zero temperature rate coefficients are comparable with the ones

66

Table 4.1 — Elastic cross sections σ_{el}, rate coefficients K_{quench} and K_{react}, and the real and imaginary parts of the scattering lengths, α and β, for initial channels $v \leq 7$.

v	σ_{el} (a_0^2)	K_{quench} $(\mathrm{cm^3\,s^{-1}})$	K_{react} $(\mathrm{cm^3\,s^{-1}})$	α (a_0)	β (a_0)
0	2755	—	3.3×10^{-24}	14.81	7.9×10^{-14}
1	2470	7.2×10^{-18}	2.7×10^{-18}	14.02	2.35×10^{-7}
2	2265	5.4×10^{-16}	2.5×10^{-15}	13.43	7.16×10^{-5}
3	2128	7.8×10^{-15}	4.1×10^{-14}	12.41	1.16×10^{-3}
4	1965	2.2×10^{-13}	7.8×10^{-13}	11.91	2.40×10^{-2}
5	1818	2.4×10^{-12}	5.1×10^{-12}	11.08	1.81×10^{-1}
6	1637	3.5×10^{-12}	4.0×10^{-12}	10.56	1.89×10^{-1}
7	1405	4.1×10^{-12}	2.1×10^{-11}	8.99	6.02×10^{-1}

we obtained for $D + H_2$ for low initial vibrational state ($v = 1, 2, 3$). However, for $v = 4$ and 5, the rate coefficients for our reactive system continue to increase faster than those for noble gases. For higher initial states, we encounter a different regime for $v \gtrsim 5$, where the rate coefficient is nearly flat (approaching its upper limit) and it may possibly begin to decrease; see Fig. 4.7. Unfortunately, due to technical difficulties, we could not obtain fully converged results for $v > 8$; thus, the v-dependence of the reaction rates for a vibrationally excited target near its dissociation threshold remains an open question.

Chapter 5

Excursion outside ultracold. D–H_2 collisions at subthermal energies

In this chapter we study the reaction rate constant for D + $H_2(v = 0)$ at thermal and subthermal temperatures, i.e., high above the ultracold regime. Thus, we go beyond s-wave and we compute results for higher partial waves, which are necessary for obtaining full convergence at high energies. The reaction D + $H_2 \longrightarrow$ DH + H is very important in astrophysics; accurate values for its rate coefficient are needed over a wide range of temperatures (including at low T, just above the sub-Kelvin regime). The production of DH via this reaction may contribute significantly to its overall abundance. The general question of finding the abundances of the various chemical species in the Universe, over its entire history since the recombination era, is still an open question in astrophysics. In particular, a good knowledge of the abundance of DH is required, as it can play an important role in the initial stages of star formation via the gravitational collapse of a gas cloud. However, laboratory measurements of the reaction rate constant for D + H_2 have only been done for temperatures in the range $167 < T < 2200$ K [1]. Despite the importance of this reaction, experimental data are not yet available for $0 < T < 167$ K. Here, we provide computed results to fill this gap.

Before we discuss our new results, we mention that Schatz [38] computed the reaction rate coefficient for D+$H_2 \longrightarrow$ DH+H at low temperatures (including the Wigner

regime). Although qualitatively correct, this result has generally been overlooked, especially in the astrophysics community, where various empirical approximations are often employed outside their domain of validity. This unfortunate practice of using invalid extrapolations becomes inevitable when both experimental data and computed results are absent. Clearly, the only good remedy is obtaining accurate results, both experimentally and theoretically.

5.1 Failure of the Arrhenius approximation

We mentioned in the previous chapter that the temperature dependence of the reaction rate coefficients in the barrier dominated regime cannot be extrapolated into the sub-Kelvin regime. Consequently, we performed full quantum computations in order to find the correct temperature dependence of the reaction rate coefficient over a wide temperature domain. We emphasize that, although reaction rate coefficients for systems with a barrier can be very small in the sub-Kelvin regime, their temperature dependence is more than an academic curiosity. Indeed, we shall see that the conventional Arrhenius rate begins to diverge significantly from the correct result at temperatures that are orders of magnitude above the ultracold regime.

The Arrhenius plot (with $1/T$ on the abscissa) in Fig. 5.1 shows results for $D + H_2 \longrightarrow DH + H$, which prove the breakdown of the conventional Arrhenius rate at temperatures below 200 K. We stress that, along with the conventional Arrhenius approximation, $\mathcal{K}_{\text{Arrh}}(T) = A\exp(-B/T)$, the generalized version, $\mathcal{K}_{\text{Arrh}}(n; T) = A T^n \exp(-B/T)$, also fails at low T; note that, even if one allows for negative powers ($n < 0$), the exponential factor still dictates a rapid vanishing at low temperatures. This contradicts the correct behavior in the sub-Kelvin regime for exoergic reactions; indeed, according to Wigner's law, the rate coefficient for an exoergic collision reaches a nonzero constant value when $T \to 0$, which is confirmed by our computed results.
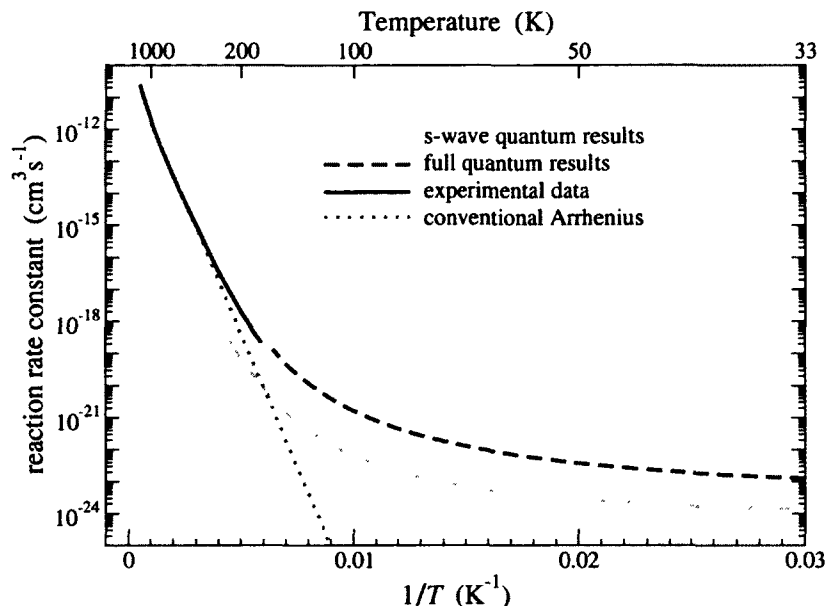
Figure 5.1 — Comparison of reaction rate coefficients: long-dash curve for s-wave computation, short-dash curve for full computation, full curve for the polynomial fit of experimental measurements [1], and dotted line for the conventional Arrhenius approximation $\mathcal{K}_{Arrh}(T) = A \exp(-B/T)$, with empirical parameters $A = 7.5 \ 10^{-11} \ \text{cm}^3/\text{s}$ and $B = 3820$ K extracted by fitting [2] quantum mechanically computed results [3]. Note the temperature scale at the top.

Fig. 5.1 also shows that, for systems with a reaction barrier, the temperature dependence of the s-wave result alone is sufficient to predict failure of the Arrhenius approximation.

In Fig. 5.1 we included experimental data, which only exist for $T > 167$ K, but already give a glimpse of the true curvature of the Arrhenius plot. We emphasize that, although one can account very accurately for the curvature with a simple empirical fit, such fitting formulas should not be extrapolated outside the temperature domain of the original data. For temperatures $T \lesssim 50$ K, we see in Fig. 5.1 that the reaction rate coefficient seems to level off; however, this is an artifact of the Arrhenius plot, with T^{-1} on the abscissa, which stretches too much the low temperature part. While it is true that $\mathcal{K}(T)$ will become constant in the $T \to 0$ limit, this will

only happen inside the Wigner regime (restricted to $T \ll 1$ K, as seen in the previous chapter). Hence, just as the extrapolation of the Arrhenius rate towards low temperatures is incorrect, the converse extrapolation of the Wigner regime behavior towards higher temperatures is also wrong. Thus, bridging the gap between the much simpler Wigner and Arrhenius regimes requires accurate data, either coming from experimental measurements, or from computed results.

5.2 Reaction rate coefficients for $T < 500$ K

Assuming thermal equilibrium, we compute the rate coefficient by thermally averaging the energy dependent cross sections for all initial rotational states $(v = 0, j)$ of H_2, and we add their contributions weighted with their fractional populations. We thus have

$$\mathcal{K}(T) = \sum_j p_j(T)\, \mathcal{K}_j(T),$$

with the populations $p_j = \frac{g_j}{Z_{rot}(T)} e^{-\frac{\epsilon_j}{k_B T}}$ normalized to unity, $\sum_j p_j = 1$, and $Z_{rot}(T) = \sum_j g_j e^{-\frac{\epsilon_j}{k_B T}}$. The degeneracy factors are

$$g_j = 2j + 1, \qquad \text{for } j = 0, 2, 4, \dots \text{ (para hydrogen)}$$

$$g_j = 3(2j + 1), \qquad \text{for } j = 1, 3, 5, \dots \text{ (ortho hydrogen)},$$

and the state specific rate coefficients are

$$\mathcal{K}_j(T) = \int_0^\infty \sigma_j(E_{kin}) E_{kin} e^{-E_{kin}/k_B T} dE_{kin}. \tag{5.1}$$

In Fig. 5.2 we show the temperature dependence of the ratios $r_j(T) = p_j \mathcal{K}_j / \mathcal{K}$, i.e., the relative contributions of the rotational levels in $v = 0$ for $T < 500$ K. Note

71
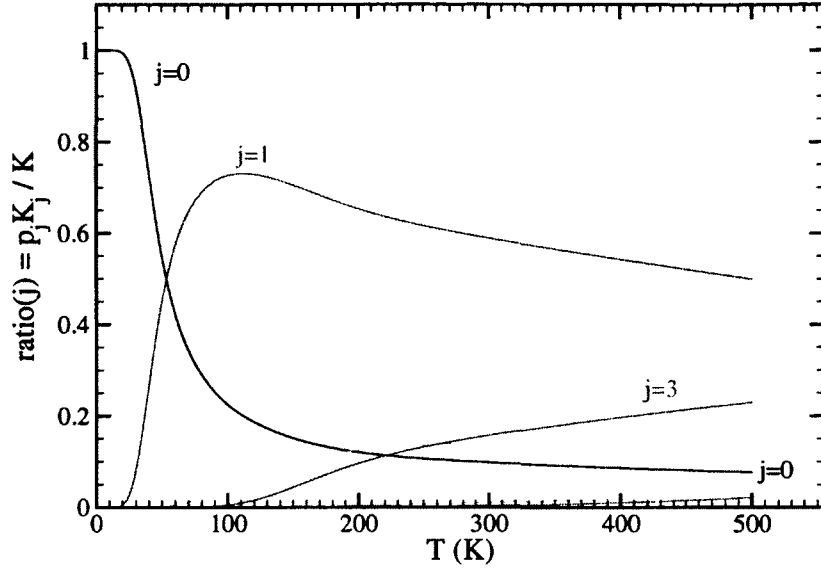
Figure 5.2 — Fractional contribution of rate coefficients for individual rotational levels j (which are shown next to each curve, except for $j = 4, 5, 6$ at the bottom).

that the contribution of $v = 1$ is negligible at these temperatures. For $v = 0$, we see in Fig. 5.2 that the first few excited rotational levels ($j = 1$, 2, 3) begin to contribute significantly at remarkably low temperatures; indeed, judging by the Boltzmann factor alone ($e^{-\frac{\varepsilon_j}{k_B T}}$), one would naively expect that $j = 1$ would become significant only for $T \gtrsim 200$ K (i.e., when $k_B T$ becomes comparable to $\varepsilon_1 - \varepsilon_0 \approx 170$ K). However, the $j = 1$ term begins to rise quickly at $T \approx 20$ K, and it overtakes the $j = 0$ term at $T \approx 60$ K. The $j = 2$ and $j = 3$ terms become significant at $T \approx 100$ K, despite the fact that ε_2 and ε_3 are several hundred Kelvin above ε_0. There are two simple facts that account for these surprising results: for $j = 1$, the degeneracy factor alone brings an enhancement of almost one order of magnitude, as we have $g_1 = 9$ and $g_0 = 1$; also, the state specific reaction cross sections (hence the individual rate constants $\mathcal{K}_j$) increase quickly with j, and this enhancement makes up for the smallness of the Boltzmann factors at low T.
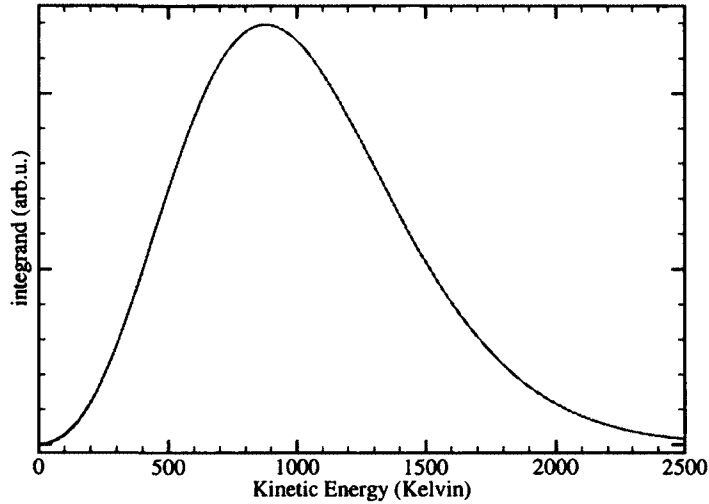
Figure 5.3 — Energy dependence of the integrand $E\sigma_j(E)e^{-\frac{E}{k_BT}}$ in Eq. (5.1) for initial state $(v = 0, \; j = 0)$ of H_2, and temperature $T = 100$ K.

Regarding the state specific rate constants $\mathcal{K}_j$ in Eq. (5.1), we emphasize that the subthermal regime is rather peculiar due to the very fast increase of the reaction cross section $\sigma_j(E_{kin})$ in the barrier dominated regime. Thus, for a given temperature, the integrand's main contribution to the thermal average in Eq. (5.1) comes from energies high above k_BT; in other words, the high energy ($E_{\text{kin}} \gg k_BT$) tail of the Maxwellian velocity distribution carries the dominant contribution. This is illustrated in Fig. 5.3, where we see that for $T = 100$ K, the integrand reaches its maximum around $E_{\text{kin}} \approx 800$ K, and it contributes significantly up to $E_{\text{kin}} \approx 2500$ K. Thus, the shape of the velocity distribution function (Maxwellian or not) is very important, as the rate constant can be very sensitive to the high energy tail. Consequently, for any given situation in a laboratory experiment or in planetary atmospheres and interstellar clouds, the assumption of thermal equilibrium should only be employed if it is really true.

The importance of the high energy tail of the Maxwellian distribution also has significant consequences of a practical nature, as it makes the computations very

73

expensive. For example, for $T = 100$ K one needs to thermally average the energy dependent cross section up to $E_{kin} \approx 2500$ K. Moreover, high collision energies also require many partial waves, thus increasing the computational difficulty. For the results presented in this chapter, we computed results for collision energies up to $E \approx 1.2$ eV $\approx 14\,000$ K, and we included contributions for total angular momentum $J \leq J_{max} = 25$. The truncation energy was set to $E_{max} = 3$ eV, and the hyperradial coupled equations were propagated up to $\rho_{max} \approx 25$ a.u., with an integration step $\Delta\rho = 0.02$ a.u.
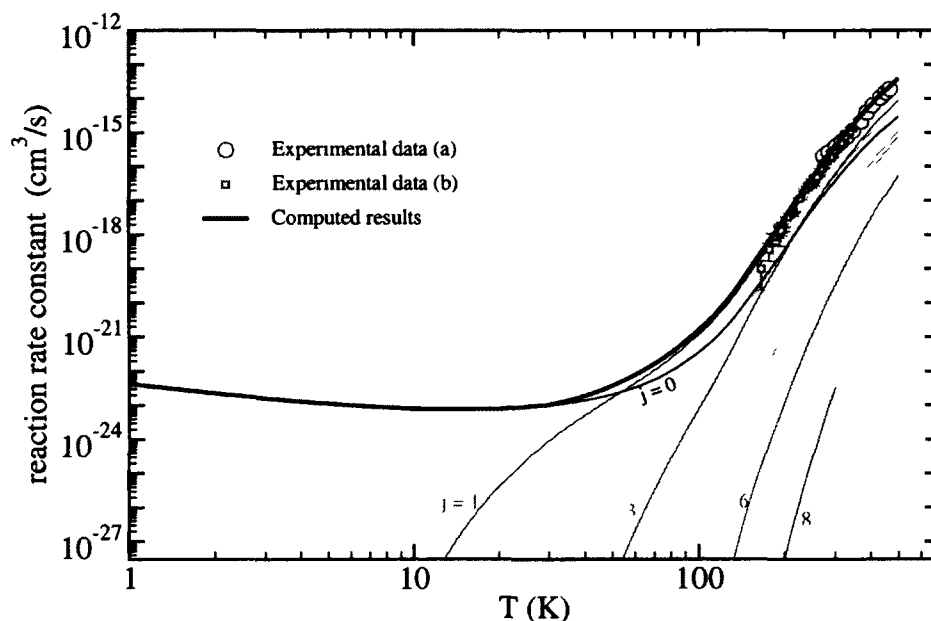
Figure 5.4 — Temperature dependence of the reaction rate coefficient for $H_2(v = 0) + D \longrightarrow HD + H$. Experimental data (a) are from Ref. [4], and (b) from Ref. [5]. The thick full line is for our full computation; the contributions of individual rotational levels j (in $v = 0$) are shown with thin lines.

In Fig. 5.4 we summarize the results already shown in Figs. 5.1 and 5.2. We now use a logarithmic temperature scale, which is more suitable for low and moderate T, and we cover the range $1 < T < 500$ K. The experimental results are included in Fig. 5.4 only to show that our computed results are in good agreement with them.

74

However, we focus here on the low T regime, where experimental measurements are absent. Our results indicate that the rate constant reaches a minimum value, $\mathcal{K}_{min} = 7\ 10^{-24}$ cm^3/s, at $T \approx 20$ K, and it starts to increase towards lower T. We analyze this surprising behavior in the next section.

5.3   Returning to the ultracold regime

In Chap. 4 we presented s-wave only results, which typically show a slight increase towards low T, just before entering the Wigner regime. However, the full results (including higher partial waves) in Fig. 5.4 show a more pronounced increase increase towards low T. We will now see that this anomalous increase of the rate constant is due to a shape resonance in the p-wave contribution.

5.3.1   Shape resonances in reactive scattering

After presenting the high T results, we end this chapter by returning to the ultra-cold regime. In Fig. 5.5 we now show the behavior of the reaction rate coefficient over a temperature range which includes the ultracold regime. There is a surprisingly large
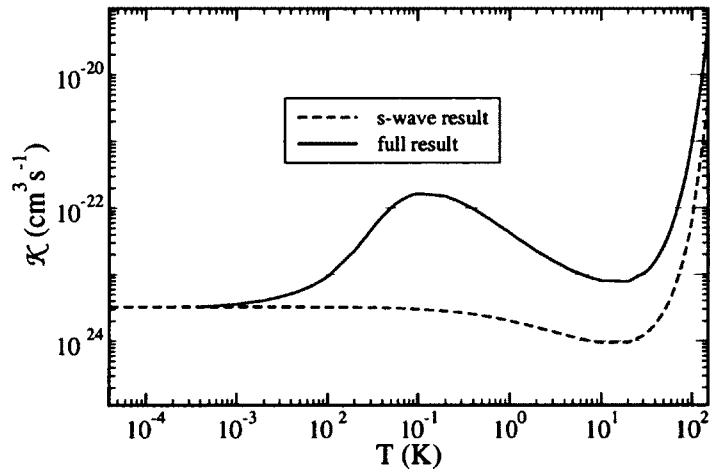
Figure 5.5 — Same as Fig. 5.4. The pronounced maximum at $T \approx 0.1$ K is due to a shape resonance in p-wave, which was obviously missing from the s-wave results.

difference between the full result and the s-wave term, which persists even at very low T. This is due to a shape resonance in p-wave, which affects strongly the results for $T \gtrsim 1$ mK. Thus, the dominance of the s-wave term (with its simple Wigner regime behavior) is now restricted to $T < 1$ mK. Note that in the absence of shape resonance in $\ell \geq 1$ partial waves, the s-wave term is typically dominant for $T < 100$ mK.

In order to clarify the interpretation of the resonance in Fig. 5.5, we show the energy dependence of the reaction cross section in Fig. 5.6 (which also shows the individual contributions for $J = 0$, 1, 2). Given the simplicity of our case, namely the initial state of H_2 has $j = 0$, we have for the relative orbital angular momentum in the entrance channel: $\ell = J$. Thus, we can indeed identify easily the resonant feature as a p-wave shape resonance. We will see in the next chapter that low energy resonances can also appear in s-wave, and the threshold behavior will be affected dramatically.
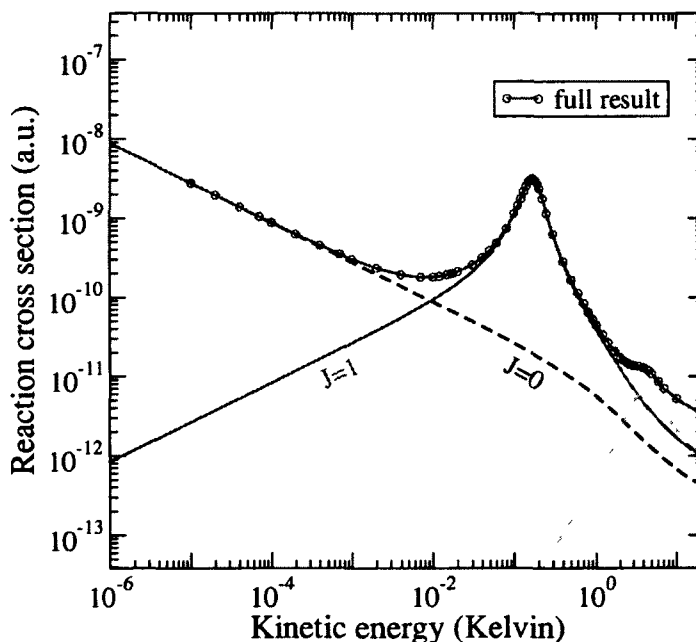
Figure 5.6 — Energy dependence of the reaction cross section. The individual contributions for partial waves s, p, and d are labeled, while the full result includes all partial wave terms up to $J = 25$.

Chapter 6

Isotope effects and threshold resonances

In this chapter we analyze the effects of weakly bound van der Waals complexes on the reaction rate coefficient at ultralow temperature for $Cl + H_2 \longrightarrow HCl + H$. This question, as we shall see, can be addressed by performing a detailed study of isotopic effects. In general, the behavior in the ultracold regime can be affected by any van der Waals complex that is located energetically near the threshold of the entrance channel; such a complex can be present in the entrance channel itself, or in any closed channel (either in the product, or in the reactant arrangement). A quasibound complex in one of the closed channels will typically produce a Feshbach resonance; this has attracted a considerable amount of attention from the community working on ultracold phenomena in general. On the other hand, the situation of a threshold resonance produced by a quasibound complex in the entrance channel has received surprisingly little attention, despite the fact that it is a simpler problem to deal with. As our studies will reveal, for systems with a reaction barrier—and in general, for many-channel scattering problems that are highly elastic—threshold resonances in the entrance channel have dramatic effects on low energy scattering.

We have investigated in great detail near threshold resonances caused by a quasi-bound van der Waals complex $(Cl \cdots H_2)$ in the entrance channel, $H_2(v = 1, j = 0)$, and we present the results in this chapter. We shall see that, when a complex has a vanishingly small binding energy, then it can dramatically affect the scattering at low energy, provided the complex is very stable against both reaction and quenching.

77

In other words, when both the width and the binding energy of the van der Waals complex are smaller than the energy scale of the van der Waals tail of the potential, $E_{vdW} = C_n/(2\mu C_n)^{\frac{n}{n-2}}$, the quasibound complex will produce strong resonance effects in ultracold collisions. Such a resonance will modify significantly the low energy behavior of the cross sections (elastic, inelastic, and reactive); moreover, despite the complexities of a large many-channel problem, we will see that the new type of energy dependence can be easily understood in terms of threshold resonance effects for a single-channel (elastic) scattering problem.

6.1 Threshold resonances in s-wave elastic scattering

The textbook example of a resonance effect in scattering at low energies is that of a shape resonance. Namely, if the effective potential energy (including the centrifugal barrier for a given partial wave $\ell \geq 1$) holds a quasibound level embedded in the continuum just above the threshold, then the cross section will show a sharp feature precisely at energies near the position of such a level. However, a resonance enhancement effect can also occur for $\ell = 0$, as is well known from the simple case of single channel (elastic) scattering.

For simplicity, we consider here the case of potential scattering for a spherically symmetrical $V(R)$. It is well known that, when the potential has a bound or antibound (virtual) level near $E = 0$, the scattering length a is extremely large; hence, the elastic cross section becomes very large near the threshold. It is also known that, while the zero energy approximation ($\sigma \approx 4\pi a^2$) has a very limited domain of applicability (i.e., the Wigner regime, for $k \ll |a|^{-1}$), there exists a simple expression for the energy dependence of the cross section, which is valid for an energy range that is much wider than the Wigner regime. We will first give two different descriptions

for the single channel problem, which will help us analyze the results for the many channel reactive problem $H_2 + Cl$.

6.1.1 Pole description of a threshold resonance

The effects of a near threshold resonance in s-wave scattering at low energy can be most *conveniently* analyzed in terms of the poles of the S-matrix in the complex plane of the momentum variable k. However, there is an important caveat; namely, the extension of the analysis on the real axis to the complex plane is quite problematic for all realistic potentials in atomic physics, because of their inverse power behavior $(V \approx -\frac{C}{R^n})$ in the asymptotic region. Rather than pursuing mathematical rigor, we will try to justify this approach by showing that it yields the same results as a more pedestrian analysis which is restricted to the real axis, as we will see in the next section.

Assuming we are allowed to define the S-matrix $S(k)$ in the complex k-plane, we will factor out explicitly the contribution of a nearby pole at $k = p$ (and its associated zero at $k = -p$). Thus, we write

$$S(k) = \frac{p + k}{p - k} \, \tilde{S}(k), \tag{6.1}$$

with $p = p' + ip''$. Recall that we focus here on a small region near $k = 0$, as we are interested in the case when the pole–zero pair is in the vicinity of $k = 0$, and will greatly affect the scattering results at low energy. From Eq. (6.1) we can extract the s-wave phaseshift, $\delta = \frac{1}{2}\arg(S)$, as a sum of two terms: $\delta = \delta_{res} + \tilde{\delta}$. For the background contribution we assume the simplest low energy approximation, namely $\tilde{S}(k) \approx e^{-2i\tilde{a}k}$, which yields $\tilde{\delta}(k) = \frac{1}{2}\arg(\tilde{S}) \approx -\tilde{a}k$, with $\tilde{a}$ the background scattering length. The resonant contribution given by the pole–zero pair can also be written explicitly; for a purely elastic problem, the pole is on the imaginary axis, and we have

79

$\delta_{\rm res}(k) = -\arctan(\frac{k}{p''})$, with $p'' = {\rm Im}(p)$. For single-channel (elastic) scattering we have $p' = {\rm Re}(p) = 0$, but in general, when inelastic channels are open in addition to the elastic one, we have $p' \neq 0$, as we shall see later in this chapter.

The $k \to 0$ limit of the phaseshift yields the full scattering length, which can be written as a sum of background and resonance terms: $a = \tilde{a} + \frac{1}{p''}$. We are interested here in the special case when the resonant term is dominant ($|\tilde{a}| \ll |p|^{-1}$), such that we have $a \approx \frac{1}{p''}$. In fact, we will ignore the background contribution entirely, i.e., we set $\tilde{S} = 1$ in Eq. (6.1), which amounts to using the so-called pole approximation, $S \approx \frac{p+k}{p-k}$. The elastic cross section can now be written in terms of the phaseshift, or more directly as $\sigma = \frac{\pi}{k^2}|1 - S|^2$. Within the pole approximation, we obtain

$$\sigma \approx \frac{4\pi}{k^2 + (p'')^2} \tag{6.2}$$

As expected, the pole approximation yielded a result that is reminiscent of the Breit–Wigner formula. However, we emphasize that Eq. (6.2) contains subtle differences; although the cross section has a Lorentzian shape, it is expressed in terms of momentum k, not energy E, which is a consequence of the fact that the former (rather than the latter) is the appropriate variable near the threshold. Also, only half of the line shape is visible, so to say, as the other half (below the threshold) is not directly accessible in a scattering problem in which the threshold belongs to the entrance channel itself.

When the resonance enhancement is strong, the energy dependence of the cross section near the threshold looks somewhat peculiar on a log-log plot. For illustration purposes, we computed the s-wave elastic cross section for a modified Lennard–Jones potential which mimics the true potential for the singlet ground state of RbCs. In Fig. 6.1 we show the results for the resonant case, along with the "normal" case; the potential was kept the same, and only the mass of the Rb atom was changed, which

shows that isotope effects and threshold resonance phenomena are closely linked in low energy scattering. We see clearly in Fig. 6.1 that the Wigner regime (with the simple behavior $\sigma \approx 4\pi a^2 \approx 4\pi(p'')^{-2}$) is limited to much lower energies in the resonant case. Also, a new regime of low energies emerges, characterized by the behavior $\sigma(k) \approx 4\pi k^{-2}$. This new domain of energies, which we call *Bethe regime*, covers the portion of the low energy domain that remained outside the Wigner regime, as the latter was displaced towards $E = 0$. It follows from Eq. (6.2) that the transition between the Wigner and Bethe regimes takes place at energies $E \approx |E_p| \equiv \frac{(p'')^2}{2\mu}$. This is the smallest energy scale in the scattering problem, when the pole at $k = p$ is very close to $k = 0$. Thus, the pole dictates that the Wigner regime be restricted to $E \lesssim |E_p|$, while the Bethe regime will extend to the high end of the full regime of low energies, $|E_p| \lesssim E \lesssim E_{\text{vdW}}$, with $E_{\text{vdW}} = C_n/(2\mu C_n)^{\frac{n}{n-2}}$.
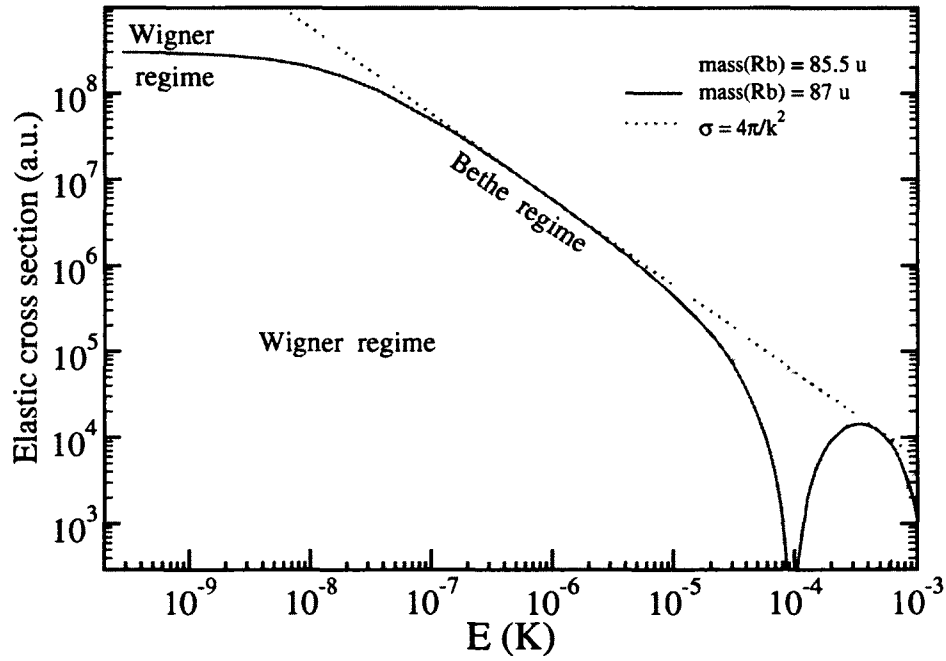

Figure 6.1 — Elastic cross section for the "normal" case (dashed line), and for the resonance case (full line). The dotted line shows the resonant behavior, which defines the Bethe regime in the resonance case.

We note that, although the background contribution could have been taken into account easily, we have neglected it here in order to clarify the role played by the resonant term. We emphasize that, despite the dramatic effect produced by a near threshold resonance, there is an inherent simplicity in the scattering problem at low energy which allowed us to write the simple result in Eq. (6.2).

6.1.2 Description on the real axis

In order to justify the pole description given above, and also to answer a separate question regarding the amplitude of the wavefunction at short range, we now present an alternative discussion which does not use complex energies or momenta. Namely, we will analyze the solutions of the radial equation, and we will extract quantities such as the phaseshift and the short range amplitude of the scattering solution $\psi_k(R)$. Although we are discussing formal aspects of the scattering problem, it helps to keep in mind the practical aspects of obtaining numerical solutions for the radial equation. Typically, the wavefunction is initialized at short range (inside the repulsive wall of the potential, near $R = 0$) and a certain algorithm is employed to compute it at subsequent points on a discrete mesh $\{R_n\}$. Thus, according to the formal aspects, we are actually computing the *regular* solution $\phi(R)$, not the *scattering* solution $\psi(R)$. Although these two solutions only differ by a (k-dependent) multiplicative coefficient, the distinction between them is very important, and it is the subject of the alternative description we give here. Note that, while the scattering solution is normalized by fixing its amplitude in the asymptotic region, e.g., $\psi(R) \sim \sin(kR + \delta)$, the regular solution has its amplitude fixed at short range (strictly speaking, at $R = 0$), where the initialization is done.

After computing the wavefunction, the final step is matching it with the asymptotic solutions, at a fixed point ($R = R_*$) chosen such that the influence of the poten-

tial tail (for $R > R_*$) is small. Denoting as $f_k(R)$ and $g_k(R)$ the *exact* solutions of the radial equation which satisfy the asymptotic boundary conditions $f_k(R) \sim \sin(kR)$ and $g_k(R) \sim \cos(kR)$, we write the matching conditions:

$$\phi_k(R_*) \;=\; \frac{1}{k} A(k)\, f_k(R_*) + B(k)\, g_k(R_*) \tag{6.3}$$

$$\phi'_k(R_*) \;=\; \frac{1}{k} A(k)\, f'_k(R_*) + B(k)\, g'_k(R_*)$$

This system of linear equations for A and B can be solved easily, provided we know the regular solution ϕ and also the two solutions f and g. Thus, we obtain

$$A(k) \;=\; W(g_k, \phi_k) \tag{6.4}$$

$$B(k) \;=\; -\frac{1}{k}\, W(f_k, \phi_k)$$

where $W(\ ,\ )$ denotes the Wronskian. Note that, if all three radial solutions (ϕ, f, g) are exact, the Wronskians (and hence the coefficients A and B) do not depend on R_*. In Eq. (6.3) the factor $\frac{1}{k}$ was included, such that both $A(k)$ and $B(k)$ will have expansion series at low-k which start with zeroth order terms.

All physical quantities relevant to the scattering problem can now be expressed in terms of $A(k)$ and $B(k)$. For example, the phaseshift will be given by $\tan \delta(k) = k\frac{B(k)}{A(k)}$, and in the $k \to 0$ limit we obtain the scattering length $a = -\frac{B(0)}{A(0)}$. Also, the scattering solution can be written in terms of the regular solution,

$$\psi_k = C(k)\, \phi_k$$

with the k-dependent coefficient $C(k)$ given as

$$C(k) = \frac{k}{\sqrt{A^2 + k^2 B^2}}$$

We are interested in the special case of a near threshold resonance, which occurs when $A(0)$ is very small, such that $\phi_0 \approx B(0)g_0$ (i.e., the regular solution becomes almost

linearly dependent on g_0). Recalling that the normalization of the regular solution is arbitrary, one can chose $B(0) = 1$. Hence, it follows that the scattering length, $a = -\frac{B(0)}{A(0)} = -\frac{1}{A(0)}$, is very large.

The "envelope" coefficient $C(k)$ has a very interesting behavior when a resonance is near the threshold; indeed, in the absence of a near threshold resonance, it behaves linearly at low-k, $C(k) \approx \frac{k}{|A(0)|}$. However, when $A(0)$ is vanishingly small, the term $k^2 B(k)^2 \approx k^2 B(0)^2$ will quickly become dominant when k increases slightly. Thus, the Wigner regime, characterized by the linear behavior of $C(k)$, is restricted to $k \ll |\frac{A(0)}{B(0)}|$. Next, while k is still very low, but $k \gg |\frac{A(0)}{B(0)}|$, the behavior will change to $C(k) \approx \frac{1}{|B(0)|} = $ constant, as we see in Fig. 6.2; this anomalous behavior corresponds to the Bethe regime that we introduced in the pole description given previously. Indeed, we can compare the expression of the elastic cross section obtained in the
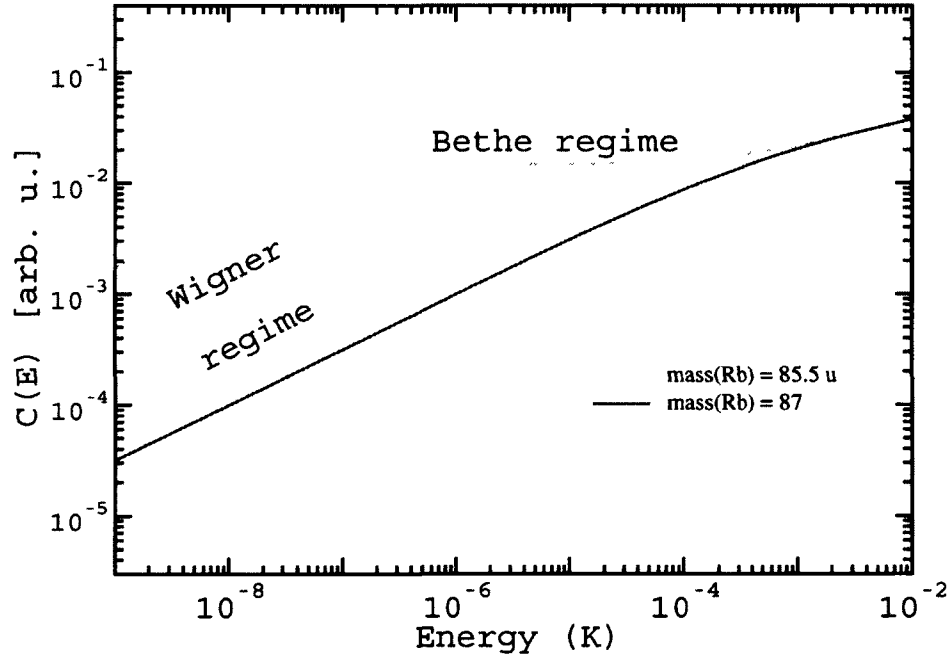

Figure 6.2 — The envelope coefficient $C(E)$, which dictates the strength of the amplitude of the scattering solution $\psi(R)$ at short range.

pole description in Eq. (6.2) to the new expression in terms of A and B, which reads

$$\sigma(k) = \frac{4\pi}{k^2} B^2(k) C^2(k) = 4\pi \frac{B^2(k)}{A^2(k) + k^2 B^2(k)} = \frac{4\pi}{\frac{A^2}{B^2} + k^2} \approx \frac{4\pi}{a^{-2} + k^2}$$

This is the same as Eq. (6.2) in the limit $|a| \to \infty$ (which is equivalent with $p \to 0$).

We emphasize that $C(k)$ dictates the strength of the amplitude of the scattering solution $\psi_k(R)$ at short range; indeed, we recall that ψ_k has its amplitude fixed in the asymptotic region; hence, the envelope $C(k)$ can only affect the wavefunction amplitude at short range. Moreover, the regular solution ϕ_k is very well behaved at low-k, and in the zeroth order it is simply given by the zero-energy solution, $\phi_k(R) \approx \phi_0(R)$. Thus, for low-k, $C(k)$ alone will control the amplitude of $\psi_k(R)$ at short range. This simple result for the single-channel case is very important for the general case of large many channel problems involving inelastic and reactive processes. Indeed, we expect that, for many channel problems which are highly elastic, the following qualitative statement holds for all non-elastic components of the full wavefunction:

$$\psi_n = (\text{Coupling})_{n,e} \times \psi_e \tag{6.5}$$

with ψ_e the entrance channel component, and ψ_n the component of any other (non-elastic) open channel. This rather qualitative expression is especially important in the case of a near threshold resonance. In the next section, our results for $H_2 + Cl$ will demonstrate that the anomalous behavior of ψ_e will be imprinted on all other channels; indeed, we will see that the inelastic and reaction cross section will exhibit striking resonance phenomena at low energy, which can be traced back to the behavior of $C(k)$.

Anticipating the full results for $H_2 + Cl$, we show in Fig. 6.3 the results of a simple exercise in which we varied continuously the mass of the Rb atom. While this type of parametric dependence is well studied for the scattering length, the significance

of a similar study for the C-coefficient, which dictates the short range amplitude of the wavefunction $\psi(R)$ in the ultracold regime, is under-appreciated and mostly overlooked.
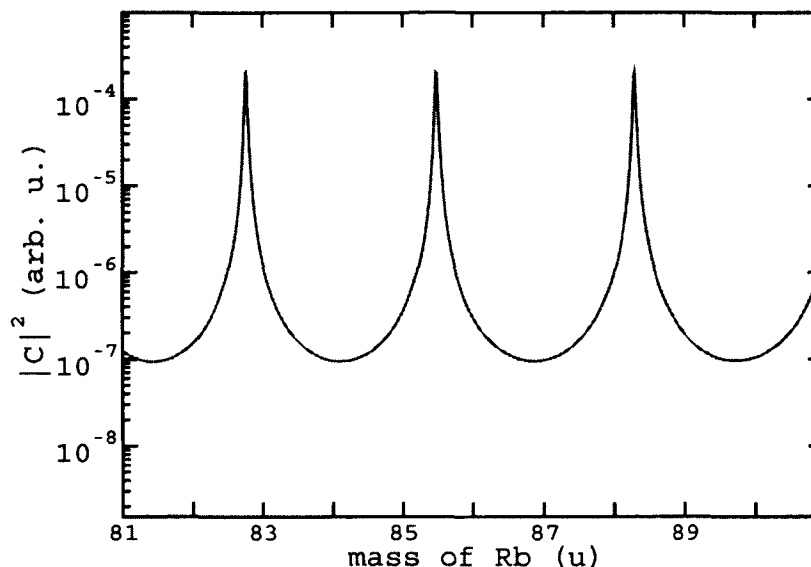
Figure 6.3 — Parametric mass dependence of the short range probability $|\psi_E(R)|^2$ (which is proportional to $|C(E)|^2$). The energy is fixed, $E = 100$ nK. Each resonance corresponds to a new bound state that is gained as the mass increases.

The most convincing argument for the great importance of near threshold resonances in ultracold chemistry is perhaps contained in Fig. 6.4, which shows the R-dependence of the scattering wavefunction at short range, and we see clearly that the amplitude is highly amplified in the resonant case, compared to the "normal" case. For a chemical reaction, this is very significant, as the reaction takes place at short range, and the reaction probability will be proportional with the probability flux in entrance channel at short range. Thus, based on the simple results in Fig. 6.4, we can make the prediction that the reaction rate coefficients in the $T \rightarrow 0$ limit cannot be easily estimated; indeed, their range of values can cover many orders of magnitude.

Figure 6.4 — Amplitude of the wavefunction at short range. Thin black line for the resonant case, and thick gray line for the normal case. The energy is fixed, $E = 1\ \mu$K. We emphasize that both wavefunctions are normalized to unit amplitude for $R \to \infty$.
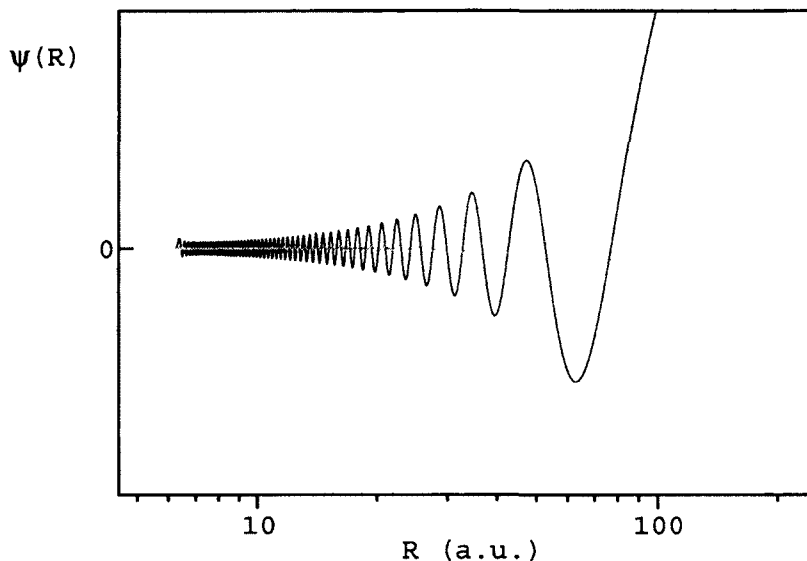
6.2 Near threshold resonances and isotope effects for $H_2 + Cl$

In this section we present the results of a systematic study of the isotope effects that we performed for the $H_2 + Cl$ reaction. We varied continuously the mass of the hydrogen atoms over a wide range, in order to better understand the differences between $H_2 + Cl$ and $D_2 + Cl$. This computationally expensive exercise proved very instructive to us; indeed, sifting through a large quantity of numerical results allowed us to "discover" the unusual behavior caused by near threshold resonances, which we hinted at in the previous section. At the end of our analysis for the simple case of single-channel (purely elastic) scattering, we made a prediction for large scattering problems with many non-elastic open channels (reactive or inelastic); namely, a new type of low energy behavior emerges in the presence of a resonance near the entrance channel threshold. This is expected to hold for all cases in which the elastic component of the full problem is well approximated by the entrance channel alone (taken as a single channel scattering problem). This is usually true for systems with a reaction

87

barrier, when the collision energy is well below the height of the barrier. Thus, ultracold collisions for systems such as $H_2 + Cl$ belong to this category.

Before discussing the results, we first need to clarify that isotope effects for low energy scattering are inevitably linked with the resonance phenomenon caused by poles near the threshold. Indeed, by varying the mass m_H of the hydrogen atoms, the reduced mass in the entrance arrangement ($\frac{1}{\mu_e} = \frac{1}{m_{H_2}} + \frac{1}{m_{Cl}}$) also changes; the latter works effectively as knob for adjusting the strength of the potential. Indeed, the radial equation for the s-wave component of the entrance channel (in the single channel approximation) reads

$$\frac{d^2}{dR^2}\psi_e = 2\mu_e V_{e,e}\psi_e - k_e^2\psi_e$$

with $V_{e,e}(R)$ the diagonal matrix element of the interaction between H_2 and Cl. The factor $2\mu_e$ clearly plays an important role: by increasing (decreasing) it, the strength of the potential is effectively amplified (reduced). Although this affects short range as well as long range, here we focus on the attractive part of $V_{e,e}(R)$ at long range, especially the van der Waals potential well, which can hold quasibound states for the $H_2\cdots Cl$ complex.

In order for a van der Waals complex to have a significant effect on the scattering problem at low energies, its binding energy needs to be within the so called van der Waals energy scale dictated by the asymptotic tail of the potential. For most systems involving H_2, this is roughly the sub-Kelvin regime; a more conservative estimate would be 100 mK. In terms of the pole description given in the preceding section, we have in mind that the pole associated with the van der Waals complex will cause resonance effects, provided it is sufficiently close to the threshold. Thus, the width of the quasibound energy level also needs to be small; this restriction puts limits of the generality of our threshold resonance study. Indeed, for problems which are not

highly elastic, i.e, with strong couplings between the entrance channel and the other open channels, van der Waals complexes are short lived; the energy level of such a complex would be very much broadened due to decay via reactive and inelastic paths. Correspondingly, the large width of the quasibound level would push the pole in the complex plane away from the threshold, and its ability to affect low energy scattering would be diminished.

We begin the discussion of our results with the parametric mass dependence of the reaction cross section shown in Fig. 6.5, which is reminiscent of Fig. 6.3. In fact, the similarity of the resonance structures in the two figures is not accidental; indeed, based on the qualitative statement in Eq. (6.5), we expect that the amplitudes of the outgoing waves in all open channels inherit the resonant behavior of the entrance channel wavefunction ψ_e.

Within the wide range of mass values that we explored, we found three resonances; their approximate positions in atomic mass units (u) are: $m = 0.57$ u, $m = 1.042$ u, and $m = 1.637$ u. Note that the middle one is located rather close to the value of the true mass $m = m_H = 1.008$ u, which proves the usefulness of our exercise (despite the fact that we vary the mass of H artificially). Indeed, as Fig. 6.5 shows, the broad wings of each resonance cover a wide range of mass values; hence, by the accidents of nature, there is a significant likelihood for the real system (e.g., $m = m_H$ or $m = m_D$) to have a near threshold resonance.

Apart from the striking resonances in Fig. 6.5, we also see a general decreasing trend with increasing mass. This background effect is significant (note the log-scale), and it stems from the simple fact that quantum tunneling is more effective for a light atom (H) than for a heavy one (D). The background is clearly marked by the cross section curve for $E = 1$ K, which is a high enough energy for the threshold resonance
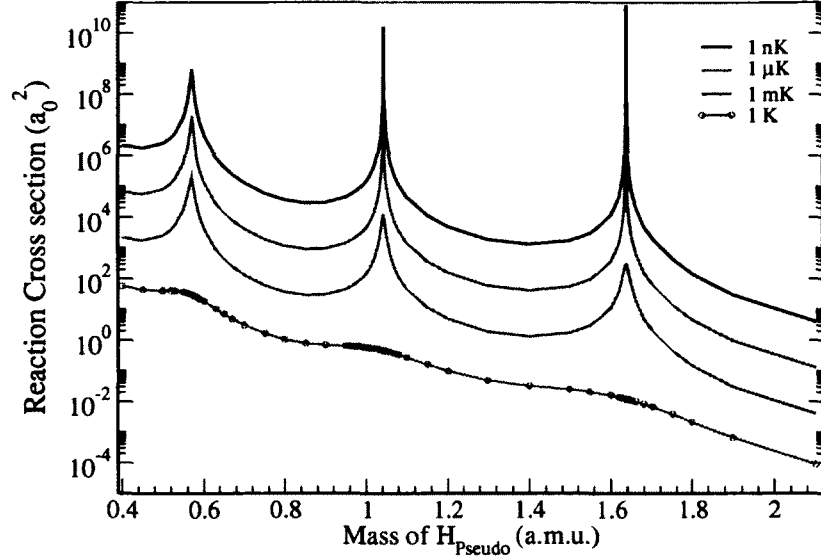
Figure 6.5 — Parametric mass dependence of the reaction cross section for fixed energies.

effects to disappear almost entirely. Note that the vertical shift of the curves with respect to each other is simply due to the $\sigma \sim \frac{1}{k}$ behavior in the Wigner regime.

The parametric mass dependence of the reaction rate coefficient (obtained by thermally averaging the reaction cross section) is shown in Fig. 6.6, which is similar to the previous figure. However, unlike the cross sections, the rate coefficients for different temperatures in the ultracold regime overlap significantly; this stems from the very simple behavior of the rate coefficients for exoergic processes in the Wigner regime, $\mathcal{K}(T) \approx \mathcal{K}(0) = \text{constant}$.

6.2.1 The Bethe regime

After the broad overview of the parametric mass dependence, we will now analyze the anomalous energy dependence of the cross sections for a particular resonant case, i.e., for a fixed mass value. Following the pole description given in Sec. (6.1.1), we factor out the resonant contribution to the diagonal S-matrix element associated with the s-wave component of the entrance channel,
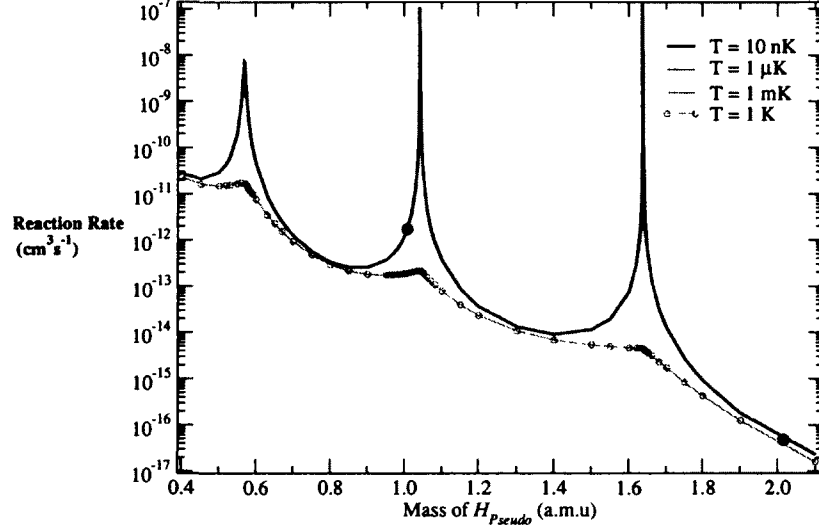
Figure 6.6 — Parametric mass dependence of the reaction rate coefficient for fixed temperatures. The full circles indicate the results for the true H and D.

$$S_{ee}(k) = \frac{p+k}{p-k} \tilde{S}_{ee}(k). \tag{6.6}$$

We will again ignore the background factor $\tilde{S}_{ee}$ in order to emphasize that the pole-zero pair is responsible for the resonance effects. However, unlike the simple case of purely elastic scattering, the pole at $k = p$ is no longer on the imaginary axis, and $|S_{ee}(k)|$ no longer equals unity for real k. In fact, the quantity $1 - |S_{ee}|^2$ represents a measure of all the non-elastic components in the scattering problem under consideration; making use of the unitarity of the S-matrix, we have

$$P_{tot}(k) = \sum_{n \neq e} |S_{n,e}|^2 = 1 - |S_{ee}|^2$$

where P_{tot} is the total probability for non-elastic scattering, which is related to the total non-elastic cross section

$$\sigma^{ne}_{tot}(k) = \frac{\pi}{k^2} P_{tot}(k). \tag{6.7}$$

91

Note that σ_{tot}^{ne} and P_{tot} include all reactive and inelastic contributions, which simplifies our analysis; indeed, in the pole approximation, we obtain

$$P_{tot}(k) \approx 1 - \left| \frac{p+k}{p-k} \right|^2 = -4p' \frac{k}{(k-p')^2 + (p'')^2} \tag{6.8}$$

Apart from the numerator with its simple k-dependence, we again have a Lorentz-type dependence in the denominator, which is now centered at $k = p' < 0$. The quantity P_{tot} is positive, hence $p' < 0$.

Fig. 6.7 shows that $P_{tot}(k)$ has a maximum near the threshold, which is due to a nearby pole at $k = p = p' + ip''$. One can verify easily that $P_{tot}(k)$ attains its maximum for $k = |p|$, which represents the transition between the Wigner regime $(k \ll |p|)$ and the Bethe regime $(k \gg |p|)$. From Eq. (6.8) we find that inside the Wigner regime we have $P_{tot}(k) \approx -4p'|p|^{-2}k$, while in the Bethe regime we have $P_{tot}(k) \approx -4\frac{p'}{k}$. Although the linear graph in Fig. 6.7(a) shows a resonance profile with a pronounced asymmetry, $P_{tot}(k)$ follows a very simple behavior, as given in Eq. (6.8). This simplicity is readily apparent on the log-log plot in Fig. 6.7(b).

In order to demonstrate that the short range envelope coefficient $C(k)$ introduced earlier in our discussion of the single channel case is a useful quantity, and it is relevant for many channel problems, we plot the quantity in $kP_{tot}(k)$ in Fig. 6.8. We emphasize the similarity with Fig. 6.2 for single channel; as suggested in Eq. (6.5), we expected that $S_{n,e}(k) \sim C(k)$. Hence, we have $kP_{tot}(k) \sim |C(k)|^2$.

From Eqs. (6.7) and (6.8) we obtain the total non-elastic cross section in the pole approximation

$$\sigma_{tot}^{ne}(k) \approx -4\pi p' \frac{1}{k\left[(k-p')^2 + (p'')^2\right]} \tag{6.9}$$
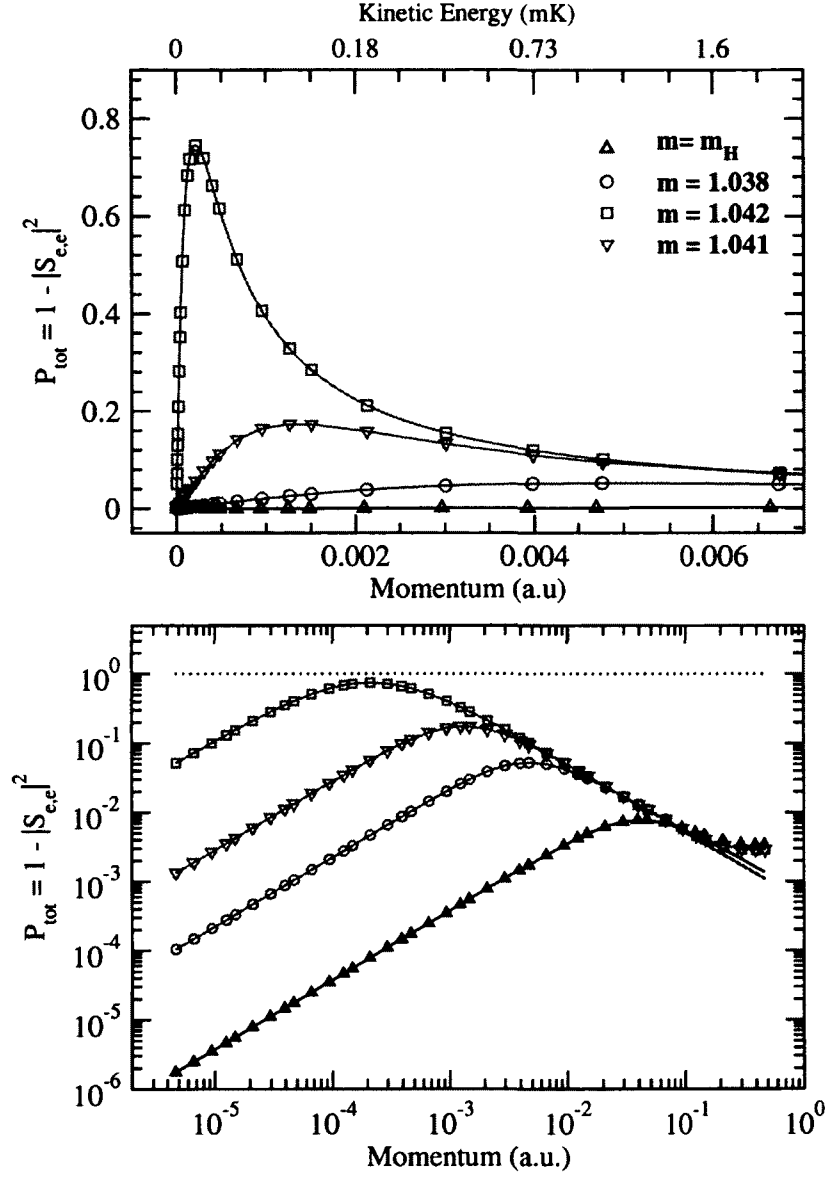
Figure 6.7 — Anomalous behavior of the total non-elastic probability. The same results are shown on a linear scale (upper panel), and on a log-log scale (lower panel). The symbols are for the full computation, and the lines are for the fit based on Eq. (6.8). The dotted line in the lower panel marks the unitarity limit.
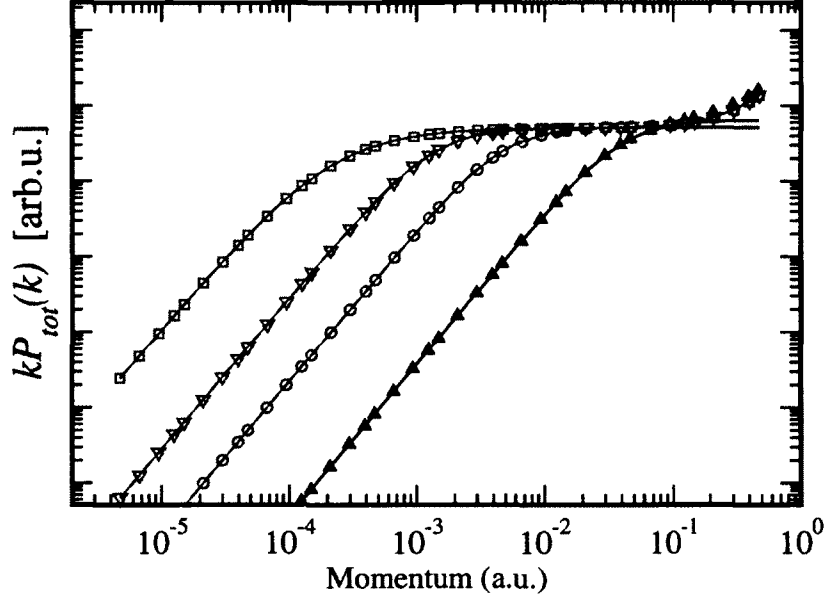
Figure 6.8 — Same as Fig. 6.7 for the quantity $kP_{\text{tot}}(k)$.

This simple expression accounts for the behavior we see in Fig. 6.9, where two separate regimes with different power laws can be identified. The Wigner regime, where $\sigma_{\text{tot}}^{ne}(k) \approx -4\pi p' |p|^{-2} \frac{1}{k}$, is restricted to $k \ll |p|$, as mentioned above. The Bethe regime spans the remainder of the low-k regime, and is characterized by the anomalous behavior $\sigma_{\text{tot}}^{ne}(k) \approx -4\pi \frac{p'}{k^3}$; more specifically, the unusual dependence $\sigma \sim k^{-3}$ holds for $k \gg |p|$.

6.2.2 Extracting the pole from scattering data

One can learn more about near threshold resonances by analyzing the parametric mass dependence of the scattering results. We will see that the mass dependence of the pole itself is remarkably simple, and it is very useful in expressing the mass dependence of the quantities involved in scattering at low energy. The pole can be extracted by using the simple expression in Eq. (6.8) to fit the scattering results obtained from the full computation; the fitting parameters are p' and p''. From a
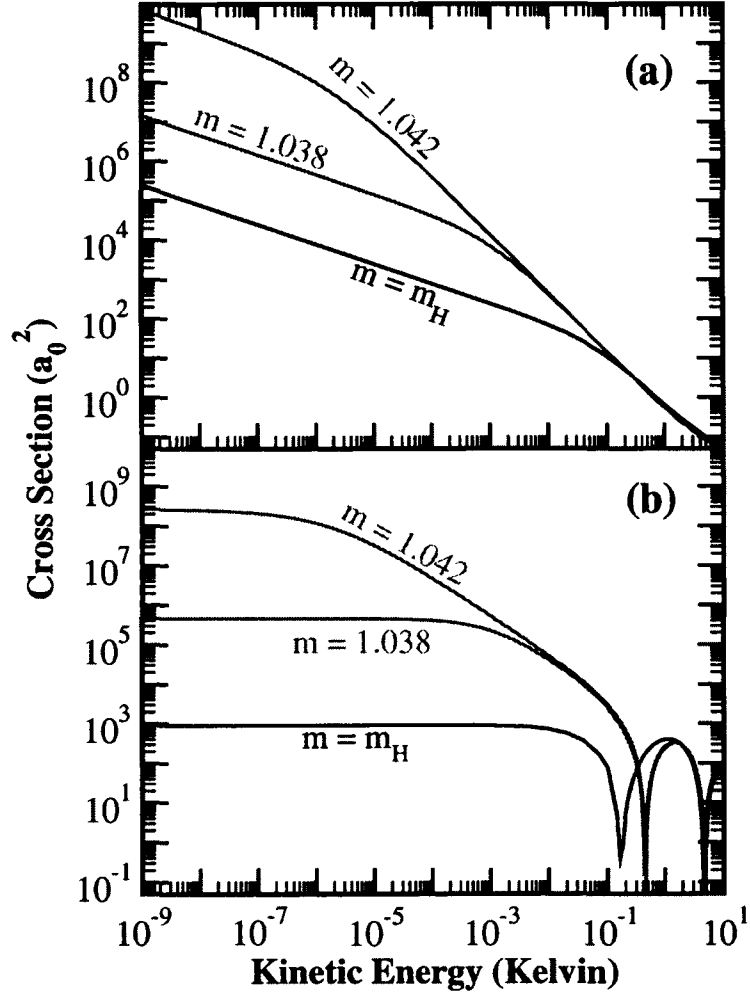
Figure 6.9 — Anomalous behavior of the total non-elastic cross section (a) and elastic (b). The mass value (in a.m.u.) is indicated for each case.
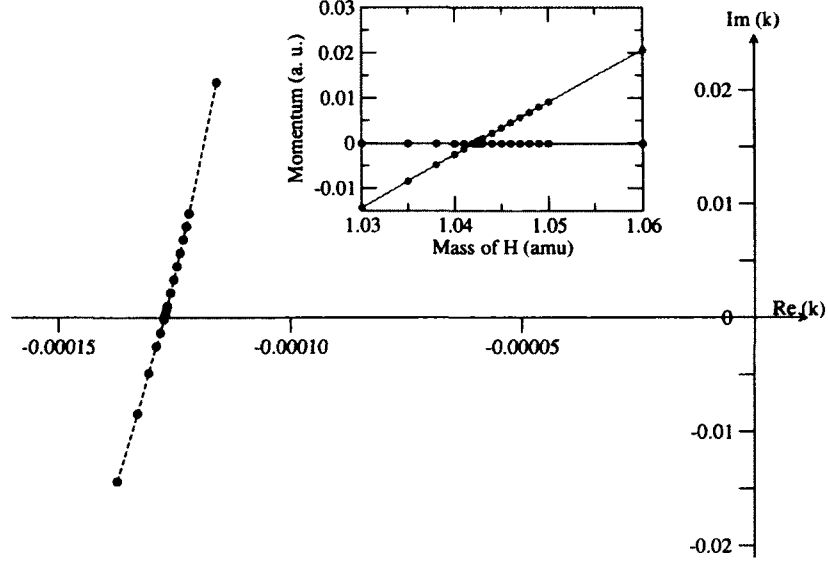
Figure 6.10 — The pole trajectory in the complex momentum plane. The inset shows the the mass dependence of the $p' = \mathrm{Re}(p)$ and $p'' = \mathrm{Im}(p)$.

practical standpoint, it is more convenient to work with Eq. (6.8) for $P_{\mathrm{tot}}(k)$, instead of Eq. (6.9) for the total non-elastic cross section (which diverges when $k \to 0$). We illustrate our fitting procedure in Fig. 6.7, where we see that the pole approximation is very accurate. We extracted the values of $p'(m)$ and $p''(m)$ for different masses m, and we show the results in Fig. 6.10.

As seen in Fig. 6.10, the pole trajectory does cross the real axis; hence, there exists a critical (resonant) value $m = m_0$ for which $p''(m_0) = 0$. For $m = m_0$ both the pole and the zero of $S_{\mathrm{ee}}(k)$ will be located on the real axis, at $k = p'(m_0)$ and $k = -p'(m_0)$ respectively. Thus, at $k_0 \equiv -p'(m_0) > 0$, we have $S_{\mathrm{ee}}(k_0) = 0$, and according to unitarity $P_{\mathrm{tot}}(m_0; k_0) = 1$. We emphasize that $P_{\mathrm{tot}}(k)$ can reach the unitarity limit at low-k only in the special case when $\mathrm{Im}(p) = p'' = 0$. We also note that the widest extent the Bethe regime can have into the ultracold regime is given by $k_0 = |p(m_0)|$; for $m \neq m_0$ the Bethe regime spans a narrower range of energies, as seen in Fig. 6.9, and it eventually disappears when the pole $p(m)$ is no longer in the vicinity of $k = 0$.

96
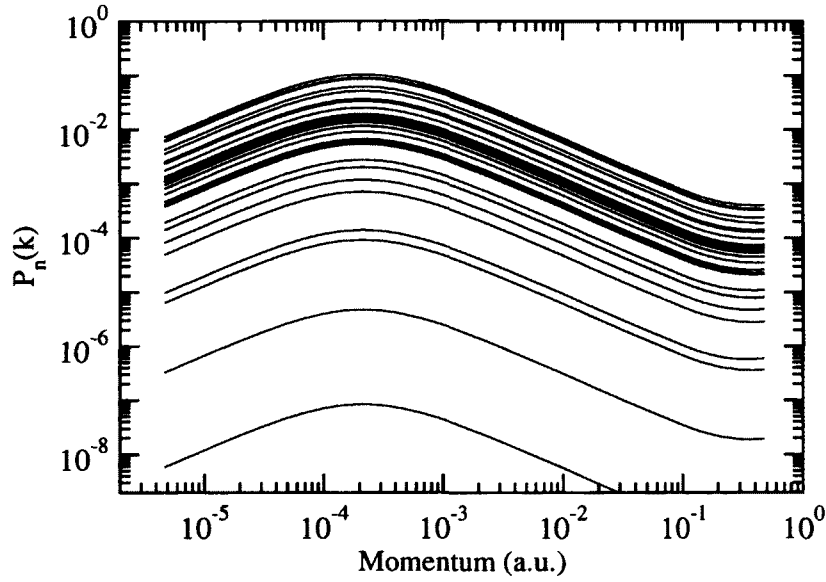
Figure 6.11 — The individual reaction probabilities for each final state of the product. Compare with Fig. 6.7

If the fitting procedure is used for a certain non-elastic component, rather than the total non-elastic probability, one additional fitting parameter should be used as a multiplicative coefficient. As seen in Fig. 6.11, all state-to-state cross sections share the same energy dependence, and they only differ in their branching ratios. In other words, despite the anomalous behavior caused by a threshold resonance, the ratio of any two non-elastic components is constant throughout the entire low energy domain (including both Wigner and Bethe regimes). The elastic cross section also has a simple relationship with the non-elastic ones. Indeed, in the pole approximation, which is very accurate in the extreme case when $p'' \approx 0$, the ratio $Q(m) \equiv \frac{k\sigma_{tot}^{ne}}{\sigma^e} \approx p'$ is independent of energy. Moreover, within a narrow window around $m \approx m_0$, this ratio is also nearly constant as a function of mass; indeed, in the pole approximation we have $Q(m) \approx -p'(m)$, which is approximately constant, as seen in Fig. 6.10. However, when m is swept through a wider range of masses, $p'(m)$ does vary significantly, and the ratio $Q(m)$ does not remain constant.

The fitting procedure can be improved by taking into account the background contribution. For simplicity, we keep our focus on the total elastic and total non-elastic cross sections, both of which can be extracted from $S_{ee}(k)$ in Eq. (6.6). We go beyond the pole approximation by using the familiar low-k expression $\tilde{S}_{ee}(k) \approx e^{-2i\tilde{a}k}$ for the background factor, with $\tilde{a} = \tilde{\alpha} - i\tilde{\beta}$ the background scattering length. From Eq. (6.6) we thus obtain for the full scattering length, $a = \tilde{a} + \frac{i}{p}$, with real and imaginary parts given explicitly as

$$\alpha = \tilde{\alpha} + \frac{p''}{|p|^2}$$

$$\beta = \tilde{\beta} - \frac{p'}{|p|^2}$$

The background value $\tilde{\alpha}$ is typically large, and the resonant term only becomes dominant when the denominator $|p|^2$ approaches is minimal value (near $m \approx m_0$). Thus the background contribution is generally important for the elastic cross section, and $\tilde{\alpha}$ should be used as a fitting parameter. However, P_{tot} does not depend on $\tilde{\alpha}$, as we have $|\tilde{S}_{ee}(k)|^2 = \exp(-4\tilde{\beta}k)$; moreover, for scattering problems that are highly elastic, $\tilde{\beta}$ is very small, and the pole approximation is indeed excellent.

Although the fitting procedure works very well, there is an important caveat regarding the algebraic signs of p'' and $\tilde{\alpha}$. The dominant background contribution to the elastic cross section is given by a cross-term containing the product $(p''\tilde{\alpha})$. Also, the factor $[(k - p')^2 + (p'')^2]^{-2}$ is insensitive to $\text{sgn}(p'')$. Hence, $\text{sgn}(p'')$ and $\text{sgn}(\tilde{\alpha})$ remain undetermined, and unless there is additional information regarding p'' or $\tilde{\alpha}$, the sign ambiguity will persist. In our extensive study for $Cl+H_2$ we have gathered ample information by exploring a wide range of parameter (m) values; thus, by following $p(m)$ and $\tilde{a}(m)$ continuously, we know whether or not $p''(m)$ is positive for any given value of m; we found $\tilde{\alpha}(m) \approx 15.4$ a.u. (nearly constant, and positive). We stress

that, in general, such information may not be available; thus, for an s-wave threshold resonance, scattering alone cannot distinguish between the bound state case ($p'' > 0$) and the anti-bound (or virtual state, $p'' < 0$) case. This is very important, since only when a quasibound state exists can one speak of its binding energy $E_b = (p'^2 - p''^2)/2\mu$ and lifetime $\tau = 1/\Gamma$, with $\Gamma = -2p'p''/\mu > 0$. Note that in the anti-bound case we have $\Gamma < 0$, which is unphysical.

6.2.3 Parametric dependence for the scattering length

The mass dependence of $p'(m)$ and $p''(m)$ in Fig. 6.10 is very simple, and it can be parametrized accordingly:

$$p''(m) \approx \frac{1}{\tilde{\alpha}} \left(\frac{m - m_0}{\Delta m} \right)$$

$$p'(m) \approx -\frac{\epsilon}{\tilde{\alpha}}$$

As a first approximation, we are ignoring any other m-dependence, except for the linear behavior of $p''(m)$. Thus, using the notation $x = \frac{m - m_0}{\Delta m}$, we can write the scattering length in terms of the two parameters $\epsilon = -p'(m_0)\tilde{\alpha}(m_0)$ and Δm,

$$\alpha(x) \approx \tilde{\alpha} \left[1 + \frac{x}{\epsilon^2 + x^2} \right]$$

$$\beta(x) \approx \tilde{\beta}(x) + \tilde{\alpha} \frac{\epsilon}{\epsilon^2 + x^2}$$

Note that in the limit of purely elastic scattering ($\epsilon \to 0$) we obtain the familiar result

$$\alpha(m) \approx \tilde{\alpha} \left(1 + \frac{\Delta m}{m - m_0} \right)$$

which diverges at $m = m_0$. However, when other open (exoergic) channels are coupled with the entrance channel, the divergence is cured; indeed, even the slightest coupling
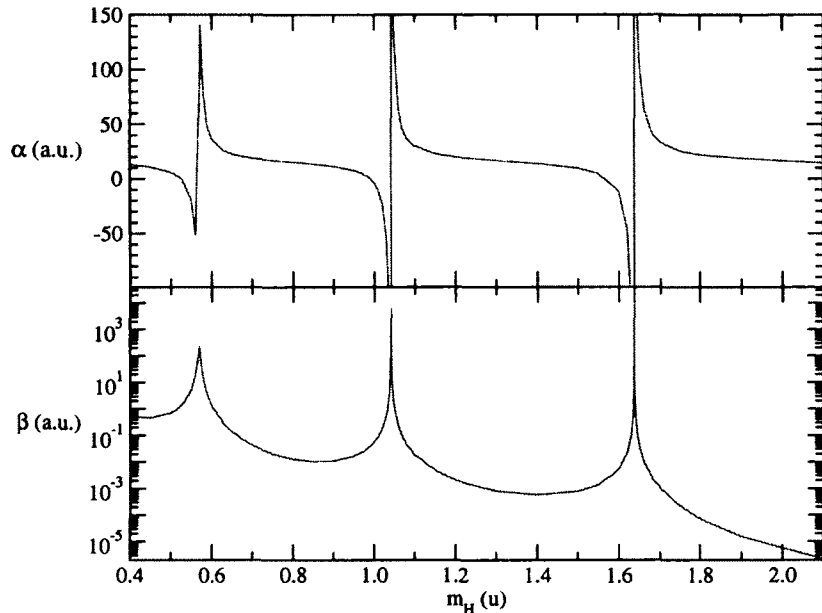
99

Figure 6.12 — Real and imaginary parts of the complex scattering length.

strength (represented by a non-zero value for ϵ) is sufficient to keep α finite (albeit still capable of reaching very large values). Near $x = 0$ ($m = m_0$), within a narrow window of order ϵ, both $\beta(x)$ and $\alpha(x)$ are very sharp. The imaginary part reaches a peak value $\beta_{max} = \beta(m_0) = \frac{\tilde{\alpha}}{\epsilon}$, while $\alpha(x)$ varies abruptly, and its derivative at $x = 0$ is $\frac{d\alpha}{dx}\Big|_{x=0} = \frac{\tilde{\alpha}}{\epsilon^2}$.

Fig. 6.12 shows the mass dependence of the real and imaginary parts of the scattering length $a = \alpha - i\beta$. Note that the imaginary part β includes all non-elastic components (i.e., reactive and inelastic). We emphasize that when a system has a near threshold resonance, all non-elastic components (e.g., any individual state-to-state cross section) will show identical resonance profiles.

6.3 Near threshold resonances in higher partial waves

In order to fully answer the question of threshold behavior in the presence of resonances one has to generalize the description given for $\ell = 0$ to higher partial

waves; indeed, if the S-matrix has a pole near $E = 0$ for $\ell \geq 1$, it is necessary to know what effect it will have on low energy scattering. We will see that, despite the similarities between the s-wave case and the higher partial waves, there are subtle differences that one needs to pay attention to. It turns out that the pole description, which was very convenient for $\ell = 0$, is no longer useful for $\ell \geq 1$. Instead, the more pedestrian description in terms of wavefunction amplitudes is the suitable approach. We start again with the matching conditions

$$
\phi_k(R_*) = \frac{1}{k^{\ell+1}} A(k) \, f_k(R_*) + k^\ell B(k) \, g_k(R_*) \tag{6.10}
$$

$$
\phi_k'(R_*) = \frac{1}{k^{\ell+1}} A(k) \, f_k'(R_*) + k^\ell B(k) \, g_k'(R_*)
$$

which are similar to Eq. (6.3). All three solutions (ϕ, f, g) should carry the subscript ℓ, but we omit it to simplify notations. The two solutions f and g are specified at $R = \infty$, and are chosen such that $f_k(R) \approx j_\ell(kR)$ and $g_k(R) \approx n_\ell(kR)$ when $R \to \infty$ (with j_ℓ and n_ℓ the Riccati–Bessel functions).

For a short range potential, it follows that both $A(k)$ and $B(k)$ are even functions in k, and can be expanded in power series:

$$
A(k) = A_0 + A_1 k^2 + \dots
$$

$$
B(k) = B_0 + B_1 k^2 + \dots.
$$

Note that the case of near threshold resonances corresponds to nearly vanishing values for A_0. Hence the next term in the low-k expansion of $A(k)$ becomes important, while we can still approximate $B(k) \approx B_0$. For the phaseshift we obtain

$$
\tan(\delta_\ell) = \frac{k^\ell B(k)}{\frac{1}{k^{\ell+1}} A(k)} = k^{2\ell+1} \frac{B(k)}{A(k)}
$$

101

and in the limit $k \to 0$ we have

$$\tan(\delta_\ell) \approx \frac{B_0}{A_0} k^{2\ell+1} \qquad \text{(Wigner regime)}$$

When A_0 is very small (i.e., if the potential has a bound state with vanishing binding energy, or it has a shape resonance that is almost bound), the familiar low-k approximation for the phaseshift given above is only valid for a domain restricted to $k \ll \sqrt{|\frac{A_0}{A_1}|}$. This means that the Wigner regime is pushed very close to the threshold. Next, while k is still very low, there will be a transition to a different behavior; namely, for $k \gg \sqrt{|\frac{A_0}{A_1}|}$ we have

$$\tan(\delta_\ell) \approx \frac{B_0}{A_1} k^{2\ell-1} \qquad \text{(Bethe regime)}$$

Note that the change in the power law for the phaseshift will be doubled when the elastic cross section is evaluated. Thus, in the Bethe regime we now have $\sigma_\ell \sim k^{4\ell-4}$, while in the Wigner regime we have the familiar behavior $\sigma_\ell \sim k^{4\ell}$. Recall that in the $\ell = 0$ case the power laws in the two regimes differed by k^2 rather than k^4.

Following the discussion for $\ell = 0$, we now consider the so called envelope coefficient $C(k)$. For $\ell > 0$ we now have

$$C(k) = \frac{k^{\ell+1}}{\sqrt{A^2 + k^{4\ell+2} B^2}}$$

Thus, due to the $k^{4\ell+2}$ factor, the term containing $B(k)$ is almost entirely irrelevant at low-k, except when A(k) vanishes; if $A(k)$ does vanish at $k = k_{\text{res}}$, we have a shape resonance with $C(k)$ having a sharp maximum at $k = k_{\text{res}}$. Within a very narrow window around $k = k_{\text{res}}$, $|C|^2$ follows a Lorentzian profile, which can be written as a

function of energy, and the well known result is obtained for the width of the shape resonance:

$$\Gamma \sim (k_{\text{res}})^{2\ell+1}$$

When k_{res} is extremely small, i.e., when the shape resonance is very near the threshold, the width Γ becomes vanishingly small, and the Lorentz profile becomes almost infinitely sharp. This sharp feature sits atop of a background which has an interesting k-dependence of its own. Indeed, for $k \ll k_{\text{res}}$ we have

$$C(k) \approx \frac{k^{\ell+1}}{|A_0|} \qquad \text{(Wigner regime)}$$

and for $k \gg k_{\text{res}}$ we have

$$C(k) \approx \frac{k^{\ell-1}}{|A_1|} \qquad \text{(Bethe regime)}$$

We point out that immediately after the shape resonance becomes truly bound (just below the threshold), the anomalous behavior with the two different power laws persists, while the sharp feature is absent.

The physical significance of $C(k)$ is very important for the general case of many channel scattering, as discussed in the s-wave case. Specifically, the amplitudes of the outgoing spherical waves in all open channels are proportional to $C(k)$. Hence, the T-matrix elements will inherit its anomalous behavior

$$T_{n,e}(k_e) \sim C(k_e)\sqrt{\frac{k_n}{k_e}}$$

For any state to state cross section we obtain

$$\sigma(n \leftarrow e) = \frac{\pi}{k^2}|Tn, e|^2 \sim \frac{|C(k)|^2}{k^3}$$

with $k = k_e$. Thus, the two regime behavior for the non-elastic cross section reads

$$\sigma_\ell \sim k^{2\ell-1} \qquad \text{(Wigner regime)}$$

$$\sigma_\ell \sim k^{2\ell-5} \qquad \text{(Bethe regime)}$$

For p-wave ($\ell = 1$) this result is quite remarkable, as it yields the same Bethe regime behavior ($\sigma \sim \frac{1}{k^3}$) that we found in the s-wave case. For higher partial waves, the Bethe regime no longer has a significant impact, as the cross section is dominated by s-wave and p-wave near the threshold.

Chapter 7

Conclusion

In this dissertation we have studied two examples of atom–diatom systems with high reaction barriers. We analyzed the role played by the initial vibrational excitation of the diatomic target in the ultracold collision, and by near threshold resonances.

We studied the D + H$_2$(v, $j = 0$) $\rightarrow$ H + DH reaction for a wide range of initial vibrational states $v = 0, 1, 2, 3, 4, \ldots, 8$. For this system, experimental data for the reaction rate coefficient only exist for $T > 167$ K, far above the sub-Kelvin regime; also, accurate theoretical results do not exist for $T \lesssim 100$ K, where the simple Arrhenius behavior will break down. We performed full computations for a very wide range of energies, from $T = 0$ to $T \approx 2000$ K (*i.e.*, up to energies that are comparable to the height of the reaction barrier, which is roughly 5000 K for this system), and found that a deviation from the Arrhenius behavior appears at temperatures very high above the ultracold regime.

We studied another benchmark system in chemistry, namely Cl+H$_2$($v = 1, j = 1$). We used as initial state H$_2$($v = 1, j = 0$), because for the lowest rovibrational state ($v = 0, j = 0$) of H$_2$, the Cl + H$_2$ $\rightarrow$ HCl + H reaction is endoergic. Compared to D–H$_2$, Cl–H$_2$ is a more reactive system, that can support more than one quasibound van der Waals complex, and thus is more likely to exhibit resonance effects in ultracold collisions. We investigated H$_2$ + Cl systematically by "tuning" the binding energy of the least bound van der Waals complex in the entrance channel by varying the mass of H continuously. We explored scattering at ultralow energies, confirming the Wigner

threshold behavior, and we uncovered a new universal regime that we labeled the Bethe regime. It manifests itself when there is a resonance near the threshold of the entrance channel. For s-wave scattering, the behavior of the inelastic and reactive cross sections in the new Bethe regime is $\sigma \sim 1/k^3$, as opposed to the Wigner threshold law, $\sigma \sim 1/k$.

Bibliography

[1] S. L. Mielke, K. A. Peterson, D. W. Schwenke, B. C. Garrett, D. G. Truhlar, J. V. Michael, M.-C. Su, and J. W. Sutherland, $H + H_2$ *Thermal Reaction: A Convergence of Theory and Experiment*, Phys. Rev. Lett. **91**, 063201 (2003).

[2] P. C. Stancil, S. Lepp, and A. Dalgarno, *The Deuterium Chemistry of the Early Universe*, Astrophys. J. **509**, 1 (1998).

[3] J. Z. H. Zhang and W. H. Miller, *Quantum reactive scattering via the S-matrix version of the Kohn variational principle: Differential and integral cross sections for* $D + H_2 \longrightarrow HD + H$, J. Chem. Phys. **91**, 1528 (1989).

[4] B. A. Ridley, W. R. Schulz, and D. J. L. Roy, *Kinetics of the Reaction* $D + H_2 \longrightarrow HD + H$, The Journal of Chemical Physics **44**, 3344 (1966).

[5] D. N. Mitchell and D. J. L. Roy, *Rate constants for the reaction* $D + H_2 \longrightarrow DH + H$ *at low temperatures using ESR detection*, The Journal of Chemical Physics **58**, 3449 (1973).

[6] R. Krems, W. Stwalley, and B. Friedrich, *Cold molecules: theory, experiment, applications*, CRC Press (2009).

[7] O. Dulieu, R. Krems, M. Weidemuller, and S. Willitsch, *Physics and Chemistry of Cold Molecules*, Phys. Chem. Chem. Phys. **13**, 18703 (2011).

[8] P. S. Julienne, T. M. Hanna, and Z. Idziaszek, *Universal ultracold collision rates for polar molecules of two alkali-metal atoms*, Phys. Chem. Chem. Phys. **13**, 19114 (2011).

[9] G. Quéméner and J. L. Bohn, *Strong dependence of ultracold chemical rates on electric dipole moments*, Phys. Rev. A **81**, 022702 (2010).

[10] D. Skouteris, J. Castillo, and D. Manolopoulos, *ABC: a quantum reactive scattering program*, Comp. Phys. Comm. **133**, 128 (2000).

[11] A. Boothroyd, W. Keogh, P. Martin, and M. Peterson, *A refined* H_3 *potential energy surface*, J. Chem. Phys. **104**, 7139 (1996).

[12] C. Seiler, S. D. Hogan, and F. Merkt, *Trapping cold molecular hydrogen*, Phys. Chem. Chem. Phys. **13**, 19000 (2011).

[13] S. C. O. Glover and T. Abel, *Uncertainties in H2 and HD chemistry and cooling and their role in early structure formation*, Monthly Notices of the Royal Astronomical Society **388**, 1627 (2008).

[14] E. P. Wigner, *On the Behavior of Cross Sections Near Thresholds*, Phys. Rev. **73**, 1002 (1948).

[15] R. Newton, *Scattering theory of waves and particles*, Dover books on physics, Dover Publications (2002).

[16] J. Taylor, *Scattering Theory: The Quantum Theory of Nonrelativistic Collisions*, Dover Books on Engineering Series, Dover Publications (2006).

[17] A. Messiah, *Quantum mechanics*, Dover books on physics, Dover Publications (1999).

[18] G. Groenenboom and D. Colbert, *Combining the discrete variable representation with the S-matrix Kohn method for quantum reactive scattering*, J. Chem. Phys. **99**, 9681 (1993).

[19] L. M. Delves, *Tertiary and general-order collisions*, Nuc. Phys. **9**, 391 (1958-1959).

[20] D. E. Manolopoulos, *An improved log derivative method for inelastic scattering*, J. Chem. Phys. **85**, 6425 (1986).

[21] M. P. de Miranda, D. C. Clary, J. F. Castillo, and D. E. Manolopoulos, *Using quantum rotational polarization moments to describe the stereodynamics of the* $H + D_2 \longrightarrow HD + D$ *reaction*, J. Chem. Phys. **108**, 3142 (1998).

[22] J. Aldegunde, P. G. Jambrina, V. Saez-Rabanos, M. P. de Miranda, and F. J. Aoiz, *Quantum mechanical mechanisms of inelastic and reactive* $H+D_2$ *collisions*, Phys. Chem. Chem. Phys. **12**, 13626 (2010).

[23] J. F. Castillo, D. E. Manolopoulos, K. Stark, and H.-J. Werner, *Quantum mechanical angular distributions for the* $F + H_2$ *reaction*, J. Chem. Phys. **104**, 6531 (1996).

[24] J. Castillo and D. Manolopoulos, *Quantum mechanical angular distributions for the F+HD reaction*, Faraday Discuss. Chem. Soc. **110**, 119 (1998).

[25] D. Skouteris, D. Manolopoulos, W. Bian, H. Werner, L. Lai, and K. Liu, *van der Waals interactions in the* $Cl + HD$ *reaction*, Science **286**, 1713 (1999).

[26] N. Balakrishnan and A. Dalgarno, *Chemistry at ultracold temperatures*, Chem. Phys. Lett. **341**, 652 (2001).

[27] N. Balakrishnan, *On the role of van der Waals interaction in chemical reactions at low temperatures*, J. Chem. Phys. **121**, 5563 (2004).

[28] E. Bodo, F. Gianturco, and A. Dalgarno, *The reaction of* $F + D_2$ *at ultra-low temperatures: the effect of rotational excitation*, J. Phys. B - Atom. Mol. Op. Phys. **35**, 2391 (2002).

[29] G. Quéméner and N. Balakrishnan, *Cold and ultracold chemical reactions of F+HCl and F+DCl*, J. Chem. Phys. **128**, 224304 (2008).

[30] J. Aldegunde, J. M. Alvarino, M. P. de Miranda, V. S. Rabanos, and F. J. Aoiz, *Mechanism and control of the* $F + H_2$ *reaction at low and ultralow collision energies*, J. Chem. Phys. **125**, 133104 (2006).

[31] R. T. Pack and G. A. Parker, *Quantum reactive scattering in three dimensions using hyperspherical (APH) coordinates. Theory*, J. Chem. Phys. **87**, 3888 (1987).

[32] M. T. Cvitas, P. Soldan, J. M. Hutson, P. Honvault, and J.-M. Launay, *Interactions and dynamics in* $Li + Li_2$ *ultracold collisions*, J. Chem. Phys. **127**, 074302 (2007).

[33] E. Bodo, F. A. Gianturco, N. Balakrishnan, and A. Dalgarno, *Chemical reactions in the limit of zero kinetic energy: virtual states and Ramsauer minima in* $F + H_2 \rightarrow HF + H$, J. Phys. B **37**, 3641 (2004).

[34] E. Garand, J. Zhou, D. E. Manolopoulos, M. H. Alexander, and D. M. Neumark, *Nonadiabatic Interactions in the* $Cl + H_2$ *Reaction Probed by* ClH_2^- *and* ClD_2^- *Photoelectron Imaging*, Science **319**, 72 (2008).

[35] G. sheng Wu, G. C. Schatz, G. Lendvay, D.-C. Fang, and L. B. Harding, *A new potential surface and quasiclassical trajectory study of* $H + H_2O \longrightarrow OH + H_2$, J. Chem. Phys. **113**, 3150 (2000).

[36] N. Balakrishnan, R. C. Forrey, and A. Dalgarno, *Quenching of H_2 Vibrations in Ultracold ^3He and ^4He Collisions*, Phys. Rev. Lett. **80**, 3224 (1998).

[37] N. Balakrishnan, B. C. Hubartt, L. Ohlinger, and R. C. Forrey, *Noble-gas quenching of rovibrationally excited* H_2, Phys. Rev. A **80**, 012704 (2009).

[38] T. Takayanagi, N. Masaki, K. Nakamura, M. Okamoto, S. Sato, and G. C. Schatz, *The rate constants for the* $H + H_2$ *reaction and its isotopic analogs at low temperatures: Wigner threshold law behavior*, J. Chem. Phys. **86**, 6133 (1987).